

14. Neutrino Masses, Mixing, and Oscillations

Revised October 2021 by M.C. Gonzalez-Garcia (YITP, Stony Brook; ICREA, Barcelona; ICC, U. of Barcelona) and M. Yokoyama (Tokyo U.; Kavli IPMU (WPI), U. Tokyo).

14.1	Neutrinos in the Standard Model: Massless Neutrinos	1
14.2	Extending the Standard Model to Introduce Massive Neutrinos	3
14.2.1	Dirac Neutrinos	4
14.2.2	The See-saw Mechanism	5
14.2.3	Light Sterile Neutrinos	5
14.2.4	Neutrino Masses from Generic New Physics	5
14.3	Lepton Mixing	6
14.4	Mass-Induced Flavour Oscillations in Vacuum	8
14.5	Propagation of Massive Neutrinos in Matter	10
14.5.1	The Mikheyev-Smirnov-Wolfenstein Effect for Solar Neutrinos	13
14.6	Experimental Study of Neutrino Oscillations	15
14.6.1	Solar Neutrinos	15
14.6.2	Atmospheric Neutrinos	19
14.6.3	Accelerator Neutrinos	22
14.6.4	Reactor Antineutrinos	27
14.7	Combined Analysis of Experimental Results: The 3ν Paradigm	32
14.7.1	3ν Oscillation Probabilities	33
14.7.2	3ν Oscillation Analysis	36
14.7.3	Convention-independent Measures of Leptonic CP Violation in 3ν Mixing	37
14.8	Beyond 3ν : Additional Neutrinos at the eV Scale	38
14.9	Laboratory Probes of ν Mass Scale and its Nature	41
14.9.1	Constraints from Kinematics of Weak Decays	41
14.9.2	Dirac vs. Majorana: Neutrinoless Double-beta Decay	43
14.9.3	Experimental Search for Neutrinoless Double-beta Decay	44

14.1 Neutrinos in the Standard Model: Massless Neutrinos

The gauge symmetry principle is one of the pillars of the great success of modern particle physics as it establishes an unambiguous connection between local (gauge) symmetries and forces mediated by spin-1 particles. In the Standard Model (SM) of particle physics the strong, weak, and electromagnetic interactions are connected to gauge symmetry under $SU(3)_C \times SU(2)_L \times U(1)_Y$ where C stands for colour, L for left-handedness, and Y for hypercharge. The SM gauge symmetry is spontaneously broken to $SU(3)_C \times U(1)_{EM}$ where $U(1)_{EM}$ couples to the electromagnetic charge $Q_{EM} = T_{L3} + Y$ (T_{L3} is the weak isospin which is the third generator of $SU(2)_L$). The model explains all the interactions of the known fermions once they are assigned to a well defined representation of the gauge group. The construction and tests of the Standard Model as a gauge theory are covered in Chapter 9 “Quantum chromodynamics” and Chapter 10 “Electroweak model and constraints on new physics” of this *Review*. Here we emphasize that the gauge invariance principle requires that all terms in the Lagrangian, including the mass terms, respect the local symmetry. This has important implications for the neutrino and in particular for the question of the neutrino mass ¹.

¹The physics of massive neutrinos has been the subject of excellent books such as [1–5] and multiple review articles. The contents of the present review is built upon the structure and the contents of the review articles [6, 7].

In the SM, neutrinos are fermions that do not have strong nor electromagnetic interactions. Consequently, they are singlets of the subgroup $SU(3)_C \times U(1)_{\text{EM}}$. They are part of the lepton doublets $L_{L\ell} = \begin{pmatrix} \nu_\ell \\ \ell \end{pmatrix}_L$ where f_L is the left-handed component of the fermion f , $f_L = P_L f \equiv \frac{1-\gamma_5}{2} f$. In what follows we will refer as *active* neutrinos to neutrinos that are part of these lepton doublets. In the SM there is one active neutrino for each charged leptons, $\ell = e, \mu, \tau$. $SU(2)_L$ gauge invariance dictates the form of weak charged current (CC) interactions between the neutrinos and their corresponding charged leptons and neutral current (NC) among themselves to be:

$$-\mathcal{L}_{\text{CC}} = \frac{g}{\sqrt{2}} \sum_{\ell} \bar{\nu}_{L\ell} \gamma^\mu \ell_L^- W_\mu^+ + \text{h.c.}, \quad (14.1)$$

$$-\mathcal{L}_{\text{NC}} = \frac{g}{2 \cos \theta_W} \sum_{\ell} \bar{\nu}_{L\ell} \gamma^\mu \nu_{L\ell} Z_\mu^0. \quad (14.2)$$

In the above equations, g is the coupling constant associated with $SU(2)$ and θ_W is the Weinberg angle. Equations(14.1) and (14.2) describe all the neutrino interactions in the SM. In particular, Eq.(14.2) determines the decay width of the Z boson into light ($m_\nu \leq m_Z/2$) left-handed neutrinos states. Thus from the measurement of the total decay width of the Z one can infer the number of such states. At present the measurement implies $N_\nu = 2.984 \pm 0.008$ (see Particle Listing). As a result any extension of the SM should contain three, and only three, light active neutrinos.

Sterile neutrinos are defined as having no SM gauge interactions, that is, they are singlets of the complete SM gauge group. Thus the SM, as the gauge theory able to describe all known particle interactions, contains no sterile neutrinos.

The SM with its gauge symmetry and the particle content required for the gauge interactions, that is, in the absence of SM singlets, respects an accidental global symmetry that is not imposed but appears as a consequence of the gauge symmetry and the representation of the matter fields:

$$G_{\text{SM}}^{\text{global}} = U(1)_B \times U(1)_{L_e} \times U(1)_{L_\mu} \times U(1)_{L_\tau}, \quad (14.3)$$

where $U(1)_B$ is the baryon number symmetry, and $U(1)_{L_e, L_\mu, L_\tau}$ are the three lepton flavour symmetries. The total lepton number, $L_e + L_\mu + L_\tau$, is then also an accidental symmetry since it is a subgroup of $G_{\text{SM}}^{\text{global}}$. This fact has consequences that are relevant to the question of the neutrino mass as we argue next.

In the SM, the masses of the fermions are generated via a Yukawa coupling of the scalar Higgs doublet ϕ with a fermion right-handed and left-handed component. The former is an $SU(2)_L$ singlet, the latter is part of a doublet. For leptons, we can build such a term coupling the left-handed lepton doublets L_L with the right-handed charged lepton fields E_R :

$$-\mathcal{L}_{\text{Yukawa,lep}} = Y_{ij}^\ell \bar{L}_{Li} \phi E_{Rj} + \text{h.c.} \quad (14.4)$$

After spontaneous symmetry breaking these terms lead to charged lepton masses

$$m_{ij}^\ell = Y_{ij}^\ell \frac{v}{\sqrt{2}}, \quad (14.5)$$

where v is the vacuum expectation value of the Higgs field. However, since the model does not contain right-handed neutrinos, no such Yukawa interaction can be built for the neutrinos, which are consequently massless at the Lagrangian level.

In principle, a neutrino mass term could be generated at loop level. With the particle content of the SM the only possible neutrino mass term that could be constructed is the bilinear $\bar{L}_L L_L^c$, where

L_L^c is the charge conjugated field, $L_L^c = C\bar{L}_L^T$ and C is the charge conjugation matrix. However this term is forbidden in the SM because it violates the total lepton symmetry by two units and therefore it cannot be induced by loop corrections because it breaks the accidental symmetry of the model. Also, because $U(1)_{B-L}$ is a non-anomalous subgroup of $G_{\text{SM}}^{\text{global}}$, the bilinear $\bar{L}_L L_L^c$, cannot be induced by nonperturbative corrections either since it breaks $B-L$.

We conclude that within the SM neutrinos are precisely massless. Consequently one must go beyond the SM in order to add a mass to the neutrino.

14.2 Extending the Standard Model to Introduce Massive Neutrinos

From the above discussion, we conclude that it is not possible to construct a renormalizable mass term for the neutrinos with the fermionic content and gauge symmetry of the SM. The obvious consequence is that in order to introduce a neutrino mass in the theory one must extend the particle content of the model, depart from gauge invariance and/or renormalizability, or do both.

As a matter of fact, neutrino mass terms can be constructed in different ways. In the following we shall assume to maintain the gauge symmetry and explore the different possibilities to introduce a neutrino mass term adding to the SM an arbitrary number of sterile neutrinos ν_{si} ($i = 1, \dots, m$).

In the SM extended with the addition of m number of sterile neutrinos one can construct two gauge invariant renormalizable operators leading to two types of mass terms

$$-\mathcal{L}_{M_\nu} = M_{Dij}\bar{\nu}_{si}\nu_{Lj} + \frac{1}{2}M_{Nij}\bar{\nu}_{si}\nu_{sj}^c + \text{h.c.}, \quad (14.6)$$

where ν^c is the neutrino charge conjugated field (defined in section 14.1). M_D is a complex matrix of dimension $m \times 3$ and M_N is a symmetric $m \times m$ matrix.

The first term is generated after spontaneous electroweak symmetry breaking from Yukawa interactions,

$$Y_{ij}^\nu\bar{\nu}_{si}\tilde{\phi}^\dagger L_{Lj} \Rightarrow M_{Dij} = Y_{ij}^\nu \frac{v}{\sqrt{2}}, \quad (14.7)$$

in similarity to Eqs.(14.4) and (14.5) for the charged fermion masses. It is correspondingly called a Dirac mass term. It conserves total lepton number but it can break the lepton flavour number symmetries.

The second term in Eq.(14.6) is a Majorana mass term and it differs from the Dirac mass terms in several relevant aspects. First, it is a singlet of the SM gauge group and, as such, it can appear as a bare mass term in the Lagrangian. Second, since it involves two neutrino fields (right-handed in this case), it breaks lepton number by two units. In general, such a term is not allowed if the neutrinos carry any additive conserved charge.

It is possible to rewrite Eq.(14.6) as:

$$-\mathcal{L}_{M_\nu} = \frac{1}{2}(\bar{\nu}_L^c, \bar{\nu}_s) \begin{pmatrix} 0 & M_D^T \\ M_D & M_N \end{pmatrix} \begin{pmatrix} \bar{\nu}_L \\ \bar{\nu}_s^c \end{pmatrix} + \text{h.c.} \equiv \bar{\nu}^c M_\nu \bar{\nu} + \text{h.c.}, \quad (14.8)$$

where $\bar{\nu} = (\bar{\nu}_L, \bar{\nu}_s^c)^T$ is a $(3+m)$ -dimensional vector. The matrix M_ν is complex and symmetric². Thus it can be diagonalized by a unitary matrix V^ν of dimension $(3+m)$, so

$$(V^\nu)^T M_\nu V^\nu = \text{diag}(m_1, m_2, \dots, m_{3+m}). \quad (14.9)$$

One can express the original weak eigenstates in terms of the resulting $3+m$ mass eigenstates

$$\bar{\nu}_{\text{mass}} = (V^\nu)^\dagger \bar{\nu}, \quad (14.10)$$

²Notice that Eq.(14.8) corresponds to the tree-level neutrino mass matrix. Corrections are induced at the loop level, which in particular lead to non-vanishing $\bar{\nu}_L^c \nu_L$ entry [8].

and in terms of the mass eigenstates, Eq.(14.8) takes the form:

$$\begin{aligned} -\mathcal{L}_{M\nu} &= \frac{1}{2} \sum_{k=1}^{3+m} m_k \left(\bar{\nu}_{\text{mass},k}^c \nu_{\text{mass},k} + \bar{\nu}_{\text{mass},k} \nu_{\text{mass},k}^c \right) \\ &= \frac{1}{2} \sum_{k=1}^{3+m} m_k \bar{\nu}_{Mk} \nu_{Mk}, \end{aligned} \quad (14.11)$$

where

$$\nu_{Mk} = \nu_{\text{mass},k} + \nu_{\text{mass},k}^c = (V^{\nu\dagger} \vec{\nu})_k + (V^{\nu\dagger} \vec{\nu})_k^c. \quad (14.12)$$

So these states obey the Majorana condition

$$\nu_M = \nu_M^c, \quad (14.13)$$

and are referred to as Majorana neutrinos. The Majorana condition implies that only one field describes both neutrino and antineutrino states, unlike the case of a charge of which particles and antiparticles are described by two different fields. So a Majorana neutrino can be described by a two-component spinor unlike the charged fermions, which are Dirac particles, and are represented by four-component spinors.

Inverting Eq.(14.12) we can write the weak-doublet components of the neutrino fields as:

$$\nu_{Li} = P_L \sum_{j=1}^{3+m} V_{ij}^{\nu} \nu_{Mj} \quad i = 1, 2, 3, \quad (14.14)$$

where P_L is the left projector.

In the following, we will discuss some interesting particular cases of this general framework: light Dirac neutrinos in Sec.14.2.1, and light Majorana neutrinos and the see-saw mechanism in Sec.14.2.2. A special case of the second example is the possibility of light-sterile neutrinos discussed in Sec.14.2.3. In Sec.14.2.4 we shall discuss the effective generation of neutrino masses from non-renormalizable operators (of which the see-saw mechanism is a particular realization).

14.2.1 Dirac Neutrinos

Imposing $M_N = 0$ is equivalent to imposing lepton number symmetry on the model. In doing this only the first term in Eq.(14.6), the Dirac mass term, is allowed. If sterile neutrinos are three ($m = 3$), we can identify them with the right-handed component of a four-spinor neutrino field. In this case the Dirac mass term can be diagonalized with two 3×3 unitary matrices, V^{ν} and V_R^{ν} as:

$$V_R^{\nu\dagger} M_D V^{\nu} = \text{diag}(m_1, m_2, m_3). \quad (14.15)$$

The neutrino mass term can be written as:

$$-\mathcal{L}_{M\nu} = \sum_{k=1}^3 m_k \bar{\nu}_{Dk} \nu_{Dk}, \quad (14.16)$$

where

$$\nu_{Dk} = (V^{\nu\dagger} \vec{\nu}_L)_k + (V_R^{\nu\dagger} \vec{\nu}_s)_k, \quad (14.17)$$

so the weak-doublet components of the neutrino fields are

$$\nu_{Li} = P_L \sum_{j=1}^3 V_{ij}^{\nu} \nu_{Dj}. \quad i = 1, 2, 3. \quad (14.18)$$

Let us stress that in this case both the low-energy matter content and the assumed symmetries are different from those of the SM. Consequently, the SM is not even a good low-energy effective theory. Furthermore, this scenario does not explain the fact that neutrinos are much lighter than the corresponding charged fermions, because all acquire their mass via the same mechanism.

14.2.2 The See-saw Mechanism

If the mass eigenvalues of M_N are much higher than the scale of electroweak symmetry breaking v , the diagonalization of M_ν leads to three light neutrinos, ν_l , and m heavy neutrinos, N :

$$-\mathcal{L}_{M_\nu} = \frac{1}{2}\bar{\nu}_l M^l \nu_l + \frac{1}{2}\bar{N} M^h N, \quad (14.19)$$

with

$$M^l \simeq -V_l^T M_D^T M_N^{-1} M_D V_l, \quad M^h \simeq V_h^T M_N V_h, \quad (14.20)$$

and

$$V^\nu \simeq \left[\begin{array}{cc} \left(1 - \frac{1}{2}M_D^\dagger M_N^{*-1} M_N^{-1} M_D\right) V_l & M_D^\dagger M_N^{*-1} V_h \\ -M_N^{-1} M_D V_l & \left(1 - \frac{1}{2}M_N^{-1} M_D M_D^\dagger M_N^{*-1}\right) V_h \end{array} \right], \quad (14.21)$$

where V_l and V_h are 3×3 and $m \times m$ unitary matrices respectively. From Eq.(14.20) we see that the masses of the heavier states are proportional to M_N while those of the lighter ones to M_N^{-1} , hence the name *see-saw mechanism* [9–13]. Also, as seen from Eq.(14.21), the heavy states are mostly right-handed while the light ones are mostly left-handed. Both the light and the heavy neutrinos are Majorana particles. Two well-known examples of extensions of the SM leading to a see-saw mechanism for neutrino masses are SO(10) Grand Unified Theories [10, 11] and left-right symmetry [13].

In this case, the SM is a good effective low energy theory. Indeed the see-saw mechanism is a particular example of a full theory whose low energy effective realization is the SM with three light Majorana neutrinos which we describe in Sec.14.2.4.

14.2.3 Light Sterile Neutrinos

If the scale of some $n_s \leq m$ eigenvalues of M_N are not higher than the electroweak scale, the low energy spectrum contains n_s additional light states with a large admixture of sterile component. As in the case with Dirac Neutrinos, the SM is not a good low energy effective theory: there are more than three ($3+n_s$) light neutrinos, and they are admixtures of doublet and singlet fields. As in the general case, both light and heavy neutrinos are Majorana particles.

14.2.4 Neutrino Masses from Generic New Physics

Under the generic hypothesis that new physics (NP) beyond the SM only manifests itself directly above some scale Λ_{NP} , we can consider that the SM is an effective low energy theory which is valid to describe the physical world at energies well below Λ_{NP} with the same gauge group, fermionic spectrum, and the pattern of spontaneous symmetry breaking of the SM. However, this is an effective theory, holding only till energy below Λ_{NP} , and consequently does not need to be renormalizable. In this case, the low energy Lagrangian can contain non-renormalizable higher dimensional terms whose effect will be suppressed by powers $1/\Lambda_{\text{NP}}^{\text{dim}-4}$.

In this approach, the least suppressed NP effects at low energy are expected to come from $\text{dim}=5$ operators. With the SM fields and gauge symmetry one can only construct the following set of dimension-five terms

$$\mathcal{O}_5 = \frac{Z_{ij}^\nu}{\Lambda_{\text{NP}}} \left(\bar{L}_{Li} \tilde{\phi} \right) \left(\tilde{\phi}^T L_{Lj}^C \right) + \text{h.c.} \quad (14.22)$$

This set violates (14.3), which poses no problem since, in general, there is no reason for the NP to respect the accidental symmetries of the SM. In particular, it violates the total lepton number by

two units, and after spontaneous symmetry breaking it generates a bilinear neutrino field term:

$$-\mathcal{L}_{M_\nu} = \frac{Z_{ij}^\nu}{2} \frac{v^2}{\Lambda_{\text{NP}}} \bar{\nu}_{Li} \nu_{Lj}^c + \text{h.c.} . \quad (14.23)$$

This is a Majorana mass term (see Eq.(14.8)). It is built with the left-handed neutrino fields and with mass matrix:

$$(M_\nu)_{ij} = Z_{ij}^\nu \frac{v^2}{\Lambda_{\text{NP}}} . \quad (14.24)$$

We conclude that Eq.(14.24) would arise in a generic extension of the SM and that neutrino masses are very likely to appear if there is NP. Comparing Eq.(14.24) and Eq.(14.5), we also find that the scale of neutrino masses is suppressed by v/Λ_{NP} when compared to the scale of charged fermion masses, which provides an explanation for their smallness. Furthermore, both total lepton number and the lepton flavour symmetry $U(1)_e \times U(1)_\mu \times U(1)_\tau$ are broken by Eq.(14.24), which means that, generically, in the absence of additional symmetries on the coefficients Z_{ij} , we can expect lepton flavour mixing and CP violation as we discuss in the next section.

Finally, we notice that, as mentioned in Sec.14.2.2, a theory where the NP is composed of m heavy sterile neutrinos, provides an specific example of a theory which at low energy theory contains three light mass eigenstates with an effective dim-5 interaction of the form (14.22) with $\Lambda_{\text{NP}} = M_N$. In this case, the NP scale is the characteristic mass scale of the heavy sterile neutrinos.

14.3 Lepton Mixing

Let us start by considering $n = 3 + m$ massive neutrino states and denote the neutrino mass eigenstates by $(\nu_1, \nu_2, \nu_3, \dots, \nu_n)$. The neutrino interaction eigenstates are denoted by $\vec{\nu} = (\nu_{Le}, \nu_{L\mu}, \nu_{L\tau}, \nu_{s1}, \dots, \nu_{sm})$. We label the corresponding mass and interaction eigenstates for the charged leptons as (e, μ, τ) and (e^I, μ^I, τ^I) , respectively. The Lagrangian for the leptonic charged current interactions in the mass basis takes the form:

$$-\mathcal{L}_{\text{CC}} = \frac{g}{\sqrt{2}} (\bar{e}_L, \bar{\mu}_L, \bar{\tau}_L) \gamma^\mu U \begin{pmatrix} \nu_1 \\ \nu_2 \\ \nu_3 \\ \vdots \\ \nu_n \end{pmatrix} W_\mu^+ + \text{h.c.} , \quad (14.25)$$

where U is a $3 \times n$ matrix [14–16]. It satisfies the unitary condition

$$UU^\dagger = I_{3 \times 3} . \quad (14.26)$$

However, in general $U^\dagger U \neq I_{n \times n}$.

In the interaction basis, the mass terms for the leptons are:

$$-\mathcal{L}_M = [(\bar{e}_L^I, \bar{\mu}_L^I, \bar{\tau}_L^I) M_\ell \begin{pmatrix} e_R^I \\ \mu_R^I \\ \tau_R^I \end{pmatrix} + \text{h.c.}] - \mathcal{L}_{M_\nu} , \quad (14.27)$$

with \mathcal{L}_{M_ν} given in Eq.(14.8). M_ℓ can be diagonalized with two 3×3 unitary matrices V^ℓ and V_R^ℓ which satisfy

$$V^{\ell\dagger} M_\ell V_R^\ell = \text{diag}(m_e, m_\mu, m_\tau) . \quad (14.28)$$

Then for the charged leptons we have

$$-\mathcal{L}_{M_\ell} = \sum_{k=1}^3 m_{\ell_k} \bar{\ell}_k \ell_k , \quad (14.29)$$

with

$$\ell_k = (V^{\ell\dagger} \ell_L^I)_k + (V_R^{\ell\dagger} \ell_R^I)_k. \quad (14.30)$$

Inverting the equation above we find that the weak-doublet components of the charged lepton fields are

$$\ell_{Li}^I = P_L \sum_{j=1}^3 V_{ij}^{\ell} \ell_j. \quad i = 1, 2, 3 \quad (14.31)$$

From Eqs.(14.14), (14.18) and (14.31) we find that the mixing matrix U can be expressed as:

$$U_{ij} = \mathcal{P}_{\ell,ii} V_{ik}^{\ell\dagger} V_{kj}^{\nu} (\mathcal{P}_{\nu,jj}). \quad (14.32)$$

The matrix $V^{\ell\dagger} V^{\nu}$ contains a number of phases that are not physical. Three of them are eliminated by the diagonal 3×3 phase matrix \mathcal{P}_{ℓ} that absorbs them in the charged lepton mass eigenstates. If neutrinos are Dirac states, further $n - 1$ are similarly eliminated by absorbing them in the neutrino mass eigenstates with the diagonal $n \times n$ phase matrix \mathcal{P}_{ν} . For Majorana neutrinos, $\mathcal{P}_{\nu} = I_{n \times n}$ because one cannot rotate by an arbitrary phase a Majorana field without physical effects. If one rotates a Majorana neutrino by a phase, this phase will appear in its mass term, which will no longer be real. Consequently, the number of phases that can be absorbed by redefining the mass eigenstates depends on whether the neutrinos are Dirac or Majorana particles. Altogether for $n \geq 3$ Majorana [Dirac] neutrinos, the U matrix contains a total of $6(n - 2)$ [$5n - 11$] real parameters, of which $3(n - 2)$ are angles, and $3(n - 2)$ [$2n - 5$] can be interpreted as physical phases.

The possibility of arbitrary mixing between massive neutrino states was first discussed in the context of two neutrinos introduced in Ref. [17] (the possibility of two mixed massless flavour neutrino states had been previously considered in the literature [18], and the possibility of mixing between neutrino and antineutrino states even earlier, in the seminal paper of Pontecorvo [19]). For that case, in which only mixing between two generations is considered with $n = 2$ distinct neutrino masses, the U matrix is 2×2 and contains one mixing angle if the neutrinos are Dirac and an additional physical phase if they are Majorana.

If there are only $n = 3$ Majorana neutrinos, U is a 3×3 matrix analogous to the CKM matrix for the quarks [20, 21], but due to the Majorana nature of the neutrinos it depends on six independent parameters: three mixing angles and three phases. In this case the mixing matrix can be conveniently parameterized as:

$$U = \begin{pmatrix} 1 & 0 & 0 \\ 0 & c_{23} & s_{23} \\ 0 & -s_{23} & c_{23} \end{pmatrix} \cdot \begin{pmatrix} c_{13} & 0 & s_{13} e^{-i\delta_{\text{CP}}} \\ 0 & 1 & 0 \\ -s_{13} e^{i\delta_{\text{CP}}} & 0 & c_{13} \end{pmatrix} \cdot \begin{pmatrix} c_{12} & s_{12} & 0 \\ -s_{12} & c_{12} & 0 \\ 0 & 0 & 1 \end{pmatrix} \cdot \begin{pmatrix} e^{i\eta_1} & 0 & 0 \\ 0 & e^{i\eta_2} & 0 \\ 0 & 0 & 1 \end{pmatrix}, \quad (14.33)$$

where $c_{ij} \equiv \cos \theta_{ij}$ and $s_{ij} \equiv \sin \theta_{ij}$. The angles θ_{ij} can be taken without loss of generality to lie in the first quadrant, $\theta_{ij} \in [0, \pi/2]$ and the phases $\delta_{\text{CP}}, \eta_i \in [0, 2\pi]$. This is to be compared to the case of three Dirac neutrinos. In this case, the Majorana phases, η_1 and η_2 , can be absorbed in the neutrino states so the number of physical phases is one (similar to the CKM matrix). Thus we can write U as:

$$U = \begin{pmatrix} c_{12} c_{13} & s_{12} c_{13} & s_{13} e^{-i\delta_{\text{CP}}} \\ -s_{12} c_{23} - c_{12} s_{13} s_{23} e^{i\delta_{\text{CP}}} & c_{12} c_{23} - s_{12} s_{13} s_{23} e^{i\delta_{\text{CP}}} & c_{13} s_{23} \\ s_{12} s_{23} - c_{12} s_{13} c_{23} e^{i\delta_{\text{CP}}} & -c_{12} s_{23} - s_{12} s_{13} c_{23} e^{i\delta_{\text{CP}}} & c_{13} c_{23} \end{pmatrix}. \quad (14.34)$$

This matrix is often called the Pontecorvo-Maki-Nakagawa-Sakata (PMNS) mixing matrix.

Notice that when the charged leptons have no other interactions than the SM ones, one can identify their interaction eigenstates with the corresponding mass eigenstates up to phase redefinition. This implies that, in this case, U is just a $3 \times n$ sub-matrix of the unitary neutrino mass diagonalizing matrix V^ν .

Finally, let us point out that for the case of 3 light Dirac neutrinos, the procedure above leads to a unitary U matrix for the light states. But for three light Majorana neutrinos, this is not the case when the full spectrum contains states which are heavy and are not in the low energy spectrum as seen, for example, in Eq.(14.21). This implies that, strictly speaking, the parametrization in Eq.(14.33) is not valid to describe the flavour mixing of the three light Majorana neutrinos in the see-saw mechanism. The violation of unitarity, however, is rather small, of the order $\mathcal{O}(M_D/M_N)$ as seen in Eq.(14.21). It is also severely constrained experimentally [22, 23]. For all these reasons, for all practical purposes, we will consider the U matrix for the 3ν mixing case to be unitary independently of whether neutrinos are Dirac or Majorana particles.

14.4 Mass-Induced Flavour Oscillations in Vacuum

If neutrinos have masses and lepton flavours are mixed in the weak CC interactions, lepton flavour is not conserved in neutrino propagation [19, 24]. This phenomenon is usually referred to as *neutrino oscillations*. In brief, a weak eigenstates, ν_α , which by default is the state produced in the weak CC interaction of a charged lepton ℓ_α , is the linear combination determined by the mixing matrix U

$$|\nu_\alpha\rangle = \sum_{i=1}^n U_{\alpha i}^* |\nu_i\rangle, \quad (14.35)$$

where ν_i are the mass eigenstates, and here n is the number of light neutrino species (implicit in our definition of the state $|\nu\rangle$ is its energy-momentum and space-time dependence). After traveling a distance L ($L \simeq ct$ for relativistic neutrinos), that state evolves as:

$$|\nu_\alpha(t)\rangle = \sum_{i=1}^n U_{\alpha i}^* |\nu_i(t)\rangle. \quad (14.36)$$

This neutrino can then undergo a charged-current (CC) interaction producing a charge lepton ℓ_β , $\nu_\alpha(t)N' \rightarrow \ell_\beta N$, with a probability

$$P_{\alpha\beta} = |\langle \nu_\beta | \nu_\alpha(t) \rangle|^2 = \left| \sum_{i=1}^n \sum_{j=1}^n U_{\alpha i}^* U_{\beta j} \langle \nu_j | \nu_i(t) \rangle \right|^2. \quad (14.37)$$

Assuming that $|\nu\rangle$ is a plane wave, $|\nu_i(t)\rangle = e^{-iE_i t} |\nu_i(0)\rangle$,³ with $E_i = \sqrt{p_i^2 + m_i^2}$ and m_i being, respectively, the energy and the mass of the neutrino mass eigenstate ν_i . In all practical cases neutrinos are very relativistic, so $p_i \simeq p_j \equiv p \simeq E$. We can then write

$$E_i = \sqrt{p_i^2 + m_i^2} \simeq p + \frac{m_i^2}{2E}, \quad (14.38)$$

and use the orthogonality of the mass eigenstates, $\langle \nu_j | \nu_i \rangle = \delta_{ij}$, to arrive to the following form for $P_{\alpha\beta}$:

$$\begin{aligned} P_{\alpha\beta} &= \delta_{\alpha\beta} - 4 \sum_{i<j}^n \text{Re}[U_{\alpha i} U_{\beta i}^* U_{\alpha j}^* U_{\beta j}] \sin^2 X_{ij} \\ &\quad + 2 \sum_{i<j}^n \text{Im}[U_{\alpha i} U_{\beta i}^* U_{\alpha j}^* U_{\beta j}] \sin 2X_{ij}, \end{aligned} \quad (14.39)$$

³ For a pedagogical discussion of the quantum mechanical description of flavour oscillations in the wave package approach see for example Ref. [3]. A recent review of the quantum mechanical aspects and subtleties on neutrino oscillations can be found in in Ref. [25].

where

$$X_{ij} = \frac{(m_i^2 - m_j^2)L}{4E} = 1.267 \frac{\Delta m_{ij}^2}{\text{eV}^2} \frac{L/E}{\text{m/MeV}}. \quad (14.40)$$

If we had made the same derivation for antineutrino states, we would have ended with a similar expression but with the exchange $U \rightarrow U^*$. Consequently, we conclude that the first term in the right-hand-side of Eq.(14.39) is CP conserving since it is the same for neutrinos and antineutrinos, while the last one is CP violating because it has opposite signs for neutrinos and antineutrinos.

Table 14.1: Characteristic values of L and E for experiments performed using various neutrino sources and the corresponding ranges of $|\Delta m^2|$ to which they can be most sensitive to flavour oscillations in vacuum. SBL stands for Short Baseline, VSBL stands for Very Short Baseline, MBL stands for Medium Baseline, and LBL for Long Baseline.

Experiment		L (m)	E (MeV)	$ \Delta m^2 $ (eV ²)
Solar		10^{10}	1	10^{-10}
Atmospheric		$10^4 - 10^7$	$10^2 - 10^5$	$10^{-1} - 10^{-4}$
Reactor	VSBL–SBL–MBL	$10 - 10^3$	1	$1 - 10^{-3}$
	LBL	$10^4 - 10^5$		$10^{-4} - 10^{-5}$
Accelerator	SBL	10^2	$10^3 - 10^4$	> 0.1
	LBL	$10^5 - 10^6$	$10^3 - 10^4$	$10^{-2} - 10^{-3}$

Equation (14.39) is oscillatory in distance with oscillation lengths

$$L_{0,ij}^{\text{osc}} = \frac{4\pi E}{|\Delta m_{ij}^2|}, \quad (14.41)$$

and with amplitudes proportional to products of elements in the mixing matrix. Thus, neutrinos must have different masses ($\Delta m_{ij}^2 \neq 0$) and they must have not vanishing mixing ($U_{\alpha i} U_{\beta i} \neq 0$) in order to undergo flavour oscillations. Also, from Eq.(14.39) we see that the Majorana phases cancel out in the oscillation probability. This is expected because flavour oscillation is a total lepton number conserving process.

Ideally, a neutrino oscillation experiment would like to measure an oscillation probability over a distance L between the source and the detector, for neutrinos of a definite energy E . In practice, neutrino beams, both from natural or artificial sources, are never monoenergetic but have an energy spectrum $\Phi(E)$. In addition, each detector has a finite energy resolution. Under these circumstances what is measured is an average probability

$$\begin{aligned} \langle P_{\alpha\beta} \rangle &= \frac{\int dE \frac{d\Phi}{dE} \sigma(E) P_{\alpha\beta}(E) \epsilon(E)}{\int dE \frac{d\Phi}{dE} \sigma_{CC}(E) \epsilon(E)} \\ &= \delta_{\alpha\beta} - 4 \sum_{i<j}^n \text{Re}[U_{\alpha i} U_{\beta i}^* U_{\alpha j}^* U_{\beta j}] \langle \sin^2 X_{ij} \rangle + 2 \sum_{i<j}^n \text{Im}[U_{\alpha i} U_{\beta i}^* U_{\alpha j}^* U_{\beta j}] \langle \sin 2X_{ij} \rangle. \end{aligned} \quad (14.42)$$

σ is the cross-section for the process in which the neutrino flavour is detected, and $\epsilon(E)$ is the detection efficiency. The minimal range of the energy integral is determined by the energy resolution of the experiment.

It is clear from the above expression that if $(E/L) \gg |\Delta m_{ij}^2|$ ($L \ll L_{0,ij}^{\text{osc}}$) so $\sin^2 X_{ij} \ll 1$, the oscillation phase does not give any appreciable effect. Conversely, if $L \gg L_{0,ij}^{\text{osc}}$, many oscillation

cycles occur between production and detection, so the oscillating term is averaged to $\langle \sin^2 X_{ij} \rangle = 1/2$.

We summarize in Table 14.1 the typical values of L/E for different types of neutrino sources and experiments and the corresponding ranges of Δm^2 to which they can be most sensitive.

Historically, the results of neutrino oscillation experiments were interpreted assuming two-neutrino states so there is only one oscillating phase; the mixing matrix depends on a single mixing angle θ , and no CP violation effect in oscillations is possible. At present, as we will discuss in Sec.14.7, we need at least the mixing among three-neutrino states to fully describe the bulk of experimental results. However, in many cases, the observed results can be understood in terms of oscillations dominantly driven by one Δm^2 . In this limit $P_{\alpha\beta}$ of Eq.(14.39) takes the form [24]

$$P_{\alpha\beta} = \delta_{\alpha\beta} - (2\delta_{\alpha\beta} - 1) \sin^2 2\theta \sin^2 X. \quad (14.43)$$

In this effective $2 - \nu$ limit, changing the sign of the mass difference, $\Delta m^2 \rightarrow -\Delta m^2$, and changing the octant of the mixing angle, $\theta \rightarrow \frac{\pi}{2} - \theta$, is just redefining the mass eigenstates, $\nu_1 \leftrightarrow \nu_2$: $P_{\alpha\beta}$ must be invariant under such transformation. So the physical parameter space can be covered with either $\Delta m^2 \geq 0$ with $0 \leq \theta \leq \frac{\pi}{2}$, or, alternatively, $0 \leq \theta \leq \frac{\pi}{4}$ with either sign for Δm^2 .

However, from Eq.(14.43) we see that $P_{\alpha\beta}$ is actually invariant under the change of sign of the mass splitting *and* the change of octant of the mixing angle separately. This implies that there is a two-fold discrete ambiguity since the two different sets of physical parameters, $(\Delta m^2, \theta)$ and $(\Delta m^2, \frac{\pi}{2} - \theta)$, give the same transition probability in vacuum. In other words, one could not tell from a measurement of, say, $P_{e\mu}$ in vacuum whether the larger component of ν_e resides in the heavier or in the lighter neutrino mass eigenstate. This symmetry is broken when one considers mixing of three or more neutrinos in the flavour evolution and or when the neutrinos traverse regions of dense matter as we describe in Sec.14.7.1 and Sec.14.5, respectively.

14.5 Propagation of Massive Neutrinos in Matter

Neutrinos propagating in a dense medium can interact with the particles in the medium. The probability of an incoherent inelastic scattering is very small. For example the characteristic cross section for ν -proton scattering is of the order

$$\sigma \sim \frac{G_F^2 s}{\pi} \sim 10^{-43} \text{ cm}^2 \left(\frac{E}{\text{MeV}} \right)^2, \quad (14.44)$$

where G_F is the Fermi constant and s is the square of the center of mass energy of the collision.

But when neutrinos propagate in dense matter, they can also interact coherently with the particles in the medium. By definition, in coherent interactions, the medium remains unchanged so it is possible to have interference of the forward scattered and the unscattered neutrino waves which enhances the effect of matter in the neutrino propagation. In this case, the effect of the medium is not on the intensity of the propagating neutrino beam, which remains unchanged, but on the phase velocity of the neutrino wave, and for this reason the effect is proportional to G_F , instead of the G_F^2 dependence of the incoherent scattering. Coherence also allows decoupling the evolution equation of the neutrinos from those of the medium. In this limit, the effect of the medium is introduced in the evolution equation for the neutrinos in the form of an effective potential which depends on the density and composition of the matter [26].

As an example, let us consider the evolution of ν_e in a medium with electrons, protons, and neutrons with corresponding n_e , n_p , and n_n number densities. The effective low-energy Hamiltonian describing the relevant neutrino interactions at point x is given by

$$H_W = \frac{G_F}{\sqrt{2}} \left[J^{(+)\alpha}(x) J_\alpha^{(-)}(x) + \frac{1}{4} J^{(N)\alpha}(x) J_\alpha^{(N)}(x) \right], \quad (14.45)$$

where the J_α 's are the standard fermionic currents

$$J_\alpha^{(+)}(x) = \bar{\nu}_e(x)\gamma_\alpha(1 - \gamma_5)e(x), \quad (14.46)$$

$$J_\alpha^{(-)}(x) = \bar{e}(x)\gamma_\alpha(1 - \gamma_5)\nu_e(x), \quad (14.47)$$

$$\begin{aligned} J_\alpha^{(N)}(x) &= \bar{\nu}_e(x)\gamma_\alpha(1 - \gamma_5)\nu_e(x) \\ &\quad - \bar{e}(x)[\gamma_\alpha(1 - \gamma_5) - 4\sin^2\theta_W\gamma_\alpha]e(x) \\ &\quad + \bar{p}(x)[\gamma_\alpha(1 - g_A^{(p)}\gamma_5) - 4\sin^2\theta_W\gamma_\alpha]p(x) \\ &\quad - \bar{n}(x)\gamma_\alpha(1 - g_A^{(n)}\gamma_5)n(x), \end{aligned} \quad (14.48)$$

and $g_A^{(n,p)}$ are the axial couplings for neutrons and protons, respectively.

Let us focus first on the effect of the charged current interactions. The effective CC Hamiltonian due to electrons in the medium is

$$\begin{aligned} H_C^{(e)} &= \frac{G_F}{\sqrt{2}} \int d^3p_e f(E_e, T) \times \left\langle \langle e(s, p_e) | \bar{e}(x)\gamma_\alpha(1 - \gamma_5)\nu_e(x)\bar{\nu}_e(x)\gamma_\alpha(1 - \gamma_5)e(x) | e(s, p_e) \rangle \right\rangle \\ &= \frac{G_F}{\sqrt{2}} \bar{\nu}_e(x)\gamma_\alpha(1 - \gamma_5)\nu_e(x) \int d^3p_e f(E_e, T) \left\langle \langle e(s, p_e) | \bar{e}(x)\gamma_\alpha(1 - \gamma_5)e(x) | e(s, p_e) \rangle \right\rangle. \end{aligned} \quad (14.49)$$

In the above equation, we denote by s the electron spin, and by p_e its momentum, and $f(E_e, T)$ is the energy distribution function of the electrons in the medium which is assumed to be homogeneous and isotropic and is normalized as

$$\int d^3p_e f(E_e, T) = 1. \quad (14.50)$$

We denote by $\langle \dots \rangle$ the averaging over electron spinors and summing over all electrons in the medium. Coherence dictates that s, p_e are the same for initial and final electrons. The axial current reduces to the spin in the non-relativistic limit and therefore averages to zero for a background of non-relativistic electrons. The spatial components of the vector current cancel because of isotropy. Therefore, the only non-trivial average is

$$\int d^3p_e f(E_e, T) \left\langle \langle e(s, p_e) | \bar{e}(x)\gamma_0 e(x) | e(s, p_e) \rangle \right\rangle = n_e(x), \quad (14.51)$$

which gives a contribution to the effective Hamiltonian

$$H_C^{(e)} = \sqrt{2}G_F n_e \bar{\nu}_{eL}(x)\gamma_0\nu_{eL}(x). \quad (14.52)$$

This can be interpreted as a contribution to the ν_{eL} potential energy

$$V_C = \sqrt{2}G_F n_e. \quad (14.53)$$

Should we have considered antineutrino states, we would have ended up with $V_C = -\sqrt{2}G_F n_e$. For a more detailed derivation of the matter potentials see, for example, Ref. [3].

With an equivalent derivation, we find that for ν_μ and ν_τ , the potential due to its CC interactions is zero for most media since neither μ 's nor τ 's are present, while the effective potential for any active neutrino due to the neutral current interactions is found to be

$$V_{NC} = \frac{\sqrt{2}}{2}G_F \left[-n_e(1 - 4\sin^2\theta_w) + n_p(1 - 4\sin^2\theta_w) - n_n \right]. \quad (14.54)$$

In neutral matter, $n_e = n_p$ and the contribution from electrons and protons cancel each other. So we are left only with the neutron contribution

$$V_{NC} = -1/\sqrt{2}G_F n_n. \quad (14.55)$$

After including these effects, the evolution equation for n ultrarelativistic neutrinos propagating in matter written in the mass basis is (see for instance Ref. [27–29] for the derivation):

$$i \frac{d\vec{\nu}}{dx} = H \vec{\nu}, \quad H = H_m + U^{\nu\dagger} V U^\nu. \quad (14.56)$$

Here $\vec{\nu} \equiv (\nu_1, \nu_2, \dots, \nu_n)^T$, H_m is the kinetic Hamiltonian,

$$H_m = \frac{1}{2E} \text{diag}(m_1^2, m_2^2, \dots, m_n^2), \quad (14.57)$$

and V is the effective neutrino potential in the interaction basis. U^ν is the $n \times n$ submatrix of the unitary V^ν matrix corresponding to the n ultrarelativistic neutrino states. For the three SM active neutrinos with purely SM interactions crossing a neutral medium with electrons, protons and neutrons, the evolution equation takes the form (14.56) with $U^\nu \equiv U$, and the effective potential:

$$V = \text{diag}(\pm\sqrt{2}G_F n_e(x), 0, 0) \equiv \text{diag}(V_e, 0, 0). \quad (14.58)$$

The sign $+$ ($-$) in Eq.(14.58) applies to neutrinos (antineutrinos), and $n_e(x)$ is the electron number density in the medium, which in general is not constant along the neutrino trajectory so the potential is not constant. The characteristic value of the potential at the Earth core is $V_e \sim 10^{-13}$ eV, while at the solar core $V_e \sim 10^{-12}$ eV. Since the neutral current potential Eq.(14.55) is flavour diagonal, it can be eliminated from the evolution equation as it only contributes to an overall unobservable phase.

The instantaneous mass eigenstates in matter, ν_i^m , are the eigenstates of the Hamiltonian H in (14.56) for a fixed value of x , and they are related to the interaction basis by

$$\vec{\nu} = \tilde{U}(x) \nu^{\vec{m}}. \quad (14.59)$$

The corresponding instantaneous eigenvalues of H are $\mu_i(x)^2/(2E)$ with $\mu_i(x)$ being the instantaneous effective neutrino masses.

Let us take for simplicity a neutrino state which is an admixture of only two neutrino species $|\nu_\alpha\rangle$ and $|\nu_\beta\rangle$, so the two instantaneous mass eigenstates in matter ν_1^m and ν_2^m have instantaneous effective neutrino masses

$$\begin{aligned} \mu_{1,2}^2(x) &= \frac{m_1^2 + m_2^2}{2} + E[V_\alpha + V_\beta] \\ &\mp \frac{1}{2} \sqrt{[\Delta m^2 \cos 2\theta - A]^2 + [\Delta m^2 \sin 2\theta]^2}, \end{aligned} \quad (14.60)$$

and $\tilde{U}(x)$ is a 2x2 rotation matrix with the instantaneous mixing angle in matter given by

$$\tan 2\theta_m = \frac{\Delta m^2 \sin 2\theta}{\Delta m^2 \cos 2\theta - A}. \quad (14.61)$$

In the Eqs.(14.60) and (14.61) A is

$$A \equiv 2E(V_\alpha - V_\beta), \quad (14.62)$$

and its sign depends on the composition of the medium and on the flavour composition of the neutrino state considered. From the expressions above, we see that for a given sign of A the mixing angle in matter is larger(smaller) than in vacuum if this last one is in the first (second) octant. We see that the symmetry about $\theta = 45^\circ$ which exists in vacuum oscillations between two neutrino states is broken by the matter potential in propagation in a medium. The expressions above show that significant effects are present when A , is close to $\Delta m^2 \cos 2\theta$. In particular, as seen in Eq.(14.61), the tangent of the mixing angle changes sign if, along its path, the neutrino passes by some matter density region satisfying, for its energy, the *resonance condition*

$$A_R = \Delta m^2 \cos 2\theta. \quad (14.63)$$

This implies that if the neutrino is created in a region where the relevant potential satisfies $A_0 > A_R$ (A_0 here is the value of the relevant potential at the production point), then the effective mixing angle in matter at the production point is such that $\text{sgn}(\cos 2\theta_{m,0}) = -\text{sgn}(\cos 2\theta)$. So the flavour component of the mass eigenstates is inverted as compared to their composition in vacuum. In particular, if at the production point we have $A_0 = 2A_R$, then $\theta_{m,0} = \frac{\pi}{2} - \theta$. Asymptotically, for $A_0 \gg A_R$, $\theta_{m,0} \rightarrow \frac{\pi}{2}$. In other words, if in vacuum the lightest (heaviest) mass eigenstate has a larger projection on the flavour α (β), inside a matter with density and composition such that $A > A_R$, the opposite holds. So if the neutrino system is traveling across a monotonically varying matter potential, the dominant flavour component of a given mass eigenstate changes when crossing the region with $A = A_R$. This phenomenon is known as *level crossing*.

Taking the derivative of Eq.(14.59) with respect to x and using Eq.(14.56), we find that in the instantaneous mass basis the evolution equation reads:

$$i \frac{d\vec{\nu}^m}{dx} = \left[\frac{1}{2E} \text{diag} \left(\mu_1^2(x), \mu_2^2(x), \dots, \mu_n^2(x) \right) - i \tilde{U}^\dagger(x) \frac{d\tilde{U}(x)}{dx} \right] \vec{\nu}^m. \quad (14.64)$$

The presence of the last term, Eq.(14.64) implies that this is a system of coupled equations. So, in general, the instantaneous mass eigenstates, ν_i^m are not energy eigenstates. For constant or slowly enough varying matter potential this last term can be neglected and the instantaneous mass eigenstates, ν_i^m , behave approximately as energy eigenstates, and they do not mix in the evolution. This is the *adiabatic* transition approximation. On the contrary, when the last term in Eq.(14.64) cannot be neglected, the instantaneous mass eigenstates mix along the neutrino path. This implies there can be *level-jumping* [30–33], and the evolution is *non-adiabatic*.

For adiabatic evolution in matter, the oscillation probability take a form very similar to the vacuum oscillation expression, Eq.(14.39). For example, neglecting CP violation:

$$P_{\alpha\beta} = \left| \sum_i \tilde{U}_{\alpha i}(0) \tilde{U}_{\beta i}(L) \exp \left(-\frac{i}{2E} \int_0^L \mu_i^2(x') dx' \right) \right|^2. \quad (14.65)$$

To compute $P_{\alpha\beta}$ in a varying potential, one can always solve the evolution equation numerically. Also, several analytic approximations for specific profiles of the matter potential can be found in the literature [34].

14.5.1 The Mikheyev-Smirnov-Wolfenstein Effect for Solar Neutrinos

The matter effects discussed in the previous section are of special relevance for solar neutrinos. As the Sun produces ν_e 's in its core, we consider the propagation of a $\nu_e - \nu_X$ neutrino system (X is some superposition of μ and τ , which is arbitrary because ν_μ and ν_τ have only and equal neutral current interactions) in the matter density of the Sun.

The density of solar matter is a monotonically decreasing function of the distance R from the center of the Sun, and it can be approximated by an exponential for $R < 0.9R_\odot$

$$n_e(R) = n_e(0) \exp(-R/r_0) , \quad (14.66)$$

with $r_0 = R_\odot/10.54 = 6.6 \times 10^7 \text{ m} = 3.3 \times 10^{14} \text{ eV}^{-1}$.

As mentioned above, the nuclear reactions in the Sun produce electron neutrinos. After crossing the Sun, the composition of the neutrino state exiting the Sun will depend on the relative size of $\Delta m^2 \cos 2\theta$ versus $A_0 = 2 E G_F n_{e,0}$ (where 0 refers to the neutrino production point, which is near but not exactly at the center of the Sun, $R = 0$).

If the relevant matter potential at production is well below the resonant value, $A_R = \Delta m^2 \cos 2\theta \gg A_0$, matter effects are negligible. With the characteristic matter density and energy of the solar neutrinos, this condition is fulfilled for values of Δm^2 such that $\Delta m^2/E \gg L_{\text{Sun-Earth}}$. So the propagation occurs as in vacuum with the oscillating phase averaged to $1/2$ and the survival probability at the exposed surface of the Earth is

$$P_{ee}(\Delta m^2 \cos 2\theta \gg A_0) = 1 - \frac{1}{2} \sin^2 2\theta > \frac{1}{2} . \quad (14.67)$$

If the relevant matter potential at production is only slightly below the resonant value, $A_R = \Delta m^2 \cos 2\theta \gtrsim A_0$, the neutrino does not cross a region with resonant density, but matter effects are sizable enough to modify the mixing. The oscillating phase is averaged in the propagation between the Sun and the Earth. This regime is well described by an adiabatic propagation, Eq.(14.65). Using that $\tilde{U}(0)$ is a 2x2 rotation of angle $\theta_{m,0}$ – the mixing angle in matter at the neutrino production point–, and $\tilde{U}(L)$ is the corresponding rotation with vacuum mixing angle θ , we get

$$P_{ee}(\Delta m^2 \cos 2\theta \geq A_0) = \cos^2 \theta_{m,0} \cos^2 \theta + \sin^2 \theta_{m,0} \sin^2 \theta = \frac{1}{2} [1 + \cos 2\theta_{m,0} \cos 2\theta] . \quad (14.68)$$

This expression reflects that an electron neutrino produced at A_0 is an admixture of ν_1 with fraction $P_{e1,0} = \cos^2 \theta_{m,0}$ and ν_2 with fraction $P_{e2,0} = \sin^2 \theta_{m,0}$. On exiting the Sun, ν_1 consists of ν_e with fraction $P_{1e} = \cos^2 \theta$, and ν_2 consists of ν_e with fraction $P_{2e} = \sin^2 \theta$ so $P_{ee} = P_{e1,0}P_{1e} + P_{e2,0}P_{2e} = \cos^2 \theta_{m,0} \cos^2 \theta + \sin^2 \theta_{m,0} \sin^2 \theta$ [35–37], exactly as given in Eq.(14.68). Since $A_0 < A_R$ the resonance is not crossed so $\cos 2\theta_{m,0}$ has the same sign as $\cos 2\theta$ and still $P_{ee} \geq 1/2$.

Finally, in the case that $A_R = \Delta m^2 \cos 2\theta < A_0$, the neutrino can cross the resonance on its way out. In the convention of $\Delta m^2 > 0$ this occurs if $\cos 2\theta > 0$ ($\theta < \pi/4$). which means that in vacuum ν_e is a combination of ν_1 and ν_2 with a larger ν_1 component, while at the production point ν_e is a combination of ν_1^m and ν_2^m with larger ν_2^m component. In particular, if the density at the production point is much higher than the resonant density, $\Delta m^2 \cos 2\theta \ll A_0$,

$$\theta_{m,0} = \frac{\pi}{2} \quad \Rightarrow \quad \cos 2\theta_{m,0} = -1 , \quad (14.69)$$

and the produced ν_e is purely ν_2^m .

In this regime, the evolution of the neutrino ensemble can be adiabatic or non-adiabatic depending on the particular values of Δm^2 and the mixing angle. The oscillation parameters (see Secs.14.6.1 and 14.7) happen to be such that the transition is adiabatic in all ranges of solar neutrino energies. Thus the survival probability at the exposed surface of the Earth is given by Eq.(14.68) but now with mixing angle (14.69) so

$$P_{ee}(\Delta m^2 \cos 2\theta < A_0) = \frac{1}{2} [1 + \cos 2\theta_{m,0} \cos 2\theta] = \sin^2 \theta . \quad (14.70)$$

So, in this case, P_{ee} can be much smaller than $1/2$ because $\cos 2\theta_{m,0}$ and $\cos 2\theta$ have opposite signs. This is referred to as the Mikheev-Smirnov-Wolfenstein (MSW) effect [26, 38], which plays a fundamental role in the interpretation of the solar neutrino data.

The resulting energy dependence of the survival probability of solar neutrinos is shown in Fig.14.3 (together with a compilation of data from solar experiments). The plotted curve corresponds to $\Delta m^2 \sim 7.5 \times 10^{-5} \text{ eV}^2$ and $\sin^2 \theta \sim 0.3$ (the so-called large mixing angle, LMA, solution). The figure illustrates the regimes described above. For these values of the oscillation parameters, neutrinos with $E \ll 1 \text{ MeV}$ are in the regime with $\Delta m^2 \cos 2\theta \gg A_0$ so the curve represents the value of vacuum averaged survival probability, Eq.(14.67), and therefore $P_{ee} > 0.5$. For $E > 10 \text{ MeV}$, on the contrary, $\Delta m^2 \cos 2\theta \ll A_0$ and the survival probability is given by Eq.(14.70), so $P_{ee} = \sin^2 \theta \sim 0.3$. In between, the survival probability is given by Eq.(14.68) with θ_0 changing rapidly from its vacuum value to the asymptotic matter value (14.69), 90° .

14.6 Experimental Study of Neutrino Oscillations

Neutrino flavour transitions, or neutrino oscillations, have been experimentally studied using various neutrino sources and detection techniques. Intense sources and large detectors are mandatory because of a large distance necessary for observable oscillation effects in addition to the tiny cross-sections. Also, the relevant neutrino flux before oscillations should be known with sufficient precision for a definitive measurement. Here, the experimental status of neutrino oscillations with the different neutrino sources: the Sun, Earth's atmosphere, accelerators, and nuclear reactors are reviewed.

14.6.1 Solar Neutrinos

14.6.1.1 Solar neutrino flux

In the Sun, electron neutrinos are produced in the thermonuclear reactions which generate solar energy. These reactions occur via two main chains, the pp chain and the CNO cycle. The pp chain includes reactions $p + p \rightarrow d + e^+ + \nu$ (pp), $p + e^- + p \rightarrow d + \nu$ (pep), ${}^3\text{He} + p \rightarrow {}^4\text{He} + e^+ + \nu$ (hep), ${}^7\text{Be} + e^- \rightarrow {}^7\text{Li} + \nu(+\gamma)$ (${}^7\text{Be}$), and ${}^8\text{B} \rightarrow {}^8\text{Be}^* + e^+ + \nu$ (${}^8\text{B}$). The CNO cycle involves ${}^{13}\text{N} \rightarrow {}^{13}\text{C} + e^+ + \nu$ (${}^{13}\text{N}$), ${}^{15}\text{O} \rightarrow {}^{15}\text{N} + e^+ + \nu$ (${}^{15}\text{O}$), and ${}^{17}\text{F} \rightarrow {}^{17}\text{O} + e^+ + \nu$ (${}^{17}\text{F}$). Those reactions result in the overall fusion of protons into ${}^4\text{He}$, $4p \rightarrow {}^4\text{He} + 2e^+ + 2\nu_e$, where the energy released in the reaction, $Q = 4m_p - m_{{}^4\text{He}} - 2m_e \sim 26 \text{ MeV}$, is mostly radiated through the photons and only a small fraction is carried by the neutrinos, $\langle E_{2\nu_e} \rangle = 0.59 \text{ MeV}$. In addition, electron capture on ${}^{13}\text{N}$, ${}^{15}\text{O}$, and ${}^{17}\text{F}$ produces line spectra of neutrinos called ecCNO neutrinos. Dividing the solar luminosity by the energy released per neutrino production, the total neutrino flux can be estimated. At Earth, the pp solar neutrino flux is about $6 \times 10^{10} \text{ cm}^{-2}\text{s}^{-1}$.

The solar neutrino flux has been calculated based on the Standard Solar Model (SSM). The SSM describes the structure and evolution of the Sun based on a variety of inputs such as the mass, luminosity, radius, surface temperature, age, and surface elemental abundances. In addition, the knowledge of the absolute nuclear reaction cross sections for relevant fusion reactions and radiative opacities are necessary. John Bahcall and his collaborators continuously updated the SSM calculations over several decades [39, 40]. Figure 14.1 shows the solar neutrino fluxes predicted by the SSM calculation in [41] and ecCNO neutrinos in [42].

14.6.1.2 Detection of solar neutrinos and the solar neutrino problem

Experiments that observed solar neutrinos are summarized in Table 14.2. A pioneering solar neutrino experiment was carried out by R. Davis, Jr. and collaborators at Homestake starting in the late 1960s [44]. The Davis' experiment utilizes the reaction $\nu_e + {}^{37}\text{Cl} \rightarrow e^- + {}^{37}\text{Ar}$. Because this process has an energy threshold of 814 keV, the most relevant fluxes are the ${}^7\text{Be}$ and ${}^8\text{B}$ neutrinos. The detector contained $\sim 615 \text{ t}$ of C_2Cl_4 . The produced ${}^{37}\text{Ar}$, which has a half-life of 34.8 d,

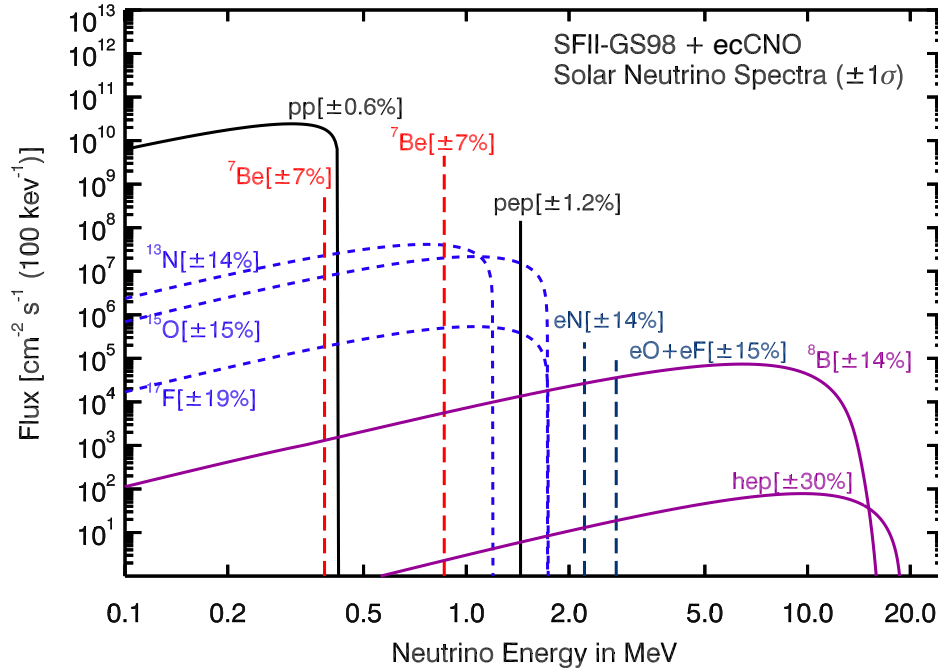


Figure 14.1: Spectrum of solar neutrino fluxes predicted by SSM calculation in [41]. In addition to standard fluxes, ecCNO neutrinos have been added based on [42]. Electron capture fluxes are given in $\text{cm}^{-2}\text{s}^{-1}$. Taken from [43].

Table 14.2: List of solar neutrino experiments

Name	Target material	Energy threshold (MeV)	Mass (ton)	Years
Homestake	C_2Cl_4	0.814	615	1970–1994
SAGE	Ga	0.233	50	1989–
GALLEX	GaCl_3	0.233	100 [30.3 for Ga]	1991–1997
GNO	GaCl_3	0.233	100 [30.3 for Ga]	1998–2003
Kamiokande	H_2O	6.5	3,000	1987–1995
Super-Kamiokande	H_2O	3.5	50,000	1996–
SNO	D_2O	3.5	1,000	1999–2006
KamLAND	Liquid scintillator	0.5/5.5	1,000	2001–
Borexino	Liquid scintillator	0.19	300	2007–

was chemically extracted and introduced into a low-background proportional chamber every few months. The Auger electrons from electron capture of ^{37}Ar were counted to determine the reaction rate.

From the beginning, the observed number of neutrinos in the Homestake mine experiment was significantly smaller than the prediction by SSM — it was almost one-third. After thorough checks of both experimental and theoretical work, the discrepancy remained. This became to be known as the solar neutrino problem. The final result from the Homestake experiment is $2.56 \pm 0.16 \pm 0.16$ SNU [45], where SNU (solar neutrino unit) is a unit of event rate, $1 \text{ SNU} = 10^{-36}$ captures/(s atom). On the other hand, prediction based on SSM is $8.46_{-0.88}^{+0.87}$ SNU [46].

The detection of neutrinos from other production processes was recognized as an important input to investigate the origin of the solar neutrino problem. In particular, the pp neutrino is most abundant, and its flux prediction has the smallest uncertainty. Using the radiochemical technique with gallium, the reaction $\nu_e + {}^{71}\text{Ga} \rightarrow e^- + {}^{71}\text{Ge}$ has an energy threshold of 233 keV and can be used for the pp neutrino detection. According to the SSM, more than half of the events on ${}^{71}\text{Ga}$ are due to the pp neutrinos, with the second dominant contribution coming from the ${}^7\text{Be}$ neutrinos. ${}^{71}\text{Ge}$ decays via electron capture with a half-life of 11.4 d. The SAGE experiment in Baksan [47] used about 50 t of liquid metallic gallium as a target. The GALLEX experiment in LNGS [48] used 101 t of GaCl_3 , containing 30.3 t of gallium. Both experiments used natural gallium, containing 39.9% of ${}^{71}\text{Ga}$ isotope. GALLEX was followed by its successor GNO experiment. The measured capture rate is $69.3 \pm 4.1 \pm 3.6$ SNU for GALLEX+GNO [49] and $65.4^{+3.1+2.6}_{-3.0-2.8}$ SNU for SAGE [50]. A SSM prediction is $127.9^{+8.1}_{-8.2}$ SNU [46].

The radiochemical detectors measure the reaction rate integrated between extractions. The real-time measurement of solar neutrinos was realized by the Kamiokande experiment [51]. The Kamiokande detector was a 3,000-t water-Cherenkov detector in the Kamioka mine. Super-Kamiokande, the successor of Kamiokande, started operation in April 1996. It is a large upright cylindrical water Cherenkov detector containing 50 kt of pure water⁴. An inner detector volume corresponding to 32 kt water mass is viewed by more than 11,000 inward-facing 50 cm diameter photomultiplier tubes (PMTs). Kamiokande and Super-Kamiokande can observe solar neutrinos using ν - e elastic scattering (ES), $\nu_x + e^- \rightarrow \nu_x + e^-$. The ES reaction occurs via both charged and neutral current interactions. Consequently, it is sensitive to all active neutrino flavours, although the cross-section for ν_e , which is the only flavour to interact via charged current, is about six times larger than that for ν_μ or ν_τ . Because the energy threshold is 6.5 MeV for Kamiokande and 3.5 MeV for the present Super-Kamiokande (for the kinetic energy of recoil electron), these experiments are sensitive to primarily to ${}^8\text{B}$ neutrinos.

The results from Kamiokande [52, 53] and Super-Kamiokande [54, 55] showed significantly smaller numbers of observed solar neutrinos compared to the prediction. The latest ${}^8\text{B}$ neutrino flux measured by Super-Kamiokande is $(2.345 \pm 0.014 \pm 0.036) \times 10^6 \text{ cm}^{-2}\text{s}^{-1}$ [56], while a prediction based on the SSM is $(5.46 \pm 0.66) \times 10^6 \text{ cm}^{-2}\text{s}^{-1}$ [57]. In addition, no significant zenith angle variation nor spectrum distortion were observed in the initial phase of Super-Kamiokande, which placed strong constraints on the solution of the solar neutrino problem [58, 59].

14.6.1.3 Solution of the solar neutrino problem

The SNO experiment in Canada used 1,000 t of heavy water (D_2O) contained in a spherical acrylic vessel which was surrounded by an H_2O shield. An array of PMTs installed on a stainless steel structure detected Cherenkov radiation produced in both the D_2O and H_2O . The SNO detector observed ${}^8\text{B}$ neutrinos via three different reactions. In addition to the ES scattering with an electron, with D_2O target the CC $\nu_e + d \rightarrow e^- + p + p$ and the NC $\nu_x + d \rightarrow \nu_x + p + n$ interactions are possible. The CC reaction is sensitive to only ν_e , while NC reaction is sensitive to all active flavours of neutrinos with equal cross-sections. Therefore, by comparing the measurements of different reactions, SNO could provide a model-independent test of the neutrino flavour change.

In 2001, SNO reported the initial result of CC measurement [62]. Combined with the high statistics measurement of ν - e elastic scattering from Super-Kamiokande [58], it provided a direct evidence for the existence of non- ν_e component in solar neutrino flux. The result of the NC measurement in 2002 [63] established it with 5.3σ of statistical significance. Figure 14.2 shows the fluxes of electron neutrinos ($\phi(\nu_e)$) and muon and tau neutrinos ($\phi(\nu_{\mu,\tau})$) with the 68%, 95%, and 99% joint probability contours obtained with the SNO data. Finally, together with the reactor

⁴From 2020, gadolinium (0.01% by weight) is loaded in the water.

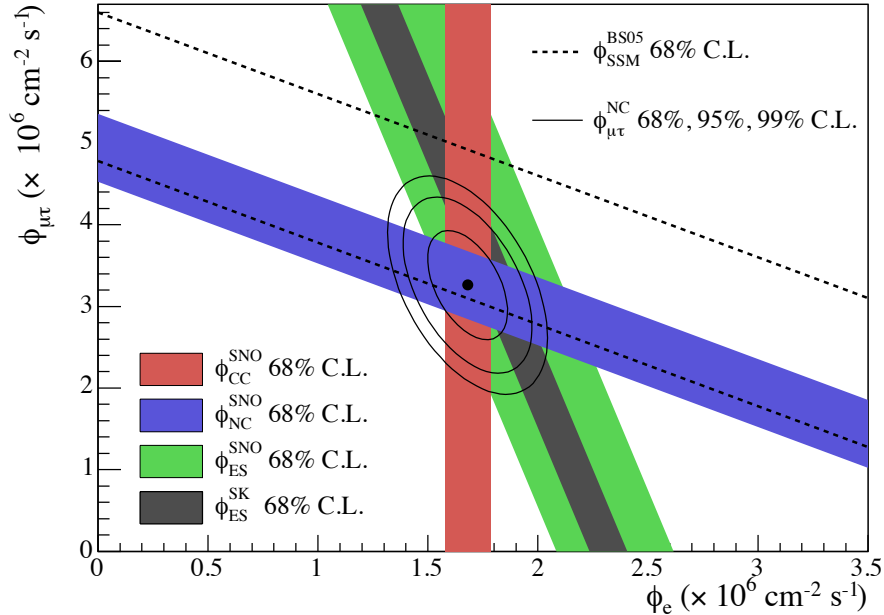


Figure 14.2: Fluxes of ${}^8\text{B}$ solar neutrinos, $\phi(\nu_e)$, and $\phi(\nu_{\mu,\tau})$, deduced from the SNO’s CC, ES, and NC results [60]. The Super-Kamiokande ES flux is from [61]. The BS05(OP) standard solar model prediction [40] is also shown. The bands represent the 1σ error. The contours show the 68%, 95%, and 99% joint probability for $\phi(\nu_e)$ and $\phi(\nu_{\mu,\tau})$. The figure is from [60].

neutrino experiment KamLAND (see Sec.14.6.4), the solution of solar neutrino problem was found to be the MSW adiabatic flavour transitions in the solar matter, the so-called large mixing angle (LMA) solution. From a combined result of three phases of SNO [64], the total flux of ${}^8\text{B}$ solar neutrino is found to be $(5.25 \pm 0.16_{-0.13}^{+0.11}) \text{ cm}^{-2}\text{s}^{-1}$, consistent with the SSM prediction. This consistency is one of the major accomplishments of SSM.

In order to understand the SSM as well as to study the MSW effect for the solar neutrino, measurements of solar neutrinos other than ${}^8\text{B}$ are important. The Borexino experiment at Gran Sasso, Italy, detects solar neutrino via ν - e scattering in real-time with a low energy threshold. The Borexino detector consists of 300 t of ultra-pure liquid scintillator, which achieved 0.19 MeV of energy threshold and 5% energy resolution at 1 MeV. Borexino reported the first real-time detection of ${}^7\text{Be}$ solar neutrinos [66]. They also measured the fluxes of pep [67], pp [68], and CNO [69] neutrino for the first time. Together with ${}^8\text{B}$ [70] neutrino measurement, Borexino provides important data to study the MSW effect. The KamLAND experiment also measured ${}^8\text{B}$ [71] and ${}^7\text{Be}$ [72] solar neutrinos.

Figure 14.3 shows the survival probability of solar ν_e as a function of neutrino energy. The data points are from the Borexino results [73,74] and the SNO+SK ${}^8\text{B}$ data. The theoretical curve shows the prediction of the MSW-LMA solution. All the data shown in this plot are consistent with the theoretically calculated curve. This indicates that these solar neutrino measurements are consistent with the MSW-LMA solution of the solar neutrino problem.

The matter effects can also be relevant to the propagation of solar neutrinos through the Earth. Because solar neutrinos go through the Earth before interaction in the detector during the nighttime, a comparison of measured event rate between daytime and nighttime provides a clean and direct test of matter effects on neutrino oscillations. Super-Kamiokande reported the indication of the day/night asymmetry in ${}^8\text{B}$ solar neutrinos [75,76]. The measured asymmetry, defined as the

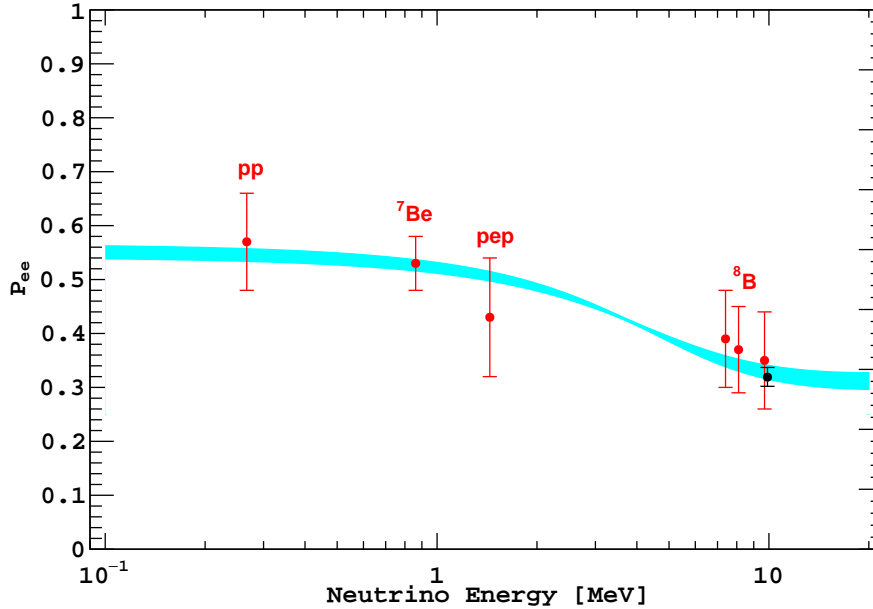


Figure 14.3: Electron neutrino survival probability as a function of neutrino energy. The points represent, from left to right, the Borexino pp, ${}^7\text{Be}$, pep, and ${}^8\text{B}$ data (red points) and the SNO+SK ${}^8\text{B}$ data (black point). The three Borexino ${}^8\text{B}$ data points correspond, from left to right, to the low-energy (LE) range, LE+HE range, and the high-energy (HE) range. The electron neutrino survival probabilities from experimental points are determined using a high metallicity SSM from Ref. [57]. The error bars represent the $\pm 1\sigma$ experimental + theoretical uncertainties. The curve corresponds to the $\pm 1\sigma$ prediction of the MSW-LMA solution using the parameter values given in [65]. This figure is provided by A. Ianni.

difference of the average day rate and average night rate divided by the average of those two rates, is $(-3.3 \pm 1.0 \pm 0.5)\%$, corresponding to a statistical significance of 2.9σ .

14.6.2 Atmospheric Neutrinos

14.6.2.1 Atmospheric neutrino flux

Atmospheric neutrinos are produced by the decays of pions and kaons generated in the interaction of cosmic rays and nucleons in the Earth's atmosphere. They have a broad range of energy (~ 0.1 GeV to $> \text{TeV}$) and long travel distances before detection (~ 10 to $\sim 10^4$ km), and contain all the flavours of neutrinos and antineutrinos.

Considering their dominant production modes, some generic relations for flux ratios of different flavours of neutrinos can be derived without detailed calculations. From the decay chain of a charged pion $\pi^+ \rightarrow \mu^+ \nu_\mu$ followed by $\mu^+ \rightarrow e^+ \nu_e \bar{\nu}_\mu$ (and the charge conjugate for π^-), the ratio $(\nu_\mu + \bar{\nu}_\mu)/(\nu_e + \bar{\nu}_e)$ is expected to be around 2 at low energies (~ 1 GeV), where most muons decay in the atmosphere. For higher energies, some muons reach the Earth before they decay and the ratio increases. One can also expect that the zenith angle distributions of atmospheric neutrinos are symmetric between upward-going and downward-going neutrinos. It is true for the energy above 1 GeV, but at lower energies, the Earth's geomagnetic field induces up-down asymmetries in the primary cosmic ray. The zenith angle corresponds to the flight length of atmospheric neutrinos. Vertically upward-going neutrinos come from the other side of the Earth with flight lengths of $\sim 10^4$ km, while downward-going neutrinos produced just above the experimental site travel ~ 10 km

before detection.

The atmospheric neutrino fluxes are calculated in detail based on the energy spectrum and composition of primary cosmic rays and their hadronic interactions in the atmosphere. The effects of solar activity and geomagnetic field are also taken into account. Results of calculations by several groups are available [77–80]. A typical uncertainty of the absolute flux is 10–20%, while the ratio of fluxes between different flavour has much smaller uncertainty ($< 5\%$).

14.6.2.2 Observation of atmospheric neutrino oscillations

The first detection of atmospheric neutrinos was reported in the 1960's by the underground experiments in the Kolar Gold Field experiment in India [81] and in South Africa [82]. In the 1980's, experiments searching for nucleon decays started operation. They used large underground detectors which could also observe atmospheric neutrinos that were studied as backgrounds to nucleon decays. Among the early experiments were Kamiokande [83] and IMB [84] using water Cherenkov detectors, and Frejus [85] and NUSEX [86] using iron tracking calorimeters.

The flavour of an atmospheric neutrino can be identified in charged current interaction with nuclei, which produces the corresponding charged lepton. Those detectors originally designed for nucleon decay search had the capability to distinguish muons and electrons. For example, a water Cherenkov detector can utilize the information from Cherenkov ring patterns for particle identification; e -like particles (e^\pm, γ) produce more diffuse ring than μ -like particles (μ^\pm, π^\pm) because of electromagnetic cascades and multiple Coulomb scattering effects.

To reduce the uncertainty, in early results the flux ratio $\nu_\mu/\nu_e \equiv (\nu_\mu + \bar{\nu}_\mu)/(\nu_e + \bar{\nu}_e)$ was measured, and the double ratio between observation and expectation $(\nu_\mu/\nu_e)_{\text{obs}}/(\nu_\mu/\nu_e)_{\text{exp}}$ was reported. The Kamiokande experiment reported an indication of a deficit of $(\nu_\mu + \bar{\nu}_\mu)$ flux [83]. IMB also observed a similar deficit [84], but measurements by Frejus [85] and NUSEX [86] were consistent with the expectations. This was called the atmospheric neutrino anomaly. Kamiokande reported studies with an increased data set of the sub-GeV (< 1.33 GeV) [87] as well as the multi-GeV (> 1.33 GeV) [88] samples. In the latter, they reported an analysis of zenith angle distributions, which showed an indication that the muon disappearance probability is dependent on the zenith angle, hence the travel length of neutrinos. However, the statistical significance was not sufficient to provide a conclusive interpretation.

The solution to the atmospheric neutrino anomaly was brought by Super-Kamiokande, which reported compelling evidence for neutrino oscillations in atmospheric neutrinos in 1998 [89]. The zenith angle (θ_z , with $\theta_z = 0$ for vertically downward-going) distributions of μ -like events showed a clear deficit of upward-going events, while no significant asymmetry was observed for e -like events. The asymmetry is defined as $A = (U - D)/(U + D)$, where U is the number of upward-going ($-1 < \cos \theta_z < -0.2$) events and D is the number of downward-going ($0.2 < \cos \theta_z < 1.0$) events. With multi-GeV (visible energy > 1.33 GeV) μ -like events alone, the measured asymmetry was $A = -0.296 \pm 0.048 \pm 0.001$, deviating from zero by more than 6σ . The sub-GeV (< 1.33 GeV) μ -like, upward through going, and upward stopping μ samples which correspond to different energy ranges of neutrinos, showed the consistent behaviour which strengthens the credibility of the observation. Super-Kamiokande's results were confirmed by other atmospheric neutrino observations MACRO [90] and Soudan2 [91].

Although the energy and zenith-angle-dependent muon neutrino disappearance observed with atmospheric neutrinos could be consistently explained by the neutrino oscillations predominantly between ν_μ and ν_τ , other exotic explanations such as neutrino decay [92] or decoherence [93] were not initially ruled out. By using a selected sample from Super-Kamiokande's atmospheric data with good L/E resolution, the L/E dependence of the survival probability was measured [94]. The observed dip in the L/E distribution was consistent with the expectation from neutrino oscillation,

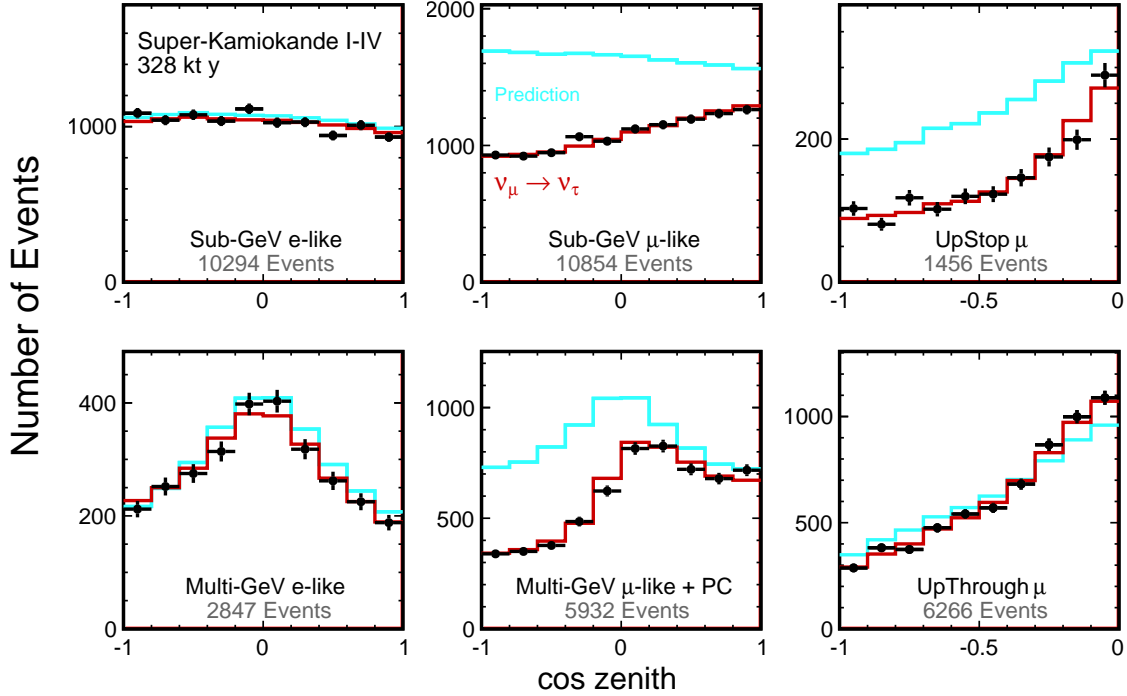


Figure 14.4: The zenith angle distributions of Super-Kamiokande atmospheric neutrino events. A data set corresponding to 328 kton-years of exposure is used. Fully contained 1-ring e -like and μ -like events with visible energy < 1.33 GeV (sub-GeV) and > 1.33 GeV (multi-GeV), as well as upward stopping and upward through going μ samples are shown. Partially contained (PC) events are combined with multi-GeV μ -like events. The blue histograms show the non-oscillated Monte Carlo events, and the red histograms show the best-fit expectations for neutrino oscillations. (This figure is provided by the Super-Kamiokande Collaboration)

while alternative models were strongly disfavored.

As an experimental proof of ν_μ - ν_τ oscillation, an appearance signal of ν_τ was searched for in the atmospheric neutrino data. Because of the high energy threshold (> 3.5 GeV) of ν_τ CC interaction and the short lifetime of τ lepton (0.3 ps), identifying the appearance of ν_τ experimentally is challenging. Super-Kamiokande reported evidence of tau neutrino appearance using atmospheric neutrino data with 4.6σ significance [95]. The definitive observation of ν_τ appearance was made by the long-baseline experiment, OPERA (See Sec.14.6.3.3), and recently IceCube also reported the ν_τ appearance analysis [96] using atmospheric neutrinos.

14.6.2.3 Neutrino oscillation measurements using atmospheric neutrinos

Figure 14.4 shows the zenith angle distributions of atmospheric neutrino data from Super-Kamiokande. For a wide range of neutrino energy and path length, the observed distributions are consistent with the expectation from neutrino oscillation. Atmospheric neutrinos in the energy region of a few to ~ 10 GeV provide information for the determination of the neutrino mass ordering [97].

The neutrino telescopes primarily built for high-energy neutrino astronomy such as ANTARES and IceCube can also measure neutrino oscillations with atmospheric neutrinos. ANTARES consists of a sparse array of PMTs deployed under the Mediterranean Sea at a depth of about 2.5 km to instrument a 10^5 m³ volume. IceCube is a detector deployed in ice in Antarctica at the South

Pole, at a depth between 1.45 and 2.45 km. In the bottom center of IceCube there is a region of $\sim 10^7$ m³ volume with denser PMT spacing called DeepCore to extend the observable energies to the lower energy region. By observing the charged current interaction of up-going ν_μ , they measure the ν_μ disappearance. ANTARES reported a measurement of ν_μ disappearance with 20 GeV threshold [98]. With analysis of events with 6–56 GeV energy range, the results on ν_μ disappearance measurements from IceCube DeepCore [99] provided a precision comparable to the measurements by Super-Kamiokande and long-baseline accelerator neutrino experiments.

There are several projects for atmospheric neutrino observations either proposed or under preparation. The atmospheric neutrino observation program is included in the plans for future neutrino telescopes such as ORCA in the KM3NeT project [100] in the Mediterranean Sea and the IceCube Upgrade [101]. In India, a 50 kt magnetized iron tracking calorimeter ICAL is planned at the INO [102]. Future large underground detectors, Hyper-Kamiokande in Japan [103] and DUNE in US [104] can also study the atmospheric neutrinos.

14.6.3 Accelerator Neutrinos

14.6.3.1 Accelerator neutrino beams

A comprehensive description of the accelerator neutrino beams is found in [105]. Conventional neutrino beams from accelerators are produced by colliding high-energy protons onto a target, producing π and K , which then decay into neutrinos. Undecayed mesons and muons are stopped in a beam dump and soil. Because pions are the most abundant product of the high energy collisions, a conventional neutrino beam contains a dominant amount of muon-type neutrinos (or antineutrinos).

Focusing devices called magnetic horns are used to concentrate the neutrino beam flux towards the desired direction [106]. A magnetic horn is a pulsed electromagnet with toroidal magnetic fields to focus charged particles that are parents of neutrinos. One can choose the dominant component of the beam to be either neutrinos or antineutrinos by selecting the direction of current in the magnetic horns. Even with the focusing with horns, *wrong sign* neutrinos contaminate in the beam. Also, there is a small amount of contamination of ν_e and $\bar{\nu}_e$ coming primarily from kaon and muon decays.

In order to maximize the sensitivity of the experiment, the ratio of baseline and neutrino energy (L/E) should be chosen to match the oscillation effects to be studied. In addition to maximizing the flux of neutrinos with relevant energy, neutrinos with irrelevant energy that result in unwanted background process should be suppressed. The energy of a neutrino from a pion decay is

$$E_\nu = \frac{[1 - (m_\mu/m_\pi)^2]E_\pi}{1 + \gamma^2\theta^2}, \quad (14.71)$$

where E_ν and E_π are the energy of neutrino and pion, respectively, θ is the angle between the pion and neutrino direction, and $\gamma = E_\pi/m_\pi$. For $\theta = 0$, the energy of neutrino is linearly proportional to the energy of pion. In this case, a narrow band beam can be made by selecting the momentum of pions. On the other hand, for $\theta \neq 0$, the energy of neutrino is not strongly dependent on the parent energy for a wide range of pion energy, but dependent on the off-axis angle θ . Using this relation, a neutrino beam with narrow energy spectrum, around the energy determined by θ , can be produced. This off-axis beam method was first introduced for BNL E889 proposal [107] and adopted in T2K and NOvA experiments. For a list of neutrino beamlines, see also Chapter 33 of this *Review*, “Neutrino Beam Lines at High-Energy Proton Synchrotrons.”

As indicated in Table 14.1, there are two different scales of baselines for accelerator-based experiments to study different ranges of Δm^2 . The atmospheric mass splitting $\Delta m^2 \sim 2.5 \times 10^{-3}$ eV² gives rise to the first oscillation maximum at $L/E \sim 500$ GeV/km. In order to study

this parameter region with a ~ 1 GeV accelerator neutrino beam, a long baseline of a few hundred to a thousand km is necessary. On the other hand, there have been reports of possible neutrino oscillations at the ~ 1 eV² scale, which can be studied at ~ 1 km baseline with neutrinos from accelerators. These experiments are called short-baseline oscillation experiments.

The flux of a neutrino beam is calculated using Monte Carlo simulation based on the configuration of the beamline. An important ingredient of the neutrino flux prediction is the hadron production cross-section. Data from dedicated hadron production experiments [108–110] are used to tune the beam simulation and constrain the uncertainty. The uncertainty of predicted neutrino flux for the most relevant energy region is ~ 5 –10% with the latest hadron production data [111–113].

14.6.3.2 Near detectors and neutrino interaction cross sections

Many long-baseline experiments use two detectors to reduce the systematic uncertainties arising from neutrino flux and neutrino-nucleus interactions. The near detectors either use the same technology as the far detector or consist of sub-detectors with complementary functions to obtain detailed information of the neutrino beam and interactions. The near detectors provide information for the neutrino flux, energy spectrum, and the interaction cross-sections, which is used as input to make predictions of observables at the far detector. However, even with the two-detector configuration, one should note that the neutrino flux is inevitably different between the near and the far detectors. In addition to the fact that the neutrino source looks like a line source for the near detector while it looks like a point source for the far detector, the neutrino oscillations alter the flavour composition of the neutrino beam quite significantly, as the design of a neutrino oscillation experiment requires.

For the precision measurements of neutrino oscillations with long-baseline experiments, the understanding of the neutrino-nucleus interaction becomes crucial. Because heavy nuclei are used as the interaction target, the nuclear effects complicate the understanding of the neutrino-nucleus interaction. For more information on the neutrino cross-sections, see also Chapter 52 of this *Review*, “Neutrino Cross Section Measurements.”

14.6.3.3 Long-baseline experiments

Table 14.3: List of long-baseline neutrino oscillation experiments

Name	Beamline	Far Detector	L (km)	E_ν (GeV)	Year
K2K	KEK-PS	Water Cherenkov	250	1.3	1999–2004
MINOS	NuMI	Iron-scintillator	735	3	2005–2013
MINOS+	NuMI	Iron-scintillator	735	7	2013–2016
OPERA	CNGS	Emulsion hybrid	730	17	2008–2012
ICARUS	CNGS	Liquid argon TPC	730	17	2010–2012
T2K	J-PARC	Water Cherenkov	295	0.6	2010–
NOvA	NuMI	Liquid scint. tracking calorimeter	810	2	2014–
DUNE	LBNF	Liquid argon TPC	1300	2–3	
Hyper-Kamiokande	J-PARC	Water Cherenkov	295	0.6	

Long-baseline neutrino oscillation experiments are summarized in Table 14.3. The first long-baseline experiment was the K2K experiment which used a neutrino beam from the KEK 12 GeV proton synchrotron directed towards Super-Kamiokande with a baseline of 250 km. The beam had an average energy of 1.3 GeV. The K2K near detectors, located 300 m downstream of the production target, consisted of a combination of a 1 kt water Cherenkov detector and a set of

fine-grained detectors. K2K confirmed the muon neutrino disappearance originally reported by Super-Kamiokande atmospheric neutrino observation [114].

The MINOS experiment used a beam from Fermilab and a detector in the Soudan mine 735 km away. The neutrino beam is produced in the NuMI beamline with a 120 GeV proton beam from the Main Injector. The MINOS detectors are both iron-scintillator tracking calorimeters with toroidal magnetic fields. The far detector was 5.4 kt, while the near detector had a total mass of 0.98 kt and was located 1 km downstream of the production target. The energy spectrum of the NuMI beamline can be varied by changing the relative position of the target and horns. Most of MINOS data were taken with the “low energy” configuration with a peak energy of around 3 GeV. Since 2013, NuMI was operated with a “medium energy” configuration with the peak neutrino energy of around 7 GeV. The experiment for this period was called MINOS+. MINOS and MINOS+ combined accelerator and atmospheric neutrino data in both disappearance and appearance modes to measure oscillation parameters [115–117].

In Europe, the CNGS neutrino beamline provided a beam with mean energy of 17 GeV from CERN to LNGS for long-baseline experiments with about 730 km of baseline. The beam energy was chosen so that CC interaction of ν_τ can occur for direct confirmation of ν_τ appearance. There was no near detector in CNGS because it was not necessary for the ν_τ appearance search. The OPERA experiment used a detector consisting of an emulsion/lead target with about 1.25 kt total mass, complemented by electronic detectors. The excellent spatial resolution of the emulsion enabled the event-by-event identification of τ leptons. OPERA observed ten ν_τ CC candidate events with 2.0 ± 0.4 expected background [118] and confirmed $\nu_\mu \rightarrow \nu_\tau$ oscillation in appearance mode with a statistical significance of 6.1σ . Another neutrino experiment, ICARUS [119], which used 600 t liquid argon time projection chambers (TPCs), was operated in Gran Sasso from 2010 to 2012.

The first generation of long-baseline experiments confirmed the existence of neutrino oscillation. The major initial goal of second-generation experiments was the observation of $\nu_\mu \rightarrow \nu_e$ oscillation. Using this appearance mode, and by comparison of neutrino and antineutrino oscillation probabilities, search for CP violation in the neutrino mixing and measurement of the mass ordering and the octant of θ_{23} become possible.

The T2K experiment started in 2010 using a newly constructed high-intensity proton synchrotron J-PARC and the Super-Kamiokande detector. It is the first long-baseline experiment to employ the off-axis neutrino beam. The off-axis angle of 2.5° was chosen to set the peak of the neutrino energy spectrum at 0.6 GeV, matching the first maximum of oscillation probability at the 295 km baseline for $\Delta m^2 \sim 2.5 \times 10^{-3} \text{ eV}^2$. T2K employs a set of near detectors at about 280 m from the production target. In 2011, T2K reported the first indication of $\nu_\mu \rightarrow \nu_e$ oscillation with a statistical significance of 2.5σ [120]. In the framework of 3ν mixing, it corresponds to detecting non-zero amplitude generated by the mixing angle θ_{13} (see Eq.14.33). Later $\nu_\mu \rightarrow \nu_e$ oscillation was established by T2K with more than 7σ in 2014 [121]. Figure 14.5 shows the observed kinematic distributions from T2K, for neutrino and antineutrino beam mode and also for muon and electron candidates. By a combined analysis of the neutrino and antineutrino data, T2K reported a hint of CP violation at the 2σ level [122, 123].

The NOvA experiment uses the upgraded NuMI beamline with an off-axis configuration. The 14 kt NOvA far detector is located near Ash River, Minnesota, 810 km away from the source. At 14.6 mrad off-axis from the central axis of the NuMI beam, the neutrino energy spectrum at the far detector has a peak of around 2 GeV. The near detector, located around 1 km from the source, has a functionally identical design to the far detector with a total mass of 290 t. Both detectors are tracking calorimeters consisting of planes of polyvinyl chloride cells alternating in vertical and horizontal orientation filled with liquid scintillator. The physics run of NOvA was started in 2014. After confirmation of ν_e appearance from ν_μ beam [124, 125], NOvA started data taking with

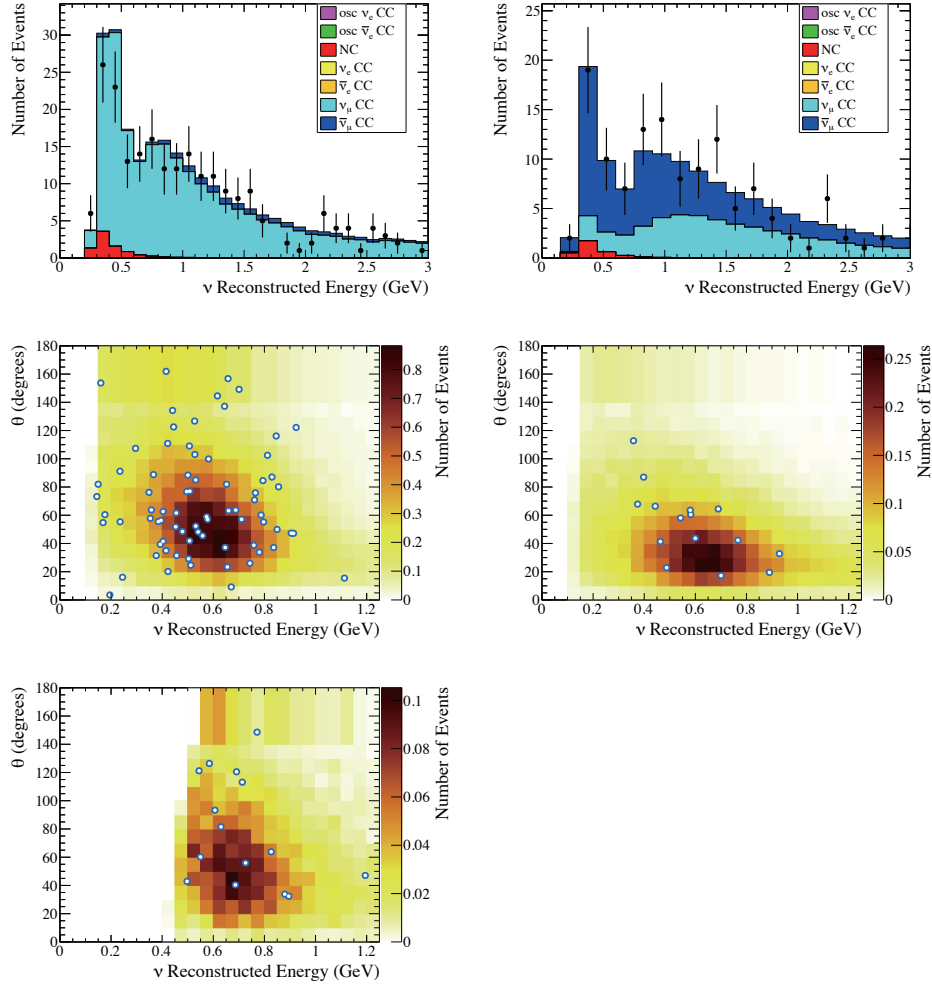


Figure 14.5: Observed kinematic distributions from T2K compared to the expectations assuming neutrino oscillations. Left and right panels correspond to data from neutrino and antineutrino beam mode, respectively. Top: Reconstructed energy distribution of single ring μ -like events. The error bars indicate the statistical uncertainty. Middle: Reconstructed energy vs. angle from beam direction of single ring e -like events with no associated decay electron. Bottom: Reconstructed energy vs. angle from beam direction of single ring e -like events with one associated decay electron for neutrino beam mode data.

antineutrino beam in 2016. Using the antineutrino beam data, NOvA has reported the observation of $\bar{\nu}_e$ appearance from $\bar{\nu}_\mu$ beam with 4.4σ significance [126]. Figure 14.6 shows the reconstructed neutrino energy distributions from NOvA. Some values of the CP -violating phase δ_{CP} (see Eq.14.33) have been excluded for the inverted mass ordering ($m_3 < m_2 < m_1$, see Sec.14.7 for definitions), while no significant limit has been set for the case of normal mass ordering ($m_1 < m_2 < m_3$, see Sec.14.7 for definitions).

Two large-scale long-baseline experiments are under preparation. DUNE [127] will be a 1,300 km long-baseline experiment based in the US. The DUNE far detector will consist of four modules of at least 10 kt fiducial mass liquid argon time projection chambers, located 1.5 km underground at

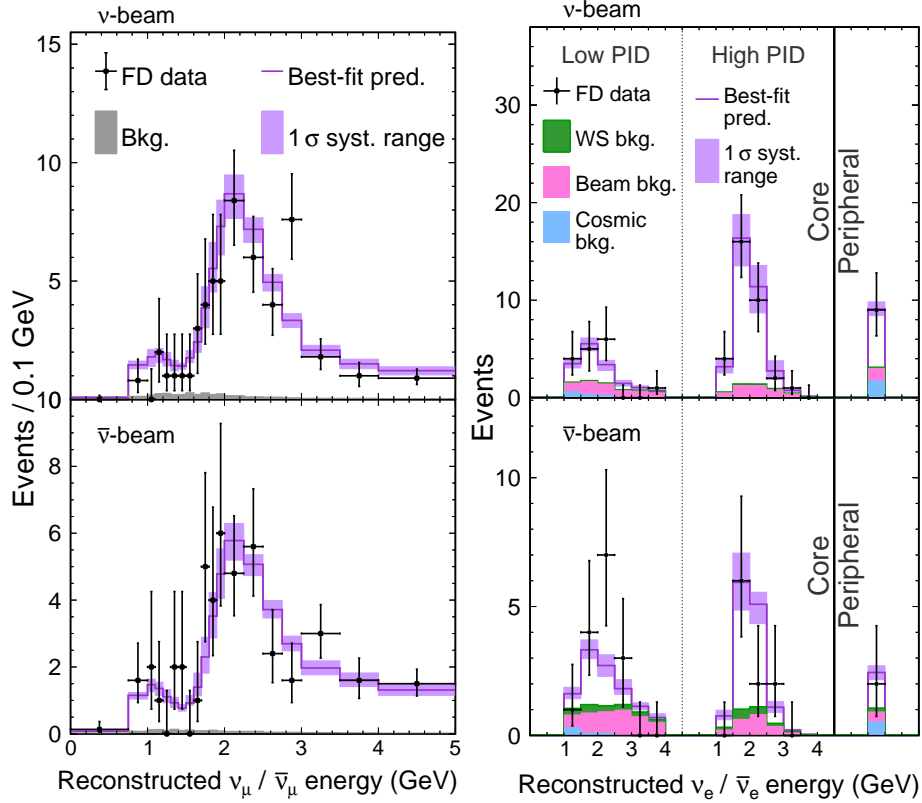


Figure 14.6: Reconstructed neutrino energy distributions from the NOvA far detector [126]. Top plots are for neutrino beam mode, and bottom plots are for antineutrino beam mode. Left: muon-type candidates. Right: electron-type candidates, split into a low and high purity sample as well as the event counts in the peripheral sample which occurred near the edge of the detector.

the Sanford Underground Research Facility in South Dakota. The beamline for DUNE, 1.2 MW at start and upgradable to 2.4 MW, as well as the facility for near detectors will be newly constructed at Fermilab. The Hyper-Kamiokande detector [128] in Japan will be the successor of the Super-Kamiokande detector. It will be a water Cherenkov detector with 260 kt total water mass. With upgrades to the existing accelerator and beamline, J-PARC will provide a 1.3 MW neutrino beam to Hyper-Kamiokande with a baseline of 295 km. Both DUNE and Hyper-Kamiokande will have a rich physics program besides the long-baseline experiment, such as searches for nucleon decays and study of supernova neutrinos.

14.6.3.4 Short-baseline experiments

The LSND experiment searched for neutrino oscillation using neutrinos from stopped pions at Los Alamos. A 800 MeV linac was used to produce pions that stopped in the target. Most of π^- s are absorbed by the nuclei inside the target, while π^+ s and their daughter μ^+ s decay and produce neutrinos. Therefore, the produced neutrinos are mostly ν_μ , $\bar{\nu}_\mu$, and ν_e with minimal contamination of $\bar{\nu}_e$. The detector was a tank filled with 167 t of diluted liquid scintillator, located about 30 m from the neutrino source. LSND searched for $\bar{\nu}_\mu \rightarrow \bar{\nu}_e$ appearance using the inverse beta decay process, $\bar{\nu}_e + p \rightarrow e^+ + n$, and found an excess of $87.9 \pm 22.4 \pm 6.0$ events over the expected background [129].

The KARMEN experiment was performed at the neutron spallation facility ISIS of the Ruther-

ford Appleton Laboratory. The KARMEN 2 detector was a segmented liquid scintillation calorimeter with a total volume of 65 m³ located at a mean distance of 17.7 m from the ISIS target. KARMEN found a number of events consistent with the total background expectation, showing no signal for $\bar{\nu}_\mu \rightarrow \bar{\nu}_e$ oscillations [130]. The resulting limits exclude large regions of the parameter area favored by LSND.

The MiniBooNE experiment at Fermilab used a conventional neutrino beam to search for ν_e and $\bar{\nu}_e$ appearance in the same parameter region as LSND. The booster neutrino beamline (BNB) with a single magnetic horn uses an 8 GeV proton beam from the Fermilab booster to produce a neutrino (antineutrino) beam with an energy spectrum peak of 600 (400) MeV. The MiniBooNE detector consists of a 12.2 m diameter sphere filled with 818 t of mineral and oil located 541 m from the target. MiniBooNE reported ν_e and $\bar{\nu}_e$ event excess in both neutrino and antineutrino running modes. In total, $638.0 \pm 52.1 \pm 122.2$ excess events are observed over the expected backgrounds, corresponding to 4.8σ significance [131].

Both LSND and MiniBooNE are single detector experiments. The reported excess will be further investigated with the multi-detector short-baseline neutrino (SBN) program at Fermilab BNB [132]. The SBN program comprises three liquid argon time projection chambers at different baselines in the same neutrino beamline. The 112 t Short-Baseline Near Detector will be located at 110 m from the target. The 85 t MicroBooNE detector has been operated at 470 m from the target. The ICARUS detector was transported from Europe after refurbishment at CERN and is located at a baseline of 600 m.

JSNS² experiment at J-PARC has started the search for neutrino oscillations with $\Delta m^2 \sim 1 \text{ eV}^2$ [133]. 1MW proton beam from the 3 GeV Rapid Cycling Synchrotron of J-PARC produces neutrinos from muon decay at rest. With a detector filled with a gadolinium-loaded liquid scintillator of 17 t fiducial mass at 24 m from the target, JSNS² is aiming to provide a direct test of the LSND anomaly. The second phase with additional second detector at 48 m is under preparation.

14.6.4 Reactor Antineutrinos

14.6.4.1 Reactor antineutrino flux

Nuclear reactors are very intense sources of $\bar{\nu}_e$'s in the MeV energy region, which are generated in nuclear fission of heavy isotopes (mainly ²³⁵U, ²³⁸U, ²³⁹Pu, and ²⁴¹Pu). The $\bar{\nu}_e$ flux from a reactor can be estimated based on the thermal power output and fuel composition as a function of time. On average, about six $\bar{\nu}_e$'s are emitted, and about 200 MeV of energy is released per fission. Therefore, a 1 GW_{th} (thermal power) reactor produces about 2×10^{20} $\bar{\nu}_e$'s per second.

The detailed estimate of $\bar{\nu}_e$ flux and energy spectrum can be obtained by either summing up the spectra of beta decays involved using available nuclear data information of each fission fragment and its decays, or by using measurements of cumulative electron spectra associated with the beta decays of fission fragments. Because the fission of four main fuel isotopes involves thousands of beta-decay branches, a complete *ab initio* calculation is challenging. The cumulative electron spectra for ²³⁵U, ²³⁹Pu, and ²⁴¹Pu were measured at the Institut Laue-Langevin (ILL) reactor in Grenoble, France in the 1980s [134–136]. For the prediction of $\bar{\nu}_e$ flux from ²³⁸U, a summation calculation in [137] was often used together with the ILL results.

A recent calculation of the reactor $\bar{\nu}_e$ flux [138] uses an improved *ab initio* approach for ²³⁸U and combined information from nuclear databases and electron spectra measured at ILL for ²³⁵U, ²³⁹Pu, and ²⁴¹Pu. Another calculation [139] is provided for ²³⁵U, ²³⁹Pu, and ²⁴¹Pu based on the ILL measurement of electron spectra, taking into account higher-order corrections and minimizing the use of nuclear databases. Both calculations predict a few percent higher normalization for the energy-averaged antineutrino fluxes of ²³⁵U, ²³⁹Pu, and ²⁴¹Pu compared to the original analyses of ILL data. However, the reactor antineutrino flux measurement at Daya Bay [140] is consistent

with the old flux predictions and the flux measurement results. Also, an excess of $\bar{\nu}_e$ flux around 5 MeV, compared to the prediction, has been observed by recent reactor experiments [141–144].

Table 14.4: List of reactor antineutrino oscillation experiments

Name	Reactor power (GW _{th})	Baseline (km)	Detector mass (t)	Year
KamLAND	various	180 (ave.)	1,000	2001–
Double Chooz	4.25×2	1.05	8.3	2011–2018
Daya Bay	2.9×6	1.65	20×4	2011–2020
RENO	2.8×6	1.38	16	2011–
JUNO	26.6 (total)	53	20,000	

14.6.4.2 Reactor antineutrino oscillation experiments

Charged current interaction cannot happen if a reactor $\bar{\nu}_e$ changes its flavour to $\bar{\nu}_\mu$ or $\bar{\nu}_\tau$, because its energy is not sufficient to produce heavier charged leptons. Thus, $\bar{\nu}_e$ disappearance is the only channel to study neutrino flavour change with reactor experiments. The inverse beta decay $\bar{\nu}_e + p \rightarrow e^+ + n$ provides a way to detect $\bar{\nu}_e$ in the relevant energy region. The energy of prompt signal from e^+ , E_p , is related to the energy of $\bar{\nu}_e$, $E_{\bar{\nu}} \sim E_p + 0.8$ MeV. The delayed coincidence with the signal from γ ray emitted by neutron capture on nucleus after thermalization very efficiently suppresses the backgrounds. A liquid scintillator is often used to realize large detectors containing hydrogen as the target of inverse beta decay. In order to increase the neutron detection efficiency, a liquid scintillator is sometimes loaded with gadolinium because of a large neutron capture cross-section and higher energy of emitted γ rays, the total energy of about 8 MeV, by gadolinium, in contrast to 2.2 MeV for the capture by hydrogen.

Early reactor experiments that searched for neutrino oscillations at short or intermediate baselines reported negative results. The CHOOZ [145] and Palo Verde [146] experiments in the 1990’s searched for neutrino oscillations in the $\Delta m^2 \sim 10^{-2}$ – 10^{-3} eV² range and set a limit on the corresponding mixing angle $\sin^2 2\theta < 0.1$ at 90% CL.

Table 14.4 shows a list of reactor antineutrino experiments measuring neutrino oscillation. As was also shown in Table 14.1, experiments are designed with different baselines because of the different scale of mass splittings found by solar and atmospheric neutrino experiments. Experiments with O(100) km baseline are sensitive to Δm^2 of 10^{-4} – 10^{-5} eV², while ~ 1 km of baseline results in a sensitivity in the range of 10^{-2} – 10^{-3} eV².

The KamLAND detector consists of 1,000 t of ultra-pure liquid scintillator contained in a 13-m diameter spherical balloon [147]. The detector is located in the original Kamiokande cavern, where the $\bar{\nu}_e$ flux was dominated by a few reactors at an average distance of ~ 180 km until 2011. KamLAND reported the first results in 2002 showing that the ratio of the observed number of $\bar{\nu}_e$ events and expectation without disappearance is $0.611 \pm 0.085 \pm 0.041$, evidence for reactor $\bar{\nu}_e$ disappearance at the 99.95% confidence level [147]. It confirmed a large value of the mixing angle corresponding to the LMA solution, which was reported by solar neutrino experiments. KamLAND also showed the evidence of $\bar{\nu}_e$ spectrum distortion consistent with the expectation from neutrino oscillations [148]. Figure 14.7 shows the ratio of observed $\bar{\nu}_e$ spectrum to the expectation for no-oscillation as a function of L_0/E ($L_0 = 180$ km) for the KamLAND data. A clear oscillatory signature can be seen.

Following the establishment of neutrino oscillations with atmospheric, solar, accelerator, and reactor experiments, the measurement of the remaining mixing angle θ_{13} was recognized as the next major milestone. A reactor neutrino experiment with a baseline of ~ 1 km can make an almost

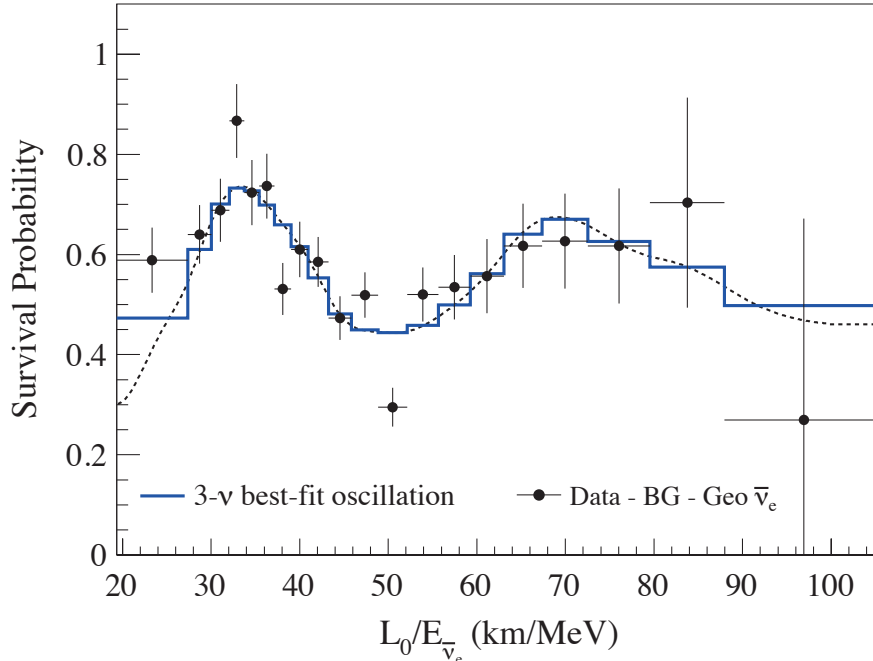


Figure 14.7: Ratio of the observed $\bar{\nu}_e$ spectrum to the expectation for no-oscillation versus L_0/E for the KamLAND data. $L_0 = 180$ km is the flux-weighted average reactor baseline. The 3ν histogram is the best-fit survival probability curve from the three-flavour unbinned maximum-likelihood analysis using only the KamLAND data. This figure is taken from [149].

pure measurement of $\sin^2 2\theta_{13}$ from the disappearance of $\bar{\nu}_e$. To be sensitive to a small value below the limit set by CHOOZ and Palo Verde, experiments with two detectors were proposed. Among several proposals, three experiments have been realized: Double Chooz in France, Daya Bay in China, and RENO in Korea.

These three experiments employ a similar detector design optimized for the precise measurement of a reactor antineutrino. An antineutrino detector consists of a cylindrical stainless steel vessel that houses two nested acrylic cylindrical vessels. The innermost vessel is filled with gadolinium-doped liquid scintillator as the primary antineutrino target. It is surrounded by a liquid scintillator layer to contain γ rays from the target volume. A buffer layer of mineral oil is placed outside to shield inner volumes from radioactivity of PMTs and surrounding rock. The light from liquid scintillator is detected by an array of PMTs mounted on the stainless steel vessel. Optically separated by the stainless steel vessel, the outside region is instrumented as a veto detector with either liquid scintillator (Double Chooz) or water Cherenkov (Daya Bay and RENO) detector.

The Double Chooz detector has a gadolinium-doped liquid scintillator with a mass of 8.3 t. The far detector at a baseline of ~ 1050 m from the two 4.25 GW_{th} reactors started physics data taking in 2011. The near detector, located at ~ 400 m from the reactors, was completed in the end of 2014. Double Chooz finished data taking in early 2018. Daya Bay has two near (flux-weighted baseline 470 m and 576 m), and one far (1648 m) underground experimental halls near six reactors with 2.9 GW_{th} each. Daya Bay has eight antineutrino detectors in total; two detectors in each of the near detector halls, and four detectors in the far detector hall. Each detector contains 20 t of gadolinium-loaded liquid scintillator. RENO has two identical detectors located at 294 m and 1383 m from the center of an array of six 2.8 GW_{th} reactors. The mass of the gadolinium-loaded

liquid scintillator is 16 t per detector. RENO started data taking with both near and far detectors from August 2011.

All three reactor neutrino experiments published their first results in 2012. First, Double Chooz reported an indication of reactor electron antineutrino disappearance with the ratio of observed to expected events of $R = 0.944 \pm 0.016 \pm 0.04$, ruling out the no-oscillation hypothesis at the 94.6% CL [150]. Daya Bay observed $R = 0.940 \pm 0.011 \pm 0.004$, corresponding to 5.2σ significance of non-zero value of θ_{13} [151]. RENO also reported $R = 0.920 \pm 0.009 \pm 0.014$, indicating a non-zero value of θ_{13} with a significance of 4.9σ [152]. These results established a non-zero value of θ_{13} .

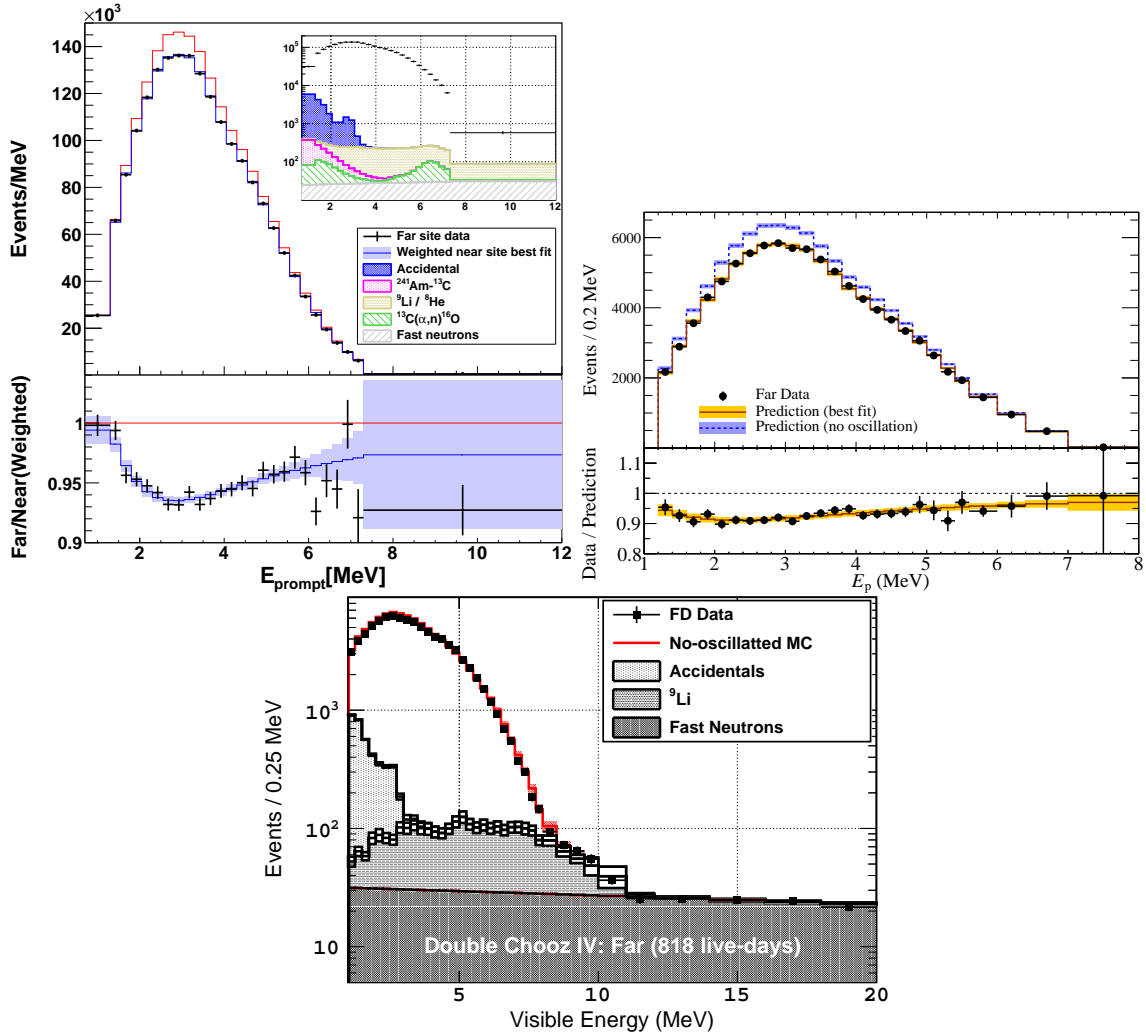


Figure 14.8: Energy spectra for prompt events at the far detectors for Daya Bay [141], RENO [142], and Double Chooz [143].

Both Daya Bay [141] and RENO [142] report results constraining mass-squared difference as well as the mixing angle by using both relative $\bar{\nu}_e$ rate and energy spectra information. Double Chooz has reported the analysis based on both far and near detectors [143] for the mixing angle, using neutron capture on any elements (primarily gadolinium and hydrogen) to increase the effective target mass. Figure 14.8 shows the energy spectra of the prompt signals observed in the far detector of three experiments.

Table 14.5: List of reactor antineutrino experiments for $O(eV^2)$ oscillations

Name	Reactor power (MW _{th})	Baseline (m)	Detector mass (t)	Detector technology	σ_E/E @1 MeV(%)	S/B
NEOS	2,800	24	1	Gd-LS	5	22
DANSS	3,100	10–13	0.9	Gd-PS	34	~30
STEREO	57	9–11	1.7	Gd-LS	10	0.9
PROSPECT	85	7–9	4	⁶ Li-LS	4.5	1.3
NEUTRINO-4	100	6–12	1.5	Gd-LS	16	0.5
SoLid	80	6–9	1.6	⁶ Li-PS	14	

In all three experiments, as well as in the NEOS experiment [144], an excess of $\bar{\nu}_e$ events over the expected energy spectrum has been observed around 5 MeV, as mentioned earlier. This excess is observed in both near and far detectors and scales with the reactor power. Thanks to the cancellation between the near and far detectors, the neutrino oscillation measurements are not affected in a multi-detector setup.

With a baseline of ~ 50 km and an excellent energy measurement, reactor antineutrino experiments have significant sensitivity to the mass ordering. The JUNO detector, which is under construction, will consist of a 20 kt liquid scintillator and be located at 53 km from two nuclear power plants in China [153]. The JUNO experiment aims to determine the mass ordering with this technique as its primary goal. It can also provide precision measurements of neutrino mixing parameters as well as a broad non-oscillation science program.

14.6.4.3 New reactor experiments sensitive to $O(1)$ eV^2 oscillations

Possible hints of neutrino oscillation at a scale of $\Delta m^2 \sim 1$ eV^2 (see Sec.14.8) have motivated reactor experiments at a distance of ~ 10 m from the core. Recent experiments searching for ~ 1 eV^2 oscillation at reactors are summarized in Table 14.5.

As the antineutrino source, some use commercial reactors, which can provide a large flux leading to high statistical precision. On the other hand, though the flux is orders of magnitude smaller, a research reactor could have favorable conditions such as relatively easier access to a short baseline, simpler fuel composition, and compact core size.

The detectors are based on organic scintillators, either liquid scintillator (LS) or solid plastic scintillator (PS), which contain hydrogen as the target for inverse beta decay ($\bar{\nu}_e + p \rightarrow e^+ + n$). To identify the signal, neutron capture on either gadolinium (Gd) or ⁶Li is detected with delayed coincidence. When a neutron is captured by Gd, γ rays with a total energy of 8 MeV are emitted. After neutron capture, ⁶Li decays into triton and α . The effect of neutrino oscillation appears as a distortion of energy spectrum. To be independent from the reactor neutrino spectrum uncertainties, some experiments compare the spectra at different baselines by using a segmented detector or moving the detector.

NEOS [144] uses about 1 t of gadolinium-loaded liquid scintillator in an unsegmented detector. It is located at 23.7 m from the center of a commercial reactor and covered by an overburden of about 20 meters of water equivalent.

DANSS [154] is another experiment using a commercial reactor. The detector is highly segmented, consisting of 2,500 plastic scintillator strips, each with the size of $1 \times 4 \times 100$ cm³ and coated with a thin gadolinium-loaded reflective layer. The detector is placed on a movable platform below the reactor core, which varies the distance to the core from 10.7 to 12.7 m.

The STEREO detector [155] has six identical target cells of 37 cm length, $\sim 2\text{m}^3$ of volume in total, filled with gadolinium-loaded liquid scintillator. They are placed from 9.4 to 11.1 m from the compact (80 cm high, 40 cm diameter) core of the ILL research reactor.

The PROSPECT detector [156] consists of a segmented 4 t ^6Li -doped liquid scintillator detector. It covers a baseline range of 7–9 m from the highly ^{235}U enriched reactor core of the High Flux Isotope Reactor (HFIR) at Oak Ridge National Laboratory. Thin reflecting panels divide the LS volume into an 11×14 two-dimensional array of 154 optically isolated rectangular segments ($14.5 \times 14.5 \times 117.6 \text{ cm}^3$).

NEUTRINO-4 [157,158] uses a gadolinium-loaded liquid scintillator detector segmented in 10×5 sections with a total volume of 1.8 m^3 . The detector is installed on a movable platform and moved to various positions with baselines of 6–12 m from the SM-3 reactor core in Russia.

The SoLid detector [159] is a finely segmented detector made of $5 \times 5 \times 5 \text{ cm}^3$ plastic scintillator cubes and $^6\text{LiF:ZnS}$ sheets. Using the difference of time constant of scintillation between ZnS and the plastic scintillator a n - γ separation capability is achieved. A detector with 1.6 t of active volume is installed at a distance of 6–9 m from the research reactor core in the BR2 reactor, Belgium.

14.7 Combined Analysis of Experimental Results: The 3ν Paradigm

From the experimental situation described in Sec.14.6 we conclude that

- Atmospheric ν_μ and $\bar{\nu}_\mu$ disappear most likely converting to ν_τ and $\bar{\nu}_\tau$. The results show an energy and distance dependence perfectly described by mass-induced oscillations.
- Accelerator ν_μ and $\bar{\nu}_\mu$ disappear over distances of ~ 200 to 800 km. The energy spectrum of the results show a clear oscillatory behavior also in accordance with mass-induced oscillations with a wavelength in agreement with the effect observed in atmospheric neutrinos.
- Accelerator ν_μ and $\bar{\nu}_\mu$ appear as ν_e and $\bar{\nu}_e$ at distances ~ 200 to 800 km.
- Solar ν_e convert to ν_μ and/or ν_τ . The observed energy dependence of the effect is well described by massive neutrino conversion in the Sun matter according to the MSW effect
- Reactor $\bar{\nu}_e$ disappear over distances of ~ 200 km and ~ 1.5 km with different probabilities. The observed energy spectra show two different mass-induced oscillation wavelengths: at short distances in agreement with the one observed in accelerator ν_μ disappearance, and a long-distance compatible with the required parameters for MSW conversion in the Sun.

The minimum scenario to describe these results requires the mixing between the three flavour neutrinos of the standard model in three distinct mass eigenstates. In this case U in Eq. (14.32) is a 3×3 matrix analogous to the CKM matrix for the quarks [21], but due to the possible Majorana nature of the neutrinos it can depend on six independent parameters: three mixing angles and three phases. There are several possible conventions for the ranges of the angles and ordering of the states. The community finally agreed to a parametrization of the leptonic mixing matrix as in Eq. (14.33). The angles θ_{ij} can be taken without loss of generality to lie in the first quadrant, $\theta_{ij} \in [0, \pi/2]$, and the phase $\delta_{\text{CP}} \in [0, 2\pi]$. Values of δ_{CP} different from 0 and π imply CP violation in neutrino oscillations in vacuum [160–162]. The Majorana phases η_1 and η_2 play no role in neutrino oscillations [161,163]. Hence for the study of neutrino oscillations in the 3ν mixing scenario one can use the parametrization in Eq. (14.34) irrespective of whether neutrinos are Dirac or Majorana particles. Indeed, Majorana phases are very hard to measure since they are only physical if neutrino mass is non-zero, and therefore, the amplitude of any process involving them is suppressed by a factor m_ν/E to some power where E is the energy involved in the process, which is typically much larger than the neutrino mass. The most sensitive experimental probe of Majorana phases is the rate of neutrinoless $\beta\beta$ decay discussed in Secs. 14.9.3 and 14.9.2.

In this convention there are two non-equivalent orderings for the spectrum of neutrino masses:

- Spectrum with Normal Ordering (NO) with $m_1 < m_2 < m_3$
- Spectrum Inverted ordering (IO) with $m_3 < m_1 < m_2$.

Furthermore, the data show a hierarchy between the mass splittings, $\Delta m_{21}^2 \ll |\Delta m_{31}^2| \simeq |\Delta m_{32}^2|$ with $\Delta m_{ij}^2 \equiv m_i^2 - m_j^2$.

In this section, we follow the convention used in the listing section of the PDG and discuss the results for both, NO and IO, using Δm_{21}^2 , which is always the smallest mass splitting, and Δm_{32}^2 , which up to a sign, is the largest mass splitting for IO, while for NO the largest mass splitting is $\Delta m_{31}^2 = \Delta m_{32}^2 + \Delta m_{21}^2$.

With what we know of the mass differences (see table 14.7) and the neutrino mass scale (see Sec. 14.9), depending on the value of the lightest neutrino mass, the neutrino mass spectrum can be further classified in:

- Normal Hierarchical Spectrum (NH): $m_1 \ll m_2 < m_3$,
 $\Rightarrow m_2 \simeq \sqrt{\Delta m_{21}^2} \sim 8.6 \times 10^{-3} \text{eV}, m_3 \simeq \sqrt{\Delta m_{32}^2 + \Delta m_{21}^2} \sim 0.05 \text{eV},$
- Inverted Hierarchical Spectrum (IH): $m_3 \ll m_1 < m_2$,
 $\Rightarrow m_1 \simeq \sqrt{|\Delta m_{32}^2 + \Delta m_{21}^2|} \sim 0.0492 \text{eV}, m_2 \simeq \sqrt{|\Delta m_{32}^2|} \sim 0.05 \text{eV},$
- Quasidegenerate Spectrum (QD): $m_1 \simeq m_2 \simeq m_3 \gg \sqrt{|\Delta m_{32}^2|}$.

Sometimes in the literature the determination of the neutrino mass spectrum is referred to as determination of the neutrino hierarchy. However, as described above, with what we know so far of the neutrino mass scale, the neutrino spectrum may or may not be hierarchical. Therefore determination of neutrino mass ordering is a more precise expression, and it is the one used in this review.

In total, the 3ν oscillation analysis of the existing data involves six parameters: 2 mass differences (one of which can be positive or negative), 3 mixing angles, and the CP phase. The different experiments described in Sec.14.6 provide information on different subsets of these parameters. The precise statistical analysis of the data requires the numerical evaluation of the corresponding oscillation probabilities by solving the evolution equation of the neutrino ensemble from their source to the experiment. Nevertheless, the dominant effects in the different experiments can be qualitatively understood in terms of approximate expressions for the oscillation probabilities which, for convenience, we briefly summarize here.

14.7.1 3ν Oscillation Probabilities

The relevant survival probabilities for solar and KamLAND experiments in the framework of three neutrino oscillations can be written as:

$$P_{ee}^{3\nu} = \sin^4 \theta_{13} + \cos^4 \theta_{13} P_{ee}^{2\nu}(\Delta m_{21}^2, \theta_{12}), \quad (14.72)$$

where we have used the fact that $L_{0,32}^{\text{osc}} = 4\pi E_\nu / \Delta m_{32}^2$ is much shorter than the distance traveled by both solar and KamLAND neutrinos, so that the oscillations related to $L_{0,32}^{\text{osc}}$ are averaged. In the presence of matter effects $P_{ee}^{2\nu}(\Delta m_{21}^2, \theta_{12})$ should be calculated, taking into account the evolution in an effective matter density $n_e^{\text{eff}} = n_e \cos^2 \theta_{13}$. For $10^{-5} \lesssim \Delta m^2 / \text{eV}^2 \lesssim 10^{-4}$, $P_{ee}^{2\nu}(\Delta m_{21}^2, \theta_{12})$

presents the following asymptotic behaviors [164]:

$$P_{ee}^{2\nu,\text{sun}} \simeq 1 - \frac{1}{2} \sin^2(2\theta_{12}) \quad \text{for } E_\nu \lesssim \text{few} \times 100 \text{ keV}, \quad (14.73)$$

$$P_{ee}^{2\nu,\text{sun}} \simeq \sin^2(\theta_{12}) \quad \text{for } E_\nu \gtrsim \text{few} \times 1 \text{ MeV}, \quad (14.74)$$

$$P_{ee}^{2\nu,\text{kam}} = 1 - \sin^2(2\theta_{12}) \sin^2 \frac{\Delta m_{21}^2 L}{4E_\nu}. \quad (14.75)$$

At present most of the precision of the solar analysis is provided by SNO and SK, for which the relevant MSW survival probability provides a direct measurement of $\sin^2 \theta_{12}$, as seen in Eq. (14.74). In the MSW regime, the determination of Δm_{21}^2 in solar experiments comes dominantly from the ratio between the solar potential and the Δm_{21}^2 term required to simultaneously describe the CC/NC data at SNO and the undistorted spectra of ^8B neutrinos as measured in both SK and SNO. Conversely, KamLAND $\bar{\nu}_e$ survival probability proceeds dominantly as vacuum oscillations and provides a most precise determination of Δm_{21}^2 via the strong effect of the oscillating phase in the distortion of the reactor energy spectrum. On the contrary, it yields a weaker constraint on θ_{12} as the vacuum oscillation probability depends on the double-valued and “flatter” function $\sin^2(2\theta_{12})$.

In what respects the interpretation of ν_μ disappearance data, at LBL experiments, the ν_μ survival probability can be expanded in the small parameters $\sin \theta_{13}$ and $\alpha \equiv \Delta m_{21}^2 / \Delta m_{31}^2$ to good accuracy as [165, 166]

$$P_{\nu_\mu \rightarrow \nu_\mu} \approx 1 - \sin^2 2\theta_{\mu\mu} \sin^2 \frac{\Delta m_{\mu\mu}^2 L}{4E_\nu} \approx 1 - \cos^2 \theta_{13} \sin^2(2\theta_{23}) \sin^2 \frac{\Delta m_{32}^2 L}{4E_\nu} + \mathcal{O}(\alpha, s_{13}^2), \quad (14.76)$$

with

$$\begin{aligned} \sin^2 \theta_{\mu\mu} &= \cos^2 \theta_{13} \sin^2 \theta_{23}, \\ \Delta m_{\mu\mu}^2 &= \sin^2 \theta_{12} \Delta m_{31}^2 + \cos^2 \theta_{12} \Delta m_{32}^2 \\ &\quad + \cos \delta_{\text{CP}} \sin \theta_{13} \sin 2\theta_{12} \tan \theta_{23} \Delta m_{21}^2. \end{aligned}$$

At present ν_μ disappearance results at LBL provide the best determination of $|\Delta m_{32}^2|$ and θ_{23} , but as seen above, the probability is symmetric with respect to the octant of $\theta_{\mu\mu}$, which implies symmetry around $s_{23}^2 = 0.5/c_{13}^2$.

The relevant oscillation probability for ν_e appearance at LBL experiments can be expanded at the second order in the small parameters $\sin \theta_{13}$ and α , and assuming a constant matter density it takes the form [167–169]:

$$\begin{aligned} P_{\nu_\mu \rightarrow \nu_e, (\bar{\nu}_\mu \rightarrow \bar{\nu}_e)} \approx & 4 \sin^2 \theta_{13} \sin^2 \theta_{23} \frac{\sin^2 \Delta}{(1-A)^2} + \alpha^2 \sin^2 2\theta_{12} \cos^2 \theta_{23} \frac{\sin^2 A \Delta}{A^2} \\ & + 8 \alpha J_{\text{CP}}^{\text{max}} \cos(\Delta \pm \delta_{\text{CP}}) \frac{\sin \Delta A}{A} \frac{\sin \Delta(1-A)}{1-A}, \quad (14.77) \end{aligned}$$

with

$$J_{\text{CP}}^{\text{max}} = \cos \theta_{12} \sin \theta_{12} \cos \theta_{23} \sin \theta_{23} \cos^2 \theta_{13} \sin \theta_{13}, \quad (14.78)$$

and

$$\Delta \equiv \frac{\Delta m_{31}^2 L}{4E_\nu}, \quad A \equiv \frac{2E_\nu V}{\Delta m_{31}^2}, \quad (14.79)$$

where V is the effective matter potential in the Earth’s crust. Results on ν_e appearance at LBL provide us with the dominant information on leptonic CP violation. Furthermore, α , Δ , and A are

sensitive to the sign of Δm_{32}^2 (*i.e.*, the type of the neutrino mass ordering). The plus (minus) sign in Eq. (14.77) applies for neutrinos (antineutrinos), and for antineutrinos $V \rightarrow -V$, which implies $A \rightarrow -A$. Numerically one finds for a typical Earth crust matter density of 3 g/cm^3 that at T2K with $E \sim 0.7 \text{ GeV}$, matter effects cause $\sim \pm 10\%$ differences in the rates, whereas in NOvA with $E \sim 2 \text{ GeV}$, we can have $|A| \sim 0.2$. Also, $\alpha^2 \approx 10^{-3}$, which implies that the second term in the first line of Eq. (14.77) gives a very small contribution compared to the other terms. Also, the first term in Eq. (14.77) (which dominates for large θ_{13}) depends on $\sin^2 \theta_{23}$ and therefore is sensitive to the octant.

The ν_e survival probability relevant for reactor experiments with medium baseline (MBL), $L \sim 1 \text{ km}$, can be approximated as [166, 170]:

$$P_{\nu_e \rightarrow \nu_e} = 1 - \sin^2 2\theta_{13} \sin^2 \frac{\Delta m_{ee}^2 L}{4E_\nu} + \mathcal{O}(\alpha^2), \quad (14.80)$$

where

$$\Delta m_{ee}^2 = \cos^2 \theta_{12} \Delta m_{31}^2 + \sin^2 \theta_{12} \Delta m_{32}^2. \quad (14.81)$$

These MBL reactor experiments provide the most precise determination of θ_{13} . Furthermore there is an additional effect sensitive to the mass ordering when comparing the disappearance of ν_μ at LBL experiments – which is symmetric with respect to the sign of $\Delta m_{\mu\mu}^2$ given in Eq.(14.7.1) – with that of ν_e disappearance at MBL reactors which is symmetric with respect to the slightly different effective mass-squared difference Δm_{ee}^2 given in Eq. (14.81).

Table 14.6: Experiments contributing to the present determination of the oscillation parameters.

Experiment	Dominant	Important
Solar Experiments	θ_{12}	$\Delta m_{21}^2, \theta_{13}$
Reactor LBL (KamLAND)	Δm_{21}^2	θ_{12}, θ_{13}
Reactor MBL (Daya-Bay, Reno, D-Chooz)	$\theta_{13}, \Delta m_{31,32}^2 $	
Atmospheric Experiments (SK, IC-DC)		$\theta_{23}, \Delta m_{31,32}^2 , \theta_{13}, \delta_{\text{CP}}$
Accel LBL $\nu_\mu, \bar{\nu}_\mu$, Disapp (K2K, MINOS, T2K, NOvA)	$ \Delta m_{31,32}^2 , \theta_{23}$	
Accel LBL $\nu_e, \bar{\nu}_e$ App (MINOS, T2K, NOvA)	δ_{CP}	θ_{13}, θ_{23}

Finally, for atmospheric neutrinos, the fluxes contain $\nu_e, \nu_\mu, \bar{\nu}_e$, and $\bar{\nu}_\mu$, and for a good fraction of the events, neutrinos travel through the Earth's matter. In the context of 3ν mixing, the dominant oscillation channel of atmospheric neutrinos is $\nu_\mu \rightarrow \nu_\tau$ driven by $|\Delta m_{32}^2|$ with an amplitude controlled by θ_{23} with subleading oscillation modes, triggered by Δm_{21}^2 and/or θ_{13} , which depend on the octant of θ_{23} , on the mass ordering, and on δ_{CP} . In that respect, an interesting observable is the deviation of e -like events relative to the no-oscillation prediction N_e^0 , since in the two-flavour limit one expects $N_e = N_e^0$. Such deviation can be written in the following way (see, *e.g.*, [171]):

$$\begin{aligned} \frac{N_e}{N_e^0} - 1 &\approx (r \sin^2 \theta_{23} - 1) P_{2\nu}(\Delta m_{32}^2, \theta_{13}) + (r \cos^2 \theta_{23} - 1) P_{2\nu}(\Delta m_{21}^2, \theta_{12}) \\ &\quad - \sin \theta_{13} \sin 2\theta_{23} r \Re(A_{ee}^* A_{\mu e}). \end{aligned} \quad (14.82)$$

Here $r \equiv \Phi_\mu / \Phi_e$ is the flux ratio with $r \approx 2$ in the sub-GeV range and $r \approx 2.6 \rightarrow 4.5$ in the multi-GeV range. $P_{2\nu}(\Delta m^2, \theta)$ is an effective two-flavour oscillation probability, and $A_{ee}, A_{\mu e}$ are elements of a transition amplitude matrix. The three terms appearing in Eq. (14.82) have a well-defined physical interpretation. The first term is important in the multi-GeV range and is controlled by the

mixing angle θ_{13} in $P_{2\nu}(\Delta m_{32}^2, \theta_{13})$. This probability can be strongly affected by resonant matter effects [172–177]. Depending on the mass ordering, the resonance will occur either for neutrinos or antineutrinos. The second term is important for sub-GeV events, and it takes into account the effect of oscillations due to Δm_{21}^2 and θ_{12} [178–181]. Via the pre-factor containing the flux ratio r both, the first and second terms in Eq. (14.82) depend on the octant of θ_{23} , though in opposite directions: the multi-GeV (sub-GeV) excess is suppressed (enhanced) for $\theta_{23} < 45^\circ$. Finally, the last term in Eq. (14.82) is an interference term between θ_{13} and Δm_{21}^2 amplitudes and this term shows also dependence on the CP phase δ_{CP} [171, 181].

Subdominant three neutrino effects can also affect μ -like events. For example, for multi-GeV muon events one can write the excess in μ -like events as [182, 183]

$$\frac{N_\mu}{N_\mu^0} - 1 \approx \sin^2 \theta_{23} \left(\frac{1}{r} - \sin^2 \theta_{23} \right) P_{2\nu}(\Delta m_{32}^2, \theta_{13}) - \frac{1}{2} \sin^2 2\theta_{23} [1 - \Re(A_{33})]. \quad (14.83)$$

The first term is controlled by θ_{13} and is subject to resonant matter effects, similar to the first term in Eq. (14.82), though with a different dependence on θ_{23} and the flux ratio. In the second term, A_{33} is a probability amplitude satisfying $P_{2\nu}(\Delta m_{32}^2, \theta_{13}) = 1 - |A_{33}|^2$. In the limit $\theta_{13} = 0$ we have $\Re(A_{33}) = \cos(\Delta m_{32}^2 L/2E)$, such that the second term in Eq. (14.83) just describes two-flavour $\nu_\mu \rightarrow \nu_\mu$ vacuum oscillations.

14.7.2 3ν Oscillation Analysis

We summarize in Table 14.6 the different experiments which dominantly contribute to the present determination of the different parameters in the chosen convention.

The table illustrates that the determination of the leptonic parameters requires global analyses of the data from the different experiments. Over the years, these analyses have been in the hands of a few phenomenological groups. We show in Table 14.7 the results from the latest analyses in Refs. [184–187]. For the sake of comparison, all results are presented in the convention of the listing section as described above.

The table illustrates the dependence of the present determination of the parameters on variations of the statistical analysis performed by the different groups and on the data samples included. In that last respect, the main difference resides in the results from Super-Kamiokande atmospheric data [97] which, at present, can only be included in this analysis by directly adding the χ^2 tabulated χ^2 map provided by the experiment.

Altogether the different analyses find consistent results, in particular on the better-known parameters, θ_{12} , θ_{13} and Δm_{21}^2 and $|\Delta m_{32}^2|$. The issues which still require clarification are the mass ordering discrimination, the determination of θ_{23} and the leptonic CP phase δ_{CP} :

- In all analyses the best fit is for the normal mass ordering. Inverted ordering is disfavoured with a $\Delta\chi^2$, which ranges from slightly above 2σ – driven by the interplay of long-baseline accelerator and short-baseline reactor data – to 3σ when adding the atmospheric χ^2 table from Ref. [97].
- All analyses find some preference for the second octant of θ_{23} but with statistical significance still well below 3σ .
- The best fit for the complex phase in NO is at $\delta_{CP} \sim 120^\circ$, but CP conservation (for $\delta_{CP} \sim 180^\circ$) is still allowed at a confidence level (CL) of 1-2 σ . We notice that, at present, the significance of CP violation in the global analysis is reduced with respect to that reported by T2K [188] because NOvA data does not show a significant indication of CP violation.

Table 14.7: 3ν oscillation parameters obtained from different global analyses of neutrino data. In all cases, the numbers labeled as NO (IO) are obtained assuming NO (IO), *i.e.*, relative to the respective local minimum. SK-ATM makes reference to the tabulated χ^2 map from the Super-Kamiokande analysis of their data in Ref. [97].

	Ref. [185] w/o SK-ATM		Ref. [185] w SK-ATM		Ref. [186] w SK-ATM		Ref. [187] w SK-ATM	
NO	Best Fit Ordering		Best Fit Ordering		Best Fit Ordering		Best Fit Ordering	
Param	bfp $\pm 1\sigma$	3σ range	bfp $\pm 1\sigma$	3σ range	bfp $\pm 1\sigma$	3σ range	bfp $\pm 1\sigma$	3σ range
$\frac{\sin^2 \theta_{12}}{10^{-1}}$	$3.10^{+0.13}_{-0.12}$	2.75 \rightarrow 3.50	$3.10^{+0.13}_{-0.12}$	2.75 \rightarrow 3.50	$3.04^{+0.14}_{-0.13}$	2.65 \rightarrow 3.46	$3.20^{+0.20}_{-0.16}$	2.73 \rightarrow 3.79
$\theta_{12}/^\circ$	$33.82^{+0.78}_{-0.76}$	31.61 \rightarrow 36.27	$33.82^{+0.78}_{-0.76}$	31.61 \rightarrow 36.27	$33.46^{+0.87}_{-0.88}$	30.98 \rightarrow 36.03	$34.5^{+1.2}_{-1.0}$	31.5 \rightarrow 38.0
$\frac{\sin^2 \theta_{23}}{10^{-1}}$	$5.58^{+0.20}_{-0.33}$	4.27 \rightarrow 6.09	$5.63^{+0.18}_{-0.24}$	4.33 \rightarrow 6.09	$5.51^{+0.19}_{-0.80}$	4.30 \rightarrow 6.02	$5.47^{+0.20}_{-0.30}$	4.45 \rightarrow 5.99
$\theta_{23}/^\circ$	$48.3^{+1.2}_{-1.9}$	40.8 \rightarrow 51.3	$48.6^{+1.0}_{-1.4}$	41.1 \rightarrow 51.3	$47.9^{+1.1}_{-4.0}$	41.0 \rightarrow 50.9	$47.7^{+1.2}_{-1.7}$	41.8 \rightarrow 50.7
$\frac{\sin^2 \theta_{13}}{10^{-2}}$	$2.241^{+0.066}_{-0.065}$	2.046 \rightarrow 2.440	$2.237^{+0.066}_{-0.065}$	2.044 \rightarrow 2.435	$2.14^{+0.09}_{-0.07}$	1.90 \rightarrow 2.39	$2.160^{+0.083}_{-0.069}$	1.96 \rightarrow 2.41
$\theta_{13}/^\circ$	$8.61^{+0.13}_{-0.13}$	8.22 \rightarrow 8.99	$8.60^{+0.13}_{-0.13}$	8.22 \rightarrow 8.98	$8.41^{+0.18}_{-0.14}$	7.9 \rightarrow 8.9	$8.45^{+0.16}_{-0.14}$	8.0 \rightarrow 8.9
$\delta_{\text{CP}}/^\circ$	222^{+38}_{-28}	141 \rightarrow 370	221^{+39}_{-28}	144 \rightarrow 357	238^{+41}_{-33}	149 \rightarrow 358	218^{+38}_{-27}	157 \rightarrow 349
Δm_{21}^2	$7.39^{+0.21}_{-0.20}$	6.79 \rightarrow 8.01	$7.39^{+0.21}_{-0.20}$	6.79 \rightarrow 8.01	$7.34^{+0.17}_{-0.14}$	6.92 \rightarrow 7.91	$7.55^{+0.20}_{-0.16}$	7.05 \rightarrow 8.24
$\frac{10^{-5} \text{ eV}^2}{\Delta m_{32}^2}$	$2.449^{+0.032}_{-0.030}$	2.358 \rightarrow 2.544	$2.454^{+0.029}_{-0.031}$	2.362 \rightarrow 2.544	$2.419^{+0.035}_{-0.032}$	2.319 \rightarrow 2.521	2.424 ± 0.03	2.334 \rightarrow 2.524
$\frac{10^{-3} \text{ eV}^2}{\Delta m_{32}^2}$								
IO	$\Delta\chi^2 = 6.2$		$\Delta\chi^2 = 10.4$		$\Delta\chi^2 = 9.5$		$\Delta\chi^2 = 11.7$	
$\frac{\sin^2 \theta_{12}}{10^{-1}}$	$3.10^{+0.13}_{-0.12}$	2.75 \rightarrow 3.50	$3.10^{+0.13}_{-0.12}$	2.75 \rightarrow 3.50	$3.03^{+0.14}_{-0.13}$	2.64 \rightarrow 3.45	$3.20^{+0.20}_{-0.16}$	2.73 \rightarrow 3.79
$\theta_{12}/^\circ$	$33.82^{+0.78}_{-0.76}$	31.61 \rightarrow 36.27	$33.82^{+0.78}_{-0.75}$	31.62 \rightarrow 36.27	$33.40^{+0.87}_{-0.81}$	30.92 \rightarrow 35.97	$34.5^{+1.2}_{-1.0}$	31.5 \rightarrow 38.0
$\frac{\sin^2 \theta_{23}}{10^{-1}}$	$5.63^{+0.19}_{-0.26}$	4.30 \rightarrow 6.12	$5.65^{+0.17}_{-0.22}$	4.36 \rightarrow 6.10	$5.57^{+0.17}_{-0.24}$	4.44 \rightarrow 6.03	$5.51^{+0.18}_{-0.30}$	4.53 \rightarrow 5.98
$\theta_{23}/^\circ$	$48.6^{+1.1}_{-1.5}$	41.0 \rightarrow 51.5	$48.8^{+1.0}_{-1.2}$	41.4 \rightarrow 51.3	$48.2^{+1.0}_{-1.4}$	41.8 \rightarrow 50.9	$47.9^{+1.0}_{-1.7}$	42.3 \rightarrow 50.7
$\frac{\sin^2 \theta_{13}}{10^{-2}}$	$2.261^{+0.067}_{-0.064}$	2.066 \rightarrow 2.461	$2.259^{+0.065}_{-0.065}$	2.064 \rightarrow 2.457	$2.18^{+0.08}_{-0.07}$	1.95 \rightarrow 2.43	$2.220^{+0.074}_{-0.076}$	1.99 \rightarrow 2.44
$\theta_{13}/^\circ$	$8.65^{+0.13}_{-0.12}$	8.26 \rightarrow 9.02	$8.64^{+0.12}_{-0.13}$	8.26 \rightarrow 9.02	$8.49^{+0.15}_{-0.14}$	8.0 \rightarrow 9.0	$8.53^{+0.14}_{-0.15}$	8.1 \rightarrow 9.0
$\delta_{\text{CP}}/^\circ$	285^{+24}_{-26}	205 \rightarrow 354	282^{+23}_{-25}	205 \rightarrow 348	247^{+26}_{-27}	193 \rightarrow 346	281^{+23}_{-27}	202 \rightarrow 349
Δm_{21}^2	$7.39^{+0.21}_{-0.20}$	6.79 \rightarrow 8.01	$7.39^{+0.21}_{-0.20}$	6.79 \rightarrow 8.01	$7.34^{+0.17}_{-0.14}$	6.92 \rightarrow 7.91	$7.55^{+0.20}_{-0.16}$	7.05 \rightarrow 8.24
$\frac{10^{-5} \text{ eV}^2}{\Delta m_{32}^2}$	$-2.509^{+0.032}_{-0.032}$	-2.603 \rightarrow -2.416	$-2.510^{+0.030}_{-0.031}$	-2.601 \rightarrow -2.419	$-2.478^{+0.035}_{-0.033}$	-2.577 \rightarrow -2.375	$-2.50 \pm^{+0.04}_{-0.03}$	-2.59 \rightarrow -2.39
$\frac{10^{-3} \text{ eV}^2}{\Delta m_{32}^2}$								

14.7.3 Convention-independent Measures of Leptonic CP Violation in 3ν Mixing

In the framework of 3ν mixing leptonic CP violation can also be quantified in terms of the leptonic Jarlskog invariant [189], defined by:

$$\Im[U_{\alpha i} U_{\alpha j}^* U_{\beta i} U_{\beta j}] \equiv \sum_{\gamma=e,\mu,\tau} \sum_{k=1,2,3} J_{\text{CP}} \epsilon_{\alpha\beta\gamma} \epsilon_{ijk} \equiv J_{\text{CP}}^{\text{max}} \sin \delta_{\text{CP}}. \quad (14.84)$$

With the convention in Eq. (14.33) $J_{\text{CP}}^{\text{max}}$ is the combination of mixing angles in Eq. (14.78). For example, from the analysis in Ref. [184, 185]

$$J_{\text{CP}}^{\text{max}} = 0.03359 \pm 0.0006 (\pm 0.0019), \quad (14.85)$$

at 1σ (3σ) for both orderings, and the preference of the present data for non-zero δ_{CP} implies a non-zero best fit value $J_{\text{CP}}^{\text{best}} = -0.019$.

The status of the determination of leptonic CP violation can also be graphically displayed by projecting the results of the global analysis in terms of leptonic unitarity triangles [190–192]. Since in the analysis U is unitary by construction, any given pair of rows or columns can be used to define a triangle in the complex plane. There are a total of six possible triangles corresponding to the unitarity conditions

$$\sum_{i=1,2,3} U_{\alpha i} U_{\beta i}^* = 0 \text{ with } \alpha \neq \beta, \quad \sum_{\alpha=e,\mu,\tau} U_{\alpha i} U_{\alpha j}^* = 0 \text{ with } i \neq j. \quad (14.86)$$

As an illustration we show in Fig. 14.9 the recasting of the allowed regions of the analysis in Ref. [184, 185] in terms of one leptonic unitarity triangle. We show the triangle corresponding to the unitarity conditions on the first and third columns (after the shown rescaling), which is the equivalent to the one usually shown for the quark sector. In this figure, the absence of CP violation would imply a flat triangle, *i.e.*, $\Im(z) = 0$. So the CL at which leptonic CP violation is being observed would be given by the CL at which the region crosses the horizontal axis. Notice however, that this representation is made *under the assumption of a unitary U matrix* and therefore does not provide any test of unitarity in the leptonic sector.

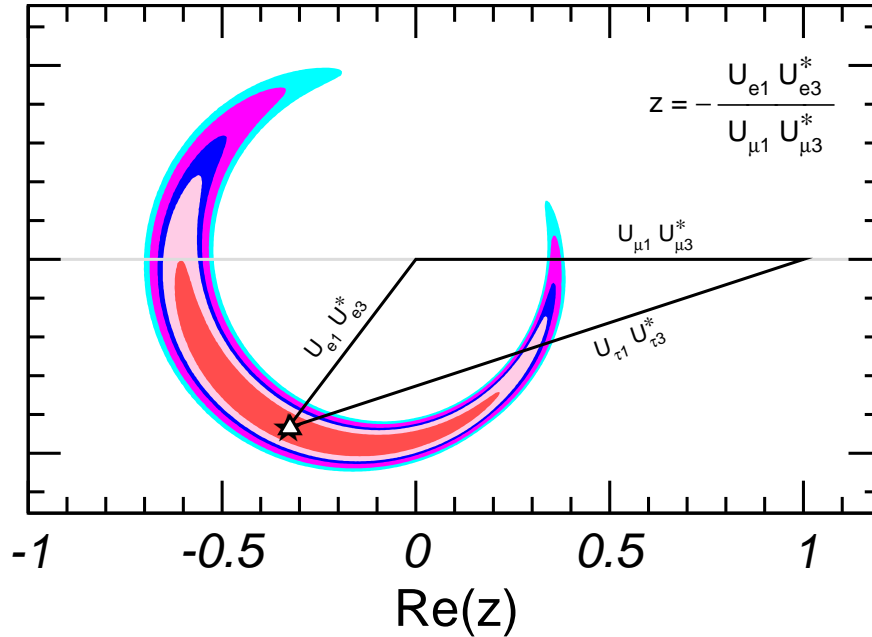


Figure 14.9: Leptonic unitarity triangle for the first and third columns of the mixing matrix. After scaling and rotating the triangle so that two of its vertices always coincide with $(0, 0)$ and $(1, 0)$ the figure shows the 1σ , 90% , 2σ , 99% , 3σ CL (2 dof) allowed regions of the third vertex for the NO from the analysis in Ref. [184, 185].

14.8 Beyond 3ν : Additional Neutrinos at the eV Scale

Besides the huge success of three-flavour oscillations described in Sec.14.7, as mentioned in Secs.14.6.3 and 14.6.4, there are some anomalies which cannot be explained within the 3ν framework and which might point towards the existence of additional neutrino states with masses at the eV scale. In brief:

- the LSND experiment [129] reports evidence for $\bar{\nu}_\mu \rightarrow \bar{\nu}_e$ transitions with $E/L \sim 1 \text{ eV}^2$, where E and L are the neutrino energy and the distance between source and detector, respectively (see *Short Baseline Experiments* subsection of Sec.14.6.3).
- this effect has also been searched for by the MiniBooNE experiment [193], which reports a yet unexplained event excess in the low-energy region of the electron neutrino and antineutrino event spectra. No significant excess is found at higher neutrino energies. Interpreting the data in terms of oscillations, parameter values consistent with the ones from LSND are obtained, but the test is not definitive;
- radioactive source experiments at the Gallium solar neutrino experiments both in SAGE and GALLEX/GNO have obtained an event rate that is somewhat lower than expected. If not due

to uncertainties in the interaction cross-section, this effect can be explained by the hypothesis of ν_e disappearance due to oscillations with $\Delta m^2 \gtrsim 1 \text{ eV}^2$ (“Gallium anomaly”) [194, 195];

- new calculations of the neutrino flux emitted by nuclear reactors [138, 139] predict a neutrino rate that is a few percent higher than observed in short-baseline ($L \lesssim 100 \text{ m}$) reactor experiments⁵. If not due to systematic or theoretical uncertainties, a decrease rate at those distances can be explained by assuming $\bar{\nu}_e$ disappearance due to oscillations with $\Delta m^2 \sim 1 \text{ eV}^2$ (“reactor anomaly”) [198]. This reactor anomaly is under study both by the experimental community – with a set of follow-up measurements performed at SBL both at reactors and accelerators (see the corresponding subsections in Sec.14.6.4 and Sec.14.6.3)–, and by the theory community for improvements of the reactor flux calculations.

As mentioned in Sec.14.1, whatever the extension of the SM we want to consider, it must contain only three light active neutrinos. Therefore if we need more than three light massive neutrinos, we must add sterile neutrinos to the particle content of the model.

The most immediate question as these anomalies were reported was whether they could all be consistently described in combination with the rest of the neutrino data – in particular with the negative results on the disappearance of ν_μ at short distances – if one adds those additional sterile states. Quantitatively one can start by adding a fourth massive neutrino state to the spectrum and perform a global data analysis to answer this question. Although the answer is always the same, the physical reason behind it depends on ordering assumed for the states. In brief, there are six possible four-neutrino schemes that can, in principle, accommodate the results of solar+KamLAND and atmospheric+LBL neutrino experiments as well as the SBL result. They can be divided into two classes: (2+2) and (3+1). In the (3+1) schemes, there is a group of three close-by neutrino masses (as on the 3ν schemes described in the previous section) that is separated from the fourth one by a gap of the order of 1 eV, which is responsible for the SBL oscillations. In (2+2) schemes, there are two pairs of close masses (one pair responsible for solar results and the other for atmospheric [199]) separated by the $\mathcal{O}(\text{eV})$ gap. The main difference between these two classes is the following: if a (2+2)-spectrum is realized in nature, the transition into the sterile neutrino is a solution of either the solar or the atmospheric neutrino problem, or the sterile neutrino takes part in both. Consequently, a (2+2)-spectrum is easier to test because the required mixing of sterile neutrinos in either solar and/or atmospheric oscillations would modify their effective matter potential in the Sun and in the Earth, giving distinctive effects in the solar and/or atmospheric neutrino observables. Those distinctive effects were not observed so oscillations into sterile neutrinos did not describe well either solar or atmospheric data. Consequently, as soon as the early 2000’s 2+2 spectra could be ruled out already beyond 3-4 σ as seen in the left panel in Fig.14.10 taken from Ref. [200].

On the contrary, for a (3+1)-spectrum (and more generally for a $3 + N$ -spectrum with an arbitrary N number of sterile states), the sterile neutrino(s) could be only slightly mixed with the active ones and mainly provide a description of the SBL results. In this case, the oscillation probabilities for experiments working at $E/L \sim 1 \text{ eV}^2$ take a simple form:

$$P_{\alpha\alpha} = 1 - \sin^2 2\theta_{\alpha\alpha} \sin^2 \Delta, \quad P_{\mu e} = \sin^2 2\theta_{\mu e} \sin^2 \Delta, \quad (14.87)$$

where $\Delta \equiv \Delta m_{41}^2 L/4E$ and one can define effective mixing angles

$$\sin^2 2\theta_{\alpha\alpha} \equiv 4|U_{\alpha 4}|^2(1 - |U_{\alpha 4}|^2), \quad \sin^2 2\theta_{\mu e} \equiv 4|U_{\mu 4}|^2|U_{e 4}|^2. \quad (14.88)$$

In here $\alpha = e, \mu$ and $U_{\alpha 4}$ are the elements of the lepton mixing matrix describing the mixing of the 4th neutrino mass state with the electron and muon flavour. In this scenario, there is no sensitivity

⁵However, as discussed in Sec.14.6.4, the reactor antineutrino flux measurement at Daya Bay [196, 197] is consistent with the old flux predictions and the flux measurement results in the previous short-baseline reactor neutrino oscillation experiments.

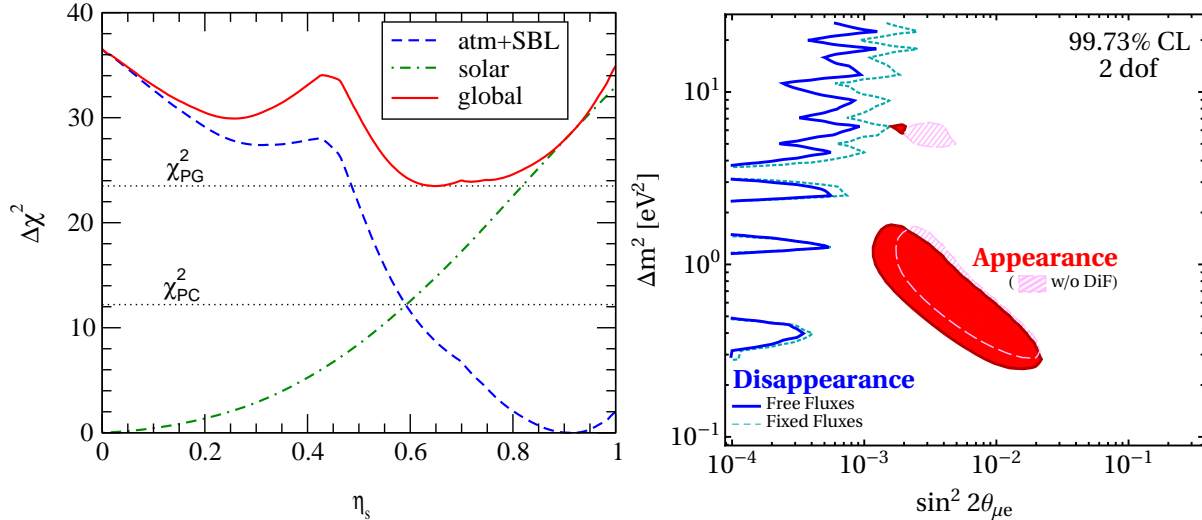


Figure 14.10: *Left:* Status of the 2+2 oscillation scenarios from Ref. [200] ($\eta_S = \sum_i |U_{is}|^2$ where i runs over the two massive states mostly relevant for solar neutrino oscillations). In the figure also shown are the values of χ_{PC}^2 and χ_{PG}^2 relevant for parameter consistency test and parameter goodness of fit, respectively. *Right:* Present status of 3+1 oscillation scenarios from Ref. [201].

to CP violation in the the Δ driven oscillations, so the relations above are valid for both neutrinos and antineutrinos. At linear order in the mixing elements one can derive a relation between the amplitudes of appearance and disappearance probabilities:

$$4 \sin^2 2\theta_{\mu e} \approx \sin^2 2\theta_{ee} \sin^2 2\theta_{\mu\mu}. \quad (14.89)$$

This relation implies a constraint between the possible results in disappearance and appearance experiments. Consequently, it is not trivial to find a consistent description to all the SBL anomalies. Over the years, different groups have performed a variety of such global analyses leading to different quantitative conclusions on the statistical quality of the global fit (see for example [201–206], see also Refs. [207,208] for recent reviews on the subject). Generically, the results of the global analysis show that there is significant tension between groups of different data sets – in particular between appearance and disappearance results – and Eq.(14.89) makes it difficult to obtain a good global fit as illustrated in the right panel in Fig.14.10 taken from Ref. [201] which concluded that 3+1 scenario is excluded at 4.7σ level.

A straightforward question to ask is whether the situation improves if more neutrino states at the eV scale are introduced. The simplest extension is the introduction of 2 states with eV scale mass splittings, ν_4 and ν_5 . The ordering of the states can be such that Δm_{41}^2 and Δm_{51}^2 are both positive (“3+2”), or one of them is negative (“1+3+1”). From the point of view of the description of the data, the most important new qualitative feature is that now, non-zero CP violation at $E/L \sim \text{eV}^2$ is possibly observable [204, 209–211]. This allows some additional freedom in fitting neutrino versus antineutrino data from LSND and MiniBooNE together. However, it still holds that a non-zero $\nu_\mu \rightarrow \nu_e$ appearance at SBL necessarily predicts SBL disappearance for both ν_e and ν_μ . So, generically, the tension between appearance and disappearance results remains, though differences in the methodology of statistical quantification of the degree of agreement/disagreement in these scenarios can lead to different conclusions on whether they can provide a successful description of all the data [201, 207, 208]. Cosmological observations can provide complementary information on

the number of relativistic neutrino states in thermal equilibrium in the early Universe and on the sum of their masses, which sets further constraints on light sterile neutrino scenarios (see Chapter 26 of this *Review*, “Neutrinos in cosmology”).

14.9 Laboratory Probes of ν Mass Scale and its Nature

As described in Secs.14.4 and 14.5, neutrino flavour oscillations in vacuum and flavour transitions in matter only depend on the differences between the neutrino masses-squared, Δm_{ij}^2 , and on the mixing matrix elements, U_{ij} . However, they are insensitive to the absolute mass scale for the neutrinos, m_i . They also give us no information on whether they are Dirac or Majorana particles.

Clearly, the observation of flavour oscillations implies a lower bound on the mass of the heavier neutrino in Δm_{ij}^2 , $|m_i| \geq \sqrt{\Delta m_{ij}^2}$ for $\Delta m_{ij}^2 > 0$. However, there is no upper bound on m_i . In particular, oscillation results allow the neutrino spectrum to be approximately degenerate at a mass scale that is much higher than the $\sqrt{\Delta m_{ij}^2}$ that they determine. Information of the mass scale of the neutrino is provided by other types of experiments. Here we briefly summarize the most sensitive laboratory probes of the neutrino mass scale and on whether they are Dirac or Majorana particles. Cosmological observations provide, albeit indirectly, complementary information on the neutrino mass scale as it is reviewed in Chapter 26 of this *Review*, “Neutrinos in cosmology”.

14.9.1 Constraints from Kinematics of Weak Decays

The only model-independent information on the neutrino masses, rather than mass differences, can be extracted from energy-momentum conservation relation in reactions in which a neutrino or an antineutrino is involved.

Historically these bounds were labeled as limits on the mass of the flavour neutrino states corresponding to the charged flavour involved in the decay. Fermi proposed in 1933 such a kinematic search for the ν_e neutrino mass (which we will label here as $m_{\nu_e}^{\text{eff}}$) in the end part of the beta spectra in ${}^3\text{H}$ beta decay ${}^3\text{H} \rightarrow {}^3\text{He} + e^- + \bar{\nu}_e$.

Because ${}^3\text{H}$ beta decay is a superallowed transition, the nuclear matrix elements are energy independent, so the electron spectrum is determined exclusively by the phase space

$$\frac{dN}{dE} = C p E (Q - T) \sqrt{(Q - T)^2 - (m_{\nu_e}^{\text{eff}})^2} F(E) \equiv R(E) \sqrt{(E_0 - E)^2 - (m_{\nu_e}^{\text{eff}})^2}. \quad (14.90)$$

E_0 is the mass difference between the initial and final nucleus, $E = T + m_e$ is the total electron energy, p its momentum, $Q \equiv E_0 - m_e$ is the maximum kinetic energy of the electron and Final state Coulomb interactions are contained in the Fermi function $F(E)$. $R(E)$ in the second equality contains all the m_{ν} -independent factors.

The Kurie function is defined as $K(T) \equiv \sqrt{\frac{dN}{dE} \frac{1}{pEF(E)}}$. From Eq.(14.90), we see that if $m_{\nu_e}^{\text{eff}}=0$ $K(T)$ would depend linearly on T . A non-vanishing neutrino mass then provokes a distortion from the straight-line T -dependence at the endpoint, So for $m_{\nu_e}^{\text{eff}} = 0$, $T_{\text{max}} = Q$, while for $m_{\nu_e}^{\text{eff}} \neq 0$, $T_{\text{max}} = Q - m_{\nu_e}^{\text{eff}}$. In ${}^3\text{H}$ beta decay $Q = 18.6$ KeV is very small and therefore, this decay is more sensitive to this $m_{\nu_e}^{\text{eff}}$ -induced distortion.

The most recent result on the kinematic search for neutrino mass in tritium decay is from KATRIN [212], an experiment which has found so far no indication of $m_{\nu_e} \neq 0$ and sets an upper limit

$$m_{\nu_e}^{\text{eff}} < 1.1 \text{ eV}, \quad (14.91)$$

at 90% CL improving over the previous bound from the Mainz [213] and Troitsk [214] experiments which constrained $m_{\nu_e}^{\text{eff}} < 2.2$ eV at 95% CL. KATRIN continues running with an estimated sensitivity limit of $m_{\nu_e}^{\text{eff}} \sim 0.2$ eV. Project 8 is exploring a new technique for β -spectrometry based on cyclotron radiation [215].

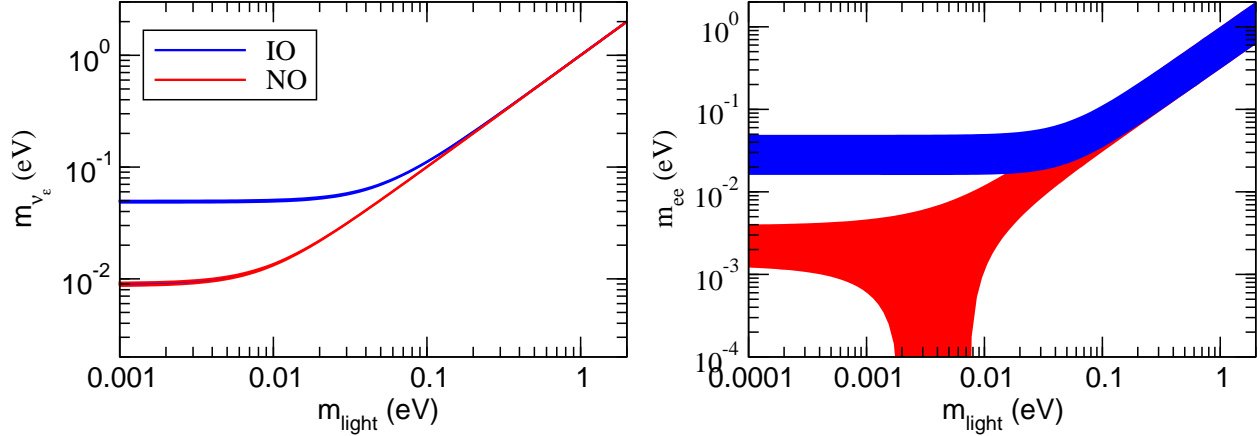


Figure 14.11: Allowed 95% CL ranges (1 dof) for the neutrino mass observable determined in ^3H beta decay (left panel) and in $0\nu\beta\beta$ (right panel) in the framework of 3ν mixing as a function of the lightest neutrino mass. The ranges are obtained by projecting the results of the global analysis of oscillation data (w/o SK-atm) in Ref. [184]. The region for each ordering is defined with respect to its local minimum.

An alternative isotope to Tritium is ^{163}Ho [216] which presents the advantage of a smaller $Q = 2.8$ KeV. It decays via electron capture to ^{163}Dy . Currently, there are three experiments exploring this decay to probe the neutrino mass: ECHo [217], HOLMES [218], and NuMECS [219]. These experiments are complementary to tritium-based searches from a technical point of view. Also, the decay of ^{163}Ho determines the effective electron neutrino mass as opposed to antineutrino in Tritium.

For the other flavours the present limits compiled in the listing section of the PDG read

$$m_{\nu_\mu}^{\text{eff}} < 190 \text{ keV (90\% CL)} \quad \text{from} \quad \pi^- \rightarrow \mu^- + \bar{\nu}_\mu, \quad (14.92)$$

$$m_{\nu_\tau}^{\text{eff}} < 18.2 \text{ MeV (95\% CL)} \quad \text{from} \quad \tau^- \rightarrow n\pi + \nu_\tau. \quad (14.93)$$

In the presence of mixing and for neutrinos with small mass differences, the distortion of the beta spectrum is given by the sum of the individual spectra generated incoherently by each neutrino massive state weighted with the relevant mixing matrix element squared [220]:

$$\frac{dN}{dE} = R(E) \sum_i |U_{ei}|^2 \sqrt{(E_0 - E)^2 - m_i^2} \Theta(E_0 - E - m_i). \quad (14.94)$$

The step function $\Theta(E_0 - E - m_i)$ arises because a neutrino with a given mass m_i can only be produced if the available energy is larger than its mass. Equation (14.94) shows the two main effects of the neutrino masses and mixings on the electron energy spectrum: First, kinks appear at the electron energies $E_e^{(i)} = E \sim E_0 - m_i$ with sizes that are determined by $|U_{ei}|^2$. Second, the endpoint shifts to $E_{\text{ep}} = E_0 - m_0$, where m_0 is the lightest neutrino mass. Corrections are induced once the energy resolution of the experiment is considered. [221, 222]

In the 3ν mixing scenario, the distortion of the spectrum can still be effectively described by a single parameter – which we will still denote as m_{ν_e} – if for all neutrino states $E_0 - E = Q - T \gg m_i$. In this case, one can expand Eq.(14.94) as:

$$\frac{dN}{dE} \simeq R(E) \sum_i |U_{ei}|^2 \sqrt{(E_0 - E)^2 - (m_{\nu_e}^{\text{eff}})^2}, \quad (14.95)$$

with

$$(m_{\nu_e}^{\text{eff}})^2 = \frac{\sum_i m_i^2 |U_{ei}|^2}{\sum_i |U_{ei}|^2} = \sum_i m_i^2 |U_{ei}|^2, \quad (14.96)$$

where unitarity is assumed in the second equality. In this approximation, the distortion of the endpoint of the spectrum is described by a single parameter, and with the present results from KATRIN, it is bounded to be

$$1.1 \text{ eV} \geq m_{\nu_e}^{\text{eff}} = \sqrt{\sum_i m_i^2 |U_{ei}|^2} = \begin{cases} \sqrt{m_0^2 + \Delta m_{21}^2 (1 - c_{13}^2 c_{12}^2) + \Delta m_{32}^2 s_{13}^2} & \text{in NO,} \\ \sqrt{m_0^2 + \Delta m_{21}^2 c_{13}^2 c_{12}^2 - \Delta m_{32}^2 c_{13}^2} & \text{in IO,} \end{cases} \quad (14.97)$$

where $m_0 = m_1$ (m_3) is the lightest neutrino mass in the NO (IO) spectrum. Correspondingly the bounds in Eqs.(14.92) and (14.93) apply to the combinations $\sum_i m_i^2 |U_{\alpha i}|^2$ for $\alpha = \mu$ and τ respectively. So with the values known of the mixing matrix elements, the strongest constraint on the absolute value of the neutrino mass comes from Tritium beta decay.

From Eq.(14.97) we see that, given the present knowledge of the neutrino mass differences and their mixing from oscillation experiments, it is possible to translate the experimental information of m_{ν_e} on a corresponding range for the lightest neutrino mass and that such relation depends on the ordering of the states. We plot in Fig.14.11 the recasting of the allowed regions of the analysis in Ref. [184] in terms of the allowed range m_{ν_e} as a function of $m_{\text{light}} \equiv m_0$. In particular, one finds that the results of oscillation experiments imply a lower bound on $m_{\nu_e} > 0.048$ (0.0085) eV for IO (NO) at 95% CL.

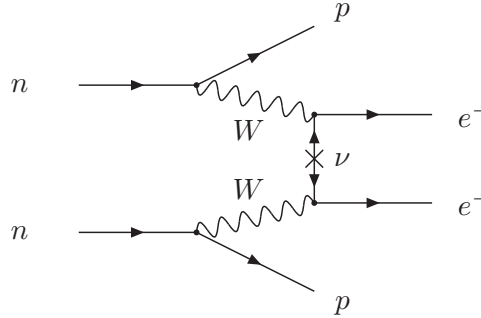


Figure 14.12: Feynman diagram for neutrinoless double-beta decay.

14.9.2 Dirac vs. Majorana: Neutrinoless Double-beta Decay

The most sensitive probe to whether neutrinos are Dirac or Majorana states is the neutrinoless double beta decay ($0\nu\beta\beta$):

$$(A, Z) \rightarrow (A, Z + 2) + e^- + e^-. \quad (14.98)$$

In the presence of neutrino masses and mixing, the process in Eq.(14.98) can be generated at lower order in perturbation theory by the term represented in Fig.14.12. The corresponding amplitude is proportional to the product of the two leptonic currents

$$M_{\alpha\beta} \propto [\bar{e}\gamma_\alpha(1 - \gamma_5)\nu_e] [\bar{e}\gamma_\beta(1 - \gamma_5)\nu_e] \propto \sum_i (U_{ei})^2 [\bar{e}\gamma_\alpha(1 - \gamma_5)\nu_i] [\bar{e}\gamma_\beta(1 - \gamma_5)\nu_i]. \quad (14.99)$$

The neutrino propagator in Fig.14.12 can only arise from the contraction $\langle 0 | \nu_i(x)\nu_i(y)^T | 0 \rangle$. However, if the neutrino is a Dirac particle ν_i field annihilates a neutrino state and creates an antineutrino state, and neutrino and antineutrino states are different, so the contraction $\langle 0 | \nu_i(x)\nu_i(y)^T | 0 \rangle =$

0 and $M_{\alpha\beta} = 0$. On the other hand, if ν_i is a Majorana particle, neutrino and antineutrino are described by the same field and $\langle 0 | \nu_i(x) \nu_i(y)^T | 0 \rangle \neq 0$.

The conclusion is that in order to induce the $0\nu\beta\beta$ decay, neutrinos must be Majorana particles. This is consistent with the fact that the process (14.98) violates the total lepton number by two units. Conversely, if $0\nu\beta\beta$ decay is observed, massive neutrinos cannot be Dirac states [223].

It is important to stress that neutrinoless double-beta decay could be dominantly induced by other new physics effects beyond that of Majorana neutrino masses. Consequently, the connection between the observation or limitation of the neutrinoless double beta decay and the neutrino mass can only be made under some assumption about the source of total lepton number violation in the model.

The observable determined by the experiments is the half-life of the decay. Under the assumption that the Majorana neutrino mass is the only source of lepton number violation at low energies, the decay half-life is given by:

$$(T_{1/2}^{0\nu})^{-1} = G^{0\nu} |M^{0\nu}|^2 \left(\frac{m_{ee}}{m_e}\right)^2, \quad (14.100)$$

where $G^{0\nu}$ is the phase space integral taking into account the final atomic state, $|M^{0\nu}|$ is the nuclear matrix element of the transition, and m_{ee} is the *effective Majorana mass* of ν_e ,

$$m_{ee} = \left| \sum_i m_i U_{ei}^2 \right| = \begin{cases} \left| m_0 c_{12}^2 c_{13}^2 + \sqrt{\Delta m_{21}^2 + m_0^2 s_{12}^2 c_{13}^2} e^{2i(\eta_2 - \eta_1)} + \sqrt{\Delta m_{32}^2 + \Delta m_{21}^2 + m_0^2 s_{13}^2} e^{-2i(\delta_{CP} + \eta_1)} \right| & \text{in NO,} \\ \left| m_0 s_{13}^2 + \sqrt{m_0^2 - \Delta m_{32}^2} s_{12}^2 c_{13}^2 e^{2i(\eta_2 + \delta_{CP})} + \sqrt{m_0^2 - \Delta m_{32}^2 - \Delta m_{21}^2} c_{12}^2 c_{13}^2 e^{2i(\eta_1 + \delta_{CP})} \right| & \text{in IO,} \end{cases}$$

which, in addition to the masses and mixing parameters that affect the tritium beta decay spectrum, also depends on the leptonic CP -violating phases. We plot in Fig.14.11 the recasting of the allowed regions of the analysis in Ref. [184] in terms of the allowed range m_{ee} as a function of $m_{\text{light}} \equiv m_0$ for the two orderings. As a consequence of the dependence on the unknown Majorana phases, the allowed range of m_{ee} for a given value of m_{light} and ordering is substantially broader than that of m_{ν_e} . Nevertheless, the results of oscillation experiments imply a lower bound on the effective Majorana mass for the IO, which at 95%CL reads $m_{ee} > 0.016$ eV.

From Eq.(14.100) we see that nuclear structure details enter relation between the decay rate (or lifetime) and the effective Majorana mass. As a consequence, uncertainties in the nuclear structure calculations result in a spread of m_{ee} values for a given $T_{1/2}^{0\nu}$ by a factor of 2–3 [224].

We present in Sec.14.9.3 a brief description of the experimental searches for neutrinoless double-beta decay. At the time of writing of this review, the strongest bound on $0\nu\beta\beta$ decay lifetimes came for Xenon and Germanium from the KamLAND-Zen [225] and GERDA [226] experiments, respectively. They have set a bound on the corresponding half-lives of $T_{1/2}^{0\nu} > 1.07 \times 10^{26}$ yr, and $T_{1/2}^{0\nu} > 1.8 \times 10^{26}$ yr, at 90% CL. Using a variety of nuclear matrix element calculations, the corresponding upper bounds on the effective Majorana mass are

$$m_{ee} < 61 - 165 \text{ meV} \quad (14.101)$$

$$m_{ee} < 79 - 180 \text{ meV} . \quad (14.102)$$

14.9.3 Experimental Search for Neutrinoless Double-beta Decay

There are 35 candidate nuclei for double-beta decay. Currently, experiments using ^{136}Xe and ^{76}Ge have reported the most sensitive results of $0\nu\beta\beta$ search. Because of the uncertainties related

to the nuclear matrix element, the complementarity of technologies, different backgrounds, and the investigation of the mechanism behind the $0\nu\beta\beta$ in case of a positive signal, it is important to pursue the searches with as many isotopes as possible.

The signature of $0\nu\beta\beta$ is that the sum of the energy of two electrons is equal to the Q -value of the nuclear transition. The energy from electrons is measured with either ionization, scintillation, or through phonons. In some experiments, a combination of two techniques is used to enhance the sensitivity. In the case of background-free measurement, the sensitivity to the half-life is proportional to the product of the detection efficiency of the signal ε , the source mass M , and the measurement time t . If background exists, it is proportional to $\varepsilon\sqrt{\frac{Mt}{b\Delta E}}$, where b is the background rate, and ΔE is the energy resolution.

Among the experiments using ionization detection, ultra-high-purity germanium detector provides the best sensitivity thanks to high energy resolution and low background. GERDA, in its final phase, used a total of 20.0 kg of broad energy germanium (BEGe), 14.6 kg of coaxial detectors, and 9.6 kg of inverted coaxial detectors. A background level of $(5.2_{-1.3}^{+1.6}) \times 10^{-4}$ counts/(keV·kg·year) was achieved [226], which enabled a background-free search. The final result from GERDA for the half-life limit for $0\nu\beta\beta$ decay of ^{76}Ge is $T_{1/2} > 1.8 \times 10^{26}$ years at 90% CL. The Majorana Demonstrator [227] consisted of 44.1 kg of Ge (29.7 kg enriched to 88% in ^{76}Ge) detectors split between two modules. It achieved energy resolution of 2.53 keV FWHM (full width at half maximum) at the Q -value (2.039 MeV). GERDA and Majorana collaborations have united and formed, together with new groups, the LEGEND collaboration. LEGEND has adopted a phased approach toward the deployment of a tonne of enriched Ge detectors [228]. The first phase of LEGEND, based on 200 kg of enriched Ge and using the GERDA infrastructure at LNGS, is expected to start in 2022. The second phase of LEGEND is planned as a one-ton experiment in a new cryostat, reaching a discovery sensitivity of half-life beyond 10^{28} years.

Liquid scintillator detectors have a simple structure and can utilize existing large detectors with low background environments. By adding an inner balloon to contain xenon-loaded liquid scintillator to the KamLAND detector, KamLAND-Zen used 380 kg of xenon with 90.1% enrichment in ^{136}Xe . Reducing the background level by purification of scintillator, KamLAND-Zen reported the half-life limit above 10^{26} years at 90% CL [225]. KamLAND-Zen has been accumulating more data with about 750 kg of enriched xenon. The SNO detector has also been upgraded to be filled with a liquid scintillator in the SNO+ experiment [229]. The SNO+ detector will be loaded with 0.5% natural tellurium, corresponding to approximately 1.3 t of ^{130}Te , to search for $0\nu\beta\beta$.

With a time projection chamber, one can utilize both ionization and scintillation. EXO-200 used a liquid xenon time projection chamber with enrichment to 80.6%, corresponding to 74.7 kg of ^{136}Xe in the fiducial mass [230]. An energy resolution of 1.15% (σ/E) is achieved at the Q -value of ^{136}Xe $0\nu\beta\beta$. Based on the technology validated by EXO-200, nEXO plans to use 5,000 kg of xenon enriched to 90% in ^{136}Xe to achieve beyond 10^{28} year half-life sensitivity [231, 232]. NEXT has been developing a high-pressure xenon gas time projection chamber with electroluminescent amplification and optical readouts. An energy resolution of 1% FWHM at the Q -value of ^{136}Xe $0\nu\beta\beta$ is demonstrated with NEXT-White detector [233]. NEXT proved background suppression by exploiting differences in the spatial ionization patterns of double beta decay and single-electron events [234]. A robust identification of signal is possible by tagging Ba^{2+} ions produced in ^{136}Xe decay. NEXT [235–238] and nEXO [239] have made significant progress in this technology. AXEL develops a cellular readout structure based on electroluminescence for the ^{136}Xe $0\nu\beta\beta$ search using a high-pressure xenon gas time projection chamber [240].

CUORE uses a cryogenic bolometer to measure the energy in a calorimetric way. The detector is located in Gran Sasso and composed of 988 TeO_2 bolometers for a total mass of 742 kg, correspond-

ing to 206 kg of ^{130}Te . An effective energy resolution of (7.0 ± 0.4) keV FWHM is achieved [241]. For further reduction of background towards future search based on the CUORE technology, CUPID proposes to simultaneously measure the calorimetric signal and the scintillation light with a tonne-scale bolometric detector [242]. Using the prototype CUPID-0, the technology is demonstrated, and $0\nu\beta\beta$ is also searched for with ^{82}Se [243] and ^{100}Mo [244].

AMoRE also uses the simultaneous detection of heat and scintillation. Six ^{100}Mo -enriched and ^{48}Ca -depleted CaMoO_4 crystals with a total mass of 1.9 kg (AMoRE-Pilot) are operated in Yangyang underground laboratory located in South Korea, searching for $0\nu\beta\beta$ of ^{100}Mo [245]. Currently, AMoRE-I experiment [246] using 13 enriched CaMoO_4 crystals and 5 enriched Li_2MoO_4 crystals (6 kg total mass) is under operation in Yemilab.

A tracker-calorimeter technique is employed in NEMO. Source isotopes are hosted in thin foils surrounded by a tracking detector, which in turn is surrounded by a calorimeter. Full topological event reconstruction with this configuration enables background rejection and gives additional information after discovery. The NEMO-3 experiment used 7 isotopes, with the largest mass comprised of ^{100}Mo (7 kg) [247]. NEMO-3 also reported the first search for neutrinoless quadrupole- β decay of ^{150}Nd [248].

References

- [1] J. N. Bahcall, *NEUTRINO ASTROPHYSICS* (1989), ISBN 9780521379755.
- [2] R. N. Mohapatra and P. B. Pal, World Sci. Lect. Notes Phys. **60**, 1 (1998), [World Sci. Lect. Notes Phys.72,1(2004)].
- [3] C. W. Kim and A. Pevsner, Contemp. Concepts Phys. **8**, 1 (1993).
- [4] B. Kayser, F. Gibrat-Debu and F. Perrier, World Sci. Lect. Notes Phys. **25**, 1 (1989).
- [5] C. Giunti and C. W. Kim, *Fundamentals of Neutrino Physics and Astrophysics* (2007), ISBN 9780198508717.
- [6] M. C. Gonzalez-Garcia and Y. Nir, *Rev. Mod. Phys.* **75**, 345 (2003), [hep-ph/0202058].
- [7] M. C. Gonzalez-Garcia and M. Maltoni, *Phys. Rept.* **460**, 1 (2008), [arXiv:0704.1800].
- [8] A. Pilaftsis, *Z. Phys.* **C55**, 275 (1992), [hep-ph/9901206].
- [9] P. Minkowski, *Phys. Lett.* **67B**, 421 (1977).
- [10] P. Ramond, in “International Symposium on Fundamentals of Quantum Theory and Quantum Field Theory,” (1979), [hep-ph/9809459].
- [11] M. Gell-Mann, P. Ramond and R. Slansky, Conf. Proc. **C790927**, 315 (1979), [arXiv:1306.4669].
- [12] T. Yanagida, Conf. Proc. C **7902131**, 95 (1979).
- [13] R. N. Mohapatra and G. Senjanovic, *Phys. Rev. Lett.* **44**, 912 (1980).
- [14] J. Schechter and J. W. F. Valle, *Phys. Rev.* **D21**, 309 (1980).
- [15] J. Schechter and J. W. F. Valle, *Phys. Rev.* **D22**, 2227 (1980).
- [16] J. Schechter and J. W. F. Valle, *Phys. Rev.* **D24**, 1883 (1981), [Erratum: Phys. Rev.D25,283(1982)].
- [17] Z. Maki, M. Nakagawa and S. Sakata, *Prog. Theor. Phys.* **28**, 870 (1962).
- [18] Y. Katayama *et al.*, *Prog. Theor. Phys.* **28**, 675 (1962).
- [19] B. Pontecorvo, *Zh. Eksp. Teor. Fiz.* **53**, 1717 (1967).
- [20] N. Cabibbo, *Phys. Rev. Lett.* **10**, 531 (1963).
- [21] M. Kobayashi and T. Maskawa, *Prog. Theor. Phys.* **49**, 652 (1973).

- [22] S. Antusch *et al.*, *JHEP* **10**, 084 (2006), [[hep-ph/0607020](#)].
- [23] S. Antusch and O. Fischer, *JHEP* **10**, 094 (2014), [[arXiv:1407.6607](#)].
- [24] V. N. Gribov and B. Pontecorvo, *Phys. Lett.* **28B**, 493 (1969).
- [25] E. Akhmedov, in “International Conference on History of the Neutrino: 1930-2018 Paris, France, September 5-7, 2018,” (2019), [[arXiv:1901.05232](#)].
- [26] L. Wolfenstein, *Phys. Rev. D* **17**, 2369 (1978).
- [27] A. Halprin, *Phys. Rev.* **D34**, 3462 (1986).
- [28] A. J. Baltz and J. Weneser, *Phys. Rev.* **D37**, 3364 (1988).
- [29] P. D. Mannheim, *Phys. Rev.* **D37**, 1935 (1988).
- [30] L. Landau, *Phys. Z. Sov.* **2**, 46 (1932).
- [31] C. Zener, *Proc. Roy. Soc. Lond.* **A137**, 696 (1932).
- [32] E. Majorana, *Nuovo Cim.* **9**, 43 (1932).
- [33] E. C. G. Stueckelberg, *Helv. Phys. Acta* **5**, 369 (1932).
- [34] T.-K. Kuo and J. T. Pantaleone, *Rev. Mod. Phys.* **61**, 937 (1989).
- [35] S. J. Parke, *Phys. Rev. Lett.* **57**, 1275 (1986).
- [36] W. C. Haxton, *Phys. Rev. Lett.* **57**, 1271 (1986).
- [37] S. T. Petcov, *Phys. Lett. B* **191**, 299 (1987).
- [38] S. P. Mikheyev and A. Y. Smirnov, *Sov. J. Nucl. Phys.* **42**, 913 (1985).
- [39] J. N. Bahcall *et al.*, *Rev. Mod. Phys.* **54**, 767 (1982).
- [40] J. N. Bahcall, A. M. Serenelli and S. Basu, *Astrophys. J.* **621**, L85 (2005), [[arXiv:astro-ph/0412440](#)].
- [41] A. M. Serenelli, W. C. Haxton and C. Pena-Garay, *Astrophys. J.* **743**, 24 (2011), [[arXiv:1104.1639](#)].
- [42] F. L. Villante, *Phys. Lett.* **B742**, 279 (2015), [[arXiv:1410.2796](#)].
- [43] A. Serenelli, *Eur. Phys. J.* **A52**, 4, 78 (2016), [[arXiv:1601.07179](#)].
- [44] R. Davis, Jr., D. S. Harmer and K. C. Hoffman, *Phys. Rev. Lett.* **20**, 1205 (1968).
- [45] B. T. Cleveland *et al.*, *Astrophys. J.* **496**, 505 (1998).
- [46] C. Pena-Garay and A. Serenelli (2008), [[arXiv:0811.2424](#)].
- [47] J. N. Abdurashitov *et al.* (SAGE), *J. Exp. Theor. Phys.* **95**, 181 (2002), [*Zh. Eksp. Teor. Fiz.*122,211(2002)], [[arXiv:astro-ph/0204245](#)].
- [48] W. Hampel *et al.* (GALLEX), *Phys. Lett.* **B447**, 127 (1999).
- [49] M. Altmann *et al.* (GNO), *Phys. Lett.* **B616**, 174 (2005), [[hep-ex/0504037](#)].
- [50] J. N. Abdurashitov *et al.* (SAGE), *Phys. Rev.* **C80**, 015807 (2009), [[arXiv:0901.2200](#)].
- [51] K. S. Hirata *et al.* (Kamiokande-II), *Phys. Rev. Lett.* **63**, 16 (1989).
- [52] K. S. Hirata *et al.* (Kamiokande-II), *Phys. Rev.* **D44**, 2241 (1991), [Erratum: *Phys. Rev.*D45, 2170 (1992)].
- [53] Y. Fukuda *et al.* (Kamiokande), *Phys. Rev. Lett.* **77**, 1683 (1996).
- [54] Y. Fukuda *et al.* (Super-Kamiokande), *Phys. Rev. Lett.* **81**, 1158 (1998), [Erratum: *Phys. Rev. Lett.* 81, 4279 (1998)], [[hep-ex/9805021](#)].
- [55] Y. Fukuda *et al.* (Super-Kamiokande), *Phys. Rev. Lett.* **82**, 2430 (1999), [[hep-ex/9812011](#)].

- [56] K. Abe *et al.* (Super-Kamiokande), *Phys. Rev.* **D94**, 5, 052010 (2016), [arXiv:1606.07538].
- [57] N. Vinyoles *et al.*, *Astrophys. J.* **835**, 2, 202 (2017), [arXiv:1611.09867].
- [58] S. Fukuda *et al.* (Super-Kamiokande), *Phys. Rev. Lett.* **86**, 5651 (2001), [hep-ex/0103032].
- [59] S. Fukuda *et al.* (Super-Kamiokande), *Phys. Rev. Lett.* **86**, 5656 (2001), [hep-ex/0103033].
- [60] B. Aharmim *et al.* (SNO), *Phys. Rev.* **C72**, 055502 (2005), [arXiv:nucl-ex/0502021].
- [61] S. Fukuda *et al.* (Super-Kamiokande), *Phys. Lett.* **B539**, 179 (2002), [hep-ex/0205075].
- [62] Q. R. Ahmad *et al.* (SNO), *Phys. Rev. Lett.* **87**, 071301 (2001), [arXiv:nucl-ex/0106015].
- [63] Q. R. Ahmad *et al.* (SNO), *Phys. Rev. Lett.* **89**, 011301 (2002), [arXiv:nucl-ex/0204008].
- [64] B. Aharmim *et al.* (SNO), *Phys. Rev.* **C88**, 025501 (2013), [arXiv:1109.0763].
- [65] J. Bergstrom *et al.*, *JHEP* **03**, 132 (2016), [arXiv:1601.00972].
- [66] C. Arpesella *et al.* (Borexino), *Phys. Lett. B* **658**, 101 (2008), [arXiv:0708.2251].
- [67] G. Bellini *et al.* (Borexino), *Phys. Rev. Lett.* **108**, 051302 (2012), [arXiv:1110.3230].
- [68] M. Agostini *et al.* (BOREXINO), *Nature* **562**, 7728, 505 (2018).
- [69] M. Agostini *et al.* (BOREXINO), *Nature* **587**, 577 (2020), [arXiv:2006.15115].
- [70] G. Bellini *et al.* (Borexino), *Phys. Rev. D* **82**, 033006 (2010), [arXiv:0808.2868].
- [71] S. Abe *et al.* (KamLAND), *Phys. Rev.* **C84**, 035804 (2011), [arXiv:1106.0861].
- [72] A. Gando *et al.* (KamLAND), *Phys. Rev.* **C92**, 5, 055808 (2015), [arXiv:1405.6190].
- [73] M. Agostini *et al.* (Borexino), *Phys. Rev. D* **100**, 8, 082004 (2019), [arXiv:1707.09279].
- [74] M. Agostini *et al.* (Borexino), *Phys. Rev. D* **101**, 6, 062001 (2020), [arXiv:1709.00756].
- [75] A. Renshaw *et al.* (Super-Kamiokande), *Phys. Rev. Lett.* **112**, 9, 091805 (2014), [arXiv:1312.5176].
- [76] K. Abe *et al.* (Super-Kamiokande), *Phys. Rev. D* **94**, 5, 052010 (2016), [arXiv:1606.07538].
- [77] M. Honda *et al.*, *Phys. Rev.* **D92**, 2, 023004 (2015), [arXiv:1502.03916].
- [78] G. D. Barr *et al.*, *Phys. Rev.* **D74**, 094009 (2006), [arXiv:astro-ph/0611266].
- [79] G. Battistoni *et al.*, *Astropart. Phys.* **19**, 269 (2003), [Erratum: *Astropart. Phys.*19,291(2003)], [hep-ph/0207035].
- [80] J. Evans *et al.*, *Phys. Rev.* **D95**, 2, 023012 (2017), [arXiv:1612.03219].
- [81] C. V. Achar *et al.*, *Phys. Lett.* **18**, 196 (1965).
- [82] F. Reines *et al.*, *Phys. Rev. Lett.* **15**, 429 (1965).
- [83] K. S. Hirata *et al.* (Kamiokande-II), *Phys. Lett. B* **205**, 416 (1988).
- [84] D. Casper *et al.*, *Phys. Rev. Lett.* **66**, 2561 (1991).
- [85] K. Daum *et al.* (Frejus), *Z. Phys.* **C66**, 417 (1995).
- [86] M. Aglietta *et al.* (NUSEX), *Europhys. Lett.* **8**, 611 (1989).
- [87] K. S. Hirata *et al.* (Kamiokande-II), *Phys. Lett.* **B280**, 146 (1992).
- [88] Y. Fukuda *et al.* (Kamiokande), *Phys. Lett.* **B335**, 237 (1994).
- [89] Y. Fukuda *et al.* (Super-Kamiokande), *Phys. Rev. Lett.* **81**, 1562 (1998), [hep-ex/9807003].
- [90] M. Ambrosio *et al.* (MACRO), *Phys. Lett.* **B517**, 59 (2001), [hep-ex/0106049].
- [91] M. C. Sanchez *et al.* (Soudan 2), *Phys. Rev.* **D68**, 113004 (2003), [hep-ex/0307069].
- [92] V. D. Barger *et al.*, *Phys. Rev. Lett.* **82**, 2640 (1999), [arXiv:astro-ph/9810121].
- [93] E. Lisi, A. Marrone and D. Montanino, *Phys. Rev. Lett.* **85**, 1166 (2000), [hep-ph/0002053].

- [94] Y. Ashie *et al.* (Super-Kamiokande), *Phys. Rev. Lett.* **93**, 101801 (2004), [hep-ex/0404034].
- [95] Z. Li *et al.* (Super-Kamiokande), *Phys. Rev.* **D98**, 5, 052006 (2018), [arXiv:1711.09436].
- [96] M. G. Aartsen *et al.* (IceCube), *Phys. Rev.* **D99**, 3, 032007 (2019), [arXiv:1901.05366].
- [97] K. Abe *et al.* (Super-Kamiokande), *Phys. Rev.* **D97**, 7, 072001 (2018), [arXiv:1710.09126].
- [98] A. Albert *et al.* (ANTARES), *JHEP* **06**, 113 (2019), [arXiv:1812.08650].
- [99] M. G. Aartsen *et al.* (IceCube), *Phys. Rev. Lett.* **120**, 7, 071801 (2018), [arXiv:1707.07081].
- [100] S. Adrian-Martinez *et al.* (KM3Net), *J. Phys.* **G43**, 8, 084001 (2016), [arXiv:1601.07459].
- [101] M. G. Aartsen *et al.* (IceCube-Gen2), *J. Phys. G* **48**, 6, 060501 (2021), [arXiv:2008.04323].
- [102] S. Ahmed *et al.* (ICAL), *Pramana* **88**, 5, 79 (2017), [arXiv:1505.07380].
- [103] K. Abe *et al.* (Hyper-Kamiokande) (2018), [arXiv:1805.04163].
- [104] B. Abi *et al.* (DUNE) (2018), [arXiv:1807.10334].
- [105] S. E. Kopp, *Phys. Rept.* **439**, 101 (2007), [arXiv:physics/0609129].
- [106] S. van der Meer (1961), CERN-61-07.
- [107] D. Beavis *et al.* (E899) (1995), BNL-52459.
- [108] M. G. Catanesi *et al.* (HARP), *Nucl. Instrum. Meth.* **A571**, 527 (2007).
- [109] J. M. Paley *et al.* (MIPP), *Phys. Rev.* **D90**, 3, 032001 (2014), [arXiv:1404.5882].
- [110] N. Abgrall *et al.* (NA61), *JINST* **9**, P06005 (2014), [arXiv:1401.4699].
- [111] J. M. Paley *et al.* (MIPP), *Phys. Rev. D* **90**, 3, 032001 (2014), [arXiv:1404.5882].
- [112] N. Abgrall *et al.* (NA61/SHINE), *Phys. Rev. C* **84**, 034604 (2011), [arXiv:1102.0983].
- [113] N. Abgrall *et al.* (NA61/SHINE), *Eur. Phys. J. C* **76**, 11, 617 (2016), [arXiv:1603.06774].
- [114] M. H. Ahn *et al.* (K2K), *Phys. Rev.* **D74**, 072003 (2006), [hep-ex/0606032].
- [115] P. Adamson *et al.* (MINOS), *Phys. Rev. Lett.* **110**, 25, 251801 (2013), [arXiv:1304.6335].
- [116] P. Adamson *et al.* (MINOS), *Phys. Rev. Lett.* **112**, 191801 (2014), [arXiv:1403.0867].
- [117] P. Adamson *et al.* (MINOS+), *Phys. Rev. Lett.* **125**, 13, 131802 (2020), [arXiv:2006.15208].
- [118] N. Agafonova *et al.* (OPERA), *Phys. Rev. Lett.* **120**, 21, 211801 (2018), [Erratum: *Phys. Rev. Lett.* 121, no.13, 139901 (2018)], [arXiv:1804.04912].
- [119] C. Rubbia *et al.*, *JINST* **6**, P07011 (2011), [arXiv:1106.0975].
- [120] K. Abe *et al.* (T2K), *Phys. Rev. Lett.* **107**, 041801 (2011), [arXiv:1106.2822].
- [121] K. Abe *et al.* (T2K), *Phys. Rev. Lett.* **112**, 061802 (2014), [arXiv:1311.4750].
- [122] K. Abe *et al.* (T2K), *Nature* **580**, 7803, 339 (2020), [Erratum: *Nature* 583, E16 (2020)], [arXiv:1910.03887].
- [123] K. Abe *et al.* (T2K), *Phys. Rev. D* **103**, 11, 112008 (2021), [arXiv:2101.03779].
- [124] P. Adamson *et al.* (NOvA), *Phys. Rev. Lett.* **116**, 15, 151806 (2016), [arXiv:1601.05022].
- [125] P. Adamson *et al.* (NOvA), *Phys. Rev. Lett.* **118**, 23, 231801 (2017), [arXiv:1703.03328].
- [126] M. A. Acero *et al.* (NOvA), *Phys. Rev. Lett.* **123**, 15, 151803 (2019), [arXiv:1906.04907].
- [127] B. Abi *et al.* (DUNE), *JINST* **15**, 08, T08008 (2020), [arXiv:2002.02967].
- [128] K. Abe *et al.* (Hyper-Kamiokande) (2018), [arXiv:1805.04163].
- [129] A. Aguilar-Arevalo *et al.* (LSND), *Phys. Rev.* **D64**, 112007 (2001), [hep-ex/0104049].
- [130] B. Armbruster *et al.* (KARMEN), *Phys. Rev.* **D65**, 112001 (2002), [hep-ex/0203021].

- [131] A. A. Aguilar-Arevalo *et al.* (MiniBooNE), *Phys. Rev. D* **103**, 5, 052002 (2021), [[arXiv:2006.16883](#)].
- [132] M. Antonello *et al.* (MicroBooNE, LAr1-ND, ICARUS-WA104) (2015), [[arXiv:1503.01520](#)].
- [133] S. Ajimura *et al.* (JSNS2), *Nucl. Instrum. Meth. A* **1014**, 165742 (2021), [[arXiv:2104.13169](#)].
- [134] F. Von Feilitzsch, A. A. Hahn and K. Schreckenbach, *Phys. Lett.* **118B**, 162 (1982).
- [135] K. Schreckenbach *et al.*, *Phys. Lett.* **160B**, 325 (1985).
- [136] A. A. Hahn *et al.*, *Phys. Lett.* **B218**, 365 (1989).
- [137] P. Vogel *et al.*, *Phys. Rev.* **C24**, 1543 (1981).
- [138] T. A. Mueller *et al.*, *Phys. Rev.* **C83**, 054615 (2011), [[arXiv:1101.2663](#)].
- [139] P. Huber, *Phys. Rev.* **C84**, 024617 (2011), [Erratum: *Phys. Rev.*C85,029901(2012)], [[arXiv:1106.0687](#)].
- [140] D. Adey *et al.* (Daya Bay), *Phys. Rev.* **D100**, 5, 052004 (2019), [[arXiv:1808.10836](#)].
- [141] D. Adey *et al.* (Daya Bay), *Phys. Rev. Lett.* **121**, 24, 241805 (2018), [[arXiv:1809.02261](#)].
- [142] G. Bak *et al.* (RENO), *Phys. Rev. Lett.* **121**, 20, 201801 (2018), [[arXiv:1806.00248](#)].
- [143] H. de Kerret *et al.* (Double Chooz), *Nature Phys.* **16**, 5, 558 (2020), [[arXiv:1901.09445](#)].
- [144] Y. J. Ko *et al.* (NEOS), *Phys. Rev. Lett.* **118**, 12, 121802 (2017), [[arXiv:1610.05134](#)].
- [145] M. Apollonio *et al.* (CHOOZ), *Eur.Phys.J.* **C27**, 331 (2003), [[hep-ex/0301017](#)].
- [146] F. Boehm *et al.*, *Phys. Rev.* **D64**, 112001 (2001), [[hep-ex/0107009](#)].
- [147] K. Eguchi *et al.* (KamLAND), *Phys. Rev. Lett.* **90**, 021802 (2003), [[hep-ex/0212021](#)].
- [148] T. Araki *et al.* (KamLAND), *Phys. Rev. Lett.* **94**, 081801 (2005), [[hep-ex/0406035](#)].
- [149] A. Gando *et al.* (KamLAND), *Phys. Rev.* **D88**, 3, 033001 (2013), [[arXiv:1303.4667](#)].
- [150] Y. Abe *et al.* (Double Chooz), *Phys. Rev. Lett.* **108**, 131801 (2012), [[arXiv:1112.6353](#)].
- [151] F. P. An *et al.* (Daya Bay), *Phys. Rev. Lett.* **108**, 171803 (2012), [[arXiv:1203.1669](#)].
- [152] J. K. Ahn *et al.* (RENO), *Phys. Rev. Lett.* **108**, 191802 (2012), [[arXiv:1204.0626](#)].
- [153] F. An *et al.* (JUNO), *J. Phys.* **G43**, 3, 030401 (2016), [[arXiv:1507.05613](#)].
- [154] I. Alekseev *et al.* (DANSS), *Phys. Lett.* **B787**, 56 (2018), [[arXiv:1804.04046](#)].
- [155] H. Almazán *et al.* (STEREO), *Phys. Rev. D* **102**, 5, 052002 (2020), [[arXiv:1912.06582](#)].
- [156] M. Andriamirado *et al.* (PROSPECT), *Phys. Rev. D* **103**, 3, 032001 (2021), [[arXiv:2006.11210](#)].
- [157] A. P. Serebrov *et al.* (NEUTRINO-4), *Pisma Zh. Eksp. Teor. Fiz.* **109**, 4, 209 (2019), [*JETP Lett.*109,no.4,213(2019)], [[arXiv:1809.10561](#)].
- [158] A. P. Serebrov *et al.*, *Phys. Rev. D* **104**, 3, 032003 (2021), [[arXiv:2005.05301](#)].
- [159] Y. Abreu *et al.* (SoLid), *JINST* **16**, 02, P02025 (2021), [[arXiv:2002.05914](#)].
- [160] N. Cabibbo, *Phys. Lett.* **72B**, 333 (1978).
- [161] S. M. Bilenky, J. Hosek and S. T. Petcov, *Phys. Lett.* **94B**, 495 (1980).
- [162] V. D. Barger, K. Whisnant and R. J. N. Phillips, *Phys. Rev. Lett.* **45**, 2084 (1980).
- [163] P. Langacker *et al.*, *Nucl. Phys.* **B282**, 589 (1987).
- [164] S. Goswami and A. Yu. Smirnov, *Phys. Rev.* **D72**, 053011 (2005), [[hep-ph/0411359](#)].
- [165] N. Okamura, *Prog. Theor. Phys.* **114**, 1045 (2006), [[hep-ph/0411388](#)].

- [166] H. Nunokawa, S. J. Parke and R. Zukanovich Funchal, *Phys. Rev.* **D72**, 013009 (2005), [[hep-ph/0503283](#)].
- [167] A. Cervera *et al.*, *Nucl. Phys.* **B579**, 17 (2000), [Erratum: *Nucl. Phys.*B593,731(2001)], [[hep-ph/0002108](#)].
- [168] M. Freund, *Phys. Rev.* **D64**, 053003 (2001), [[hep-ph/0103300](#)].
- [169] E. K. Akhmedov *et al.*, *JHEP* **04**, 078 (2004), [[hep-ph/0402175](#)].
- [170] H. Minakata *et al.*, *Phys. Rev.* **D74**, 053008 (2006), [[hep-ph/0607284](#)].
- [171] O. L. G. Peres and A. Yu. Smirnov, *Nucl. Phys.* **B680**, 479 (2004), [[hep-ph/0309312](#)].
- [172] S. Petcov, *Phys.Lett.* **B434**, 321 (1998), [[hep-ph/9805262](#)].
- [173] E. K. Akhmedov *et al.*, *Nucl.Phys.* **B542**, 3 (1999), [[hep-ph/9808270](#)].
- [174] E. K. Akhmedov, *Nucl.Phys.* **B538**, 25 (1999), [[hep-ph/9805272](#)].
- [175] M. Chizhov, M. Maris and S. Petcov (1998), SISSA-53-98-EP, [[hep-ph/9810501](#)].
- [176] M. Chizhov and S. Petcov, *Phys.Rev.Lett.* **83**, 1096 (1999), [[hep-ph/9903399](#)].
- [177] E. K. Akhmedov, M. Maltoni and A. Y. Smirnov, *JHEP* **0705**, 077 (2007), [[hep-ph/0612285](#)].
- [178] C. Kim and U. Lee, *Phys.Lett.* **B444**, 204 (1998), [[hep-ph/9809491](#)].
- [179] O. Peres and A. Y. Smirnov, *Phys.Lett.* **B456**, 204 (1999), [[hep-ph/9902312](#)].
- [180] M. Gonzalez-Garcia, M. Maltoni and A. Y. Smirnov, *Phys.Rev.* **D70**, 093005 (2004), [[hep-ph/0408170](#)].
- [181] E. K. Akhmedov, M. Maltoni and A. Y. Smirnov, *JHEP* **0806**, 072 (2008), [[arXiv:0804.1466](#)].
- [182] J. Bernabeu, S. Palomares Ruiz and S. Petcov, *Nucl.Phys.* **B669**, 255 (2003), [[hep-ph/0305152](#)].
- [183] S. Petcov and T. Schwetz, *Nucl.Phys.* **B740**, 1 (2006), [[hep-ph/0511277](#)].
- [184] I. Esteban *et al.*, *JHEP* **01**, 106 (2019), [[arXiv:1811.05487](#)].
- [185] I. Esteban *et al.*, “Nufit4.1 at nufit webpage,” <http://www.nu-fit.org>.
- [186] F. Capozzi *et al.*, *Prog. Part. Nucl. Phys.* **102**, 48 (2018), [[arXiv:1804.09678](#)].
- [187] P. F. de Salas *et al.*, *Phys. Lett.* **B782**, 633 (2018), [[arXiv:1708.01186](#)].
- [188] M. Friend, “Updated Results from the T2K Experiment with 3.13×10^{21} Protons on Target,” (2019), KEK/J-PARC Physics seminar, January 10, 2019, URL <https://t2k.org/docs/talk/335/2019kekseminar>.
- [189] C. Jarlskog, *Phys. Rev. Lett.* **55**, 1039 (1985).
- [190] M. C. Gonzalez-Garcia, M. Maltoni and T. Schwetz, *JHEP* **11**, 052 (2014), [[arXiv:1409.5439](#)].
- [191] Y. Farzan and A. Yu. Smirnov, *Phys. Rev.* **D65**, 113001 (2002), [[hep-ph/0201105](#)].
- [192] A. Dueck, S. Petcov and W. Rodejohann, *Phys. Rev.* **D82**, 013005 (2010), [[arXiv:1006.0227](#)].
- [193] A. Aguilar-Arevalo *et al.* (MiniBooNE) (2012), [[arXiv:1207.4809](#)].
- [194] M. A. Acero, C. Giunti and M. Laveder, *Phys. Rev.* **D78**, 073009 (2008), [[arXiv:0711.4222](#)].
- [195] C. Giunti and M. Laveder, *Phys. Rev.* **C83**, 065504 (2011), [[arXiv:1006.3244](#)].
- [196] F. P. An *et al.* (Daya Bay), *Phys. Rev. Lett.* **116**, 6, 061801 (2016), [Erratum: *Phys. Rev. Lett.*118,no.9,099902(2017)], [[arXiv:1508.04233](#)].
- [197] F. P. An *et al.* (Daya Bay), *Phys. Rev. Lett.* **118**, 25, 251801 (2017), [[arXiv:1704.01082](#)].
- [198] G. Mention *et al.*, *Phys. Rev.* **D83**, 073006 (2011), [[arXiv:1101.2755](#)].

- [199] J. J. Gomez-Cadenas and M. C. Gonzalez-Garcia, *Z. Phys.* **C71**, 443 (1996), [[hep-ph/9504246](#)].
- [200] M. Maltoni *et al.*, *Nucl. Phys.* **B643**, 321 (2002), [[hep-ph/0207157](#)].
- [201] M. Dentler *et al.*, *JHEP* **08**, 010 (2018), [[arXiv:1803.10661](#)].
- [202] C. Giunti and M. Laveder, *Phys. Rev.* **D84**, 093006 (2011), [[arXiv:1109.4033](#)].
- [203] J. M. Conrad *et al.*, *Adv. High Energy Phys.* **2013**, 163897 (2013), [[arXiv:1207.4765](#)].
- [204] J. Kopp *et al.*, *JHEP* **05**, 050 (2013), [[arXiv:1303.3011](#)].
- [205] G. H. Collin *et al.*, *Phys. Rev. Lett.* **117**, 22, 221801 (2016), [[arXiv:1607.00011](#)].
- [206] S. Gariazzo *et al.*, *JHEP* **06**, 135 (2017), [[arXiv:1703.00860](#)].
- [207] A. Diaz *et al.*, *Phys. Rept.* **884**, 1 (2020), [[arXiv:1906.00045](#)].
- [208] S. Böser *et al.*, *Prog. Part. Nucl. Phys.* **111**, 103736 (2020), [[arXiv:1906.01739](#)].
- [209] G. Karagiorgi *et al.*, *Phys. Rev.* **D75**, 013011 (2007), [Erratum: *Phys. Rev.D*80,099902(2009)], [[hep-ph/0609177](#)].
- [210] M. Maltoni and T. Schwetz, *Phys. Rev.* **D76**, 093005 (2007), [[arXiv:0705.0107](#)].
- [211] C. Giunti and M. Laveder, *Phys. Rev.* **D84**, 073008 (2011), [[arXiv:1107.1452](#)].
- [212] M. Aker *et al.* (KATRIN) (2019), [[arXiv:1909.06048](#)].
- [213] J. Bonn *et al.*, *Nucl. Phys. B Proc. Suppl.* **91**, 273 (2001).
- [214] V. M. Lobashev *et al.*, *Nucl. Phys. B Proc. Suppl.* **91**, 280 (2001).
- [215] B. Monreal and J. A. Formaggio, *Phys. Rev.* **D80**, 051301 (2009), [[arXiv:0904.2860](#)].
- [216] A. De Rujula and M. Lusignoli, *Phys. Lett.* **118B**, 429 (1982).
- [217] L. Gastaldo *et al.*, *J. Low Temp. Phys.* **176**, 5-6, 876 (2014), [[arXiv:1309.5214](#)].
- [218] B. Alpert *et al.*, *Eur. Phys. J.* **C75**, 3, 112 (2015), [[arXiv:1412.5060](#)].
- [219] M. P. Croce *et al.*, *J. Low. Temp. Phys.* **184**, 3-4, 958 (2016), [[arXiv:1510.03874](#)].
- [220] R. E. Shrock, *Phys. Lett.* **96B**, 159 (1980).
- [221] F. Vissani, *Nucl. Phys. B Proc. Suppl.* **100**, 273 (2001), [[hep-ph/0012018](#)].
- [222] Y. Farzan, O. L. G. Peres and A. Yu. Smirnov, *Nucl. Phys.* **B612**, 59 (2001), [[hep-ph/0105105](#)].
- [223] J. Schechter and J. W. F. Valle, *Phys. Rev. D* **25**, 2951 (1982).
- [224] J. Engel and J. Menendez, *Rept. Prog. Phys.* **80**, 4, 046301 (2017), [[arXiv:1610.06548](#)].
- [225] A. Gando *et al.* (KamLAND-Zen), *Phys. Rev. Lett.* **117**, 8, 082503 (2016), [Addendum: *Phys.Rev.Lett.* 117, 109903 (2016)], [[arXiv:1605.02889](#)].
- [226] M. Agostini *et al.* (GERDA), *Phys. Rev. Lett.* **125**, 25, 252502 (2020), [[arXiv:2009.06079](#)].
- [227] S. I. Alvis *et al.* (Majorana), *Phys. Rev. C* **100**, 2, 025501 (2019), [[arXiv:1902.02299](#)].
- [228] N. Abgrall *et al.* (LEGEND) (2021), [[arXiv:2107.11462](#)].
- [229] V. Albanese *et al.* (SNO+), *JINST* **16**, 08, P08059 (2021), [[arXiv:2104.11687](#)].
- [230] G. Anton *et al.* (EXO-200), *Phys. Rev. Lett.* **123**, 16, 161802 (2019), [[arXiv:1906.02723](#)].
- [231] S. A. Kharusi *et al.* (nEXO) (2018), [[arXiv:1805.11142](#)].
- [232] G. Adhikari *et al.* (nEXO) (2021), [[arXiv:2106.16243](#)].
- [233] J. Renner *et al.* (NEXT), *JINST* **13**, 10, P10020 (2018), [[arXiv:1808.01804](#)].
- [234] A. Simón *et al.* (NEXT), *JHEP* **21**, 146 (2020), [[arXiv:2102.11931](#)].

- [235] D. R. Nygren, *J. Phys. Conf. Ser.* **650**, 1, 012002 (2015).
- [236] B. J. P. Jones, A. D. McDonald and D. R. Nygren, *JINST* **11**, 12, P12011 (2016), [[arXiv:1609.04019](#)].
- [237] A. D. McDonald *et al.*, *Phys. Rev. Lett.* **120**, 13, 132504 (2018), [[arXiv:1711.04782](#)].
- [238] I. Rivilla *et al.*, *Nature* **583**, 7814, 48 (2020).
- [239] C. Chambers *et al.* (nEXO), *Nature* **569**, 7755, 203 (2019), [[arXiv:1806.10694](#)].
- [240] S. Ban *et al.*, *PTEP* **2020**, 3, 033H01 (2020), [[arXiv:2001.03281](#)].
- [241] D. Q. Adams *et al.* (CUORE), *Phys. Rev. Lett.* **124**, 12, 122501 (2020), [[arXiv:1912.10966](#)].
- [242] W. R. Armstrong *et al.* (CUPID) (2019), [[arXiv:1907.09376](#)].
- [243] O. Azzolini *et al.* (CUPID), *Phys. Rev. Lett.* **123**, 3, 032501 (2019), [[arXiv:1906.05001](#)].
- [244] E. Armengaud *et al.* (CUPID), *Phys. Rev. Lett.* **126**, 18, 181802 (2021), [[arXiv:2011.13243](#)].
- [245] V. Alenkov *et al.* (AMoRE), *Eur. Phys. J.* **C79**, 9, 791 (2019), [[arXiv:1903.09483](#)].
- [246] M. H. Lee (AMoRE), *JINST* **15**, 08, C08010 (2020), [[arXiv:2005.05567](#)].
- [247] R. Arnold *et al.* (NEMO-3), *Phys. Rev.* **D92**, 7, 072011 (2015), [[arXiv:1506.05825](#)].
- [248] R. Arnold *et al.* (NEMO-3), *Phys. Rev. Lett.* **119**, 4, 041801 (2017), [[arXiv:1705.08847](#)].